CHAPTER ONE

1.0   INTRODUCTION

1.1 Background to the Study

With the energy demand rising and production from mature fields on the decline, oil and gas companies are expanding activities into increasing challenging areas. Exploring for oil and gas is a risky and expensive business. It takes about 5.5 to 9.5 million dollars to drill and complete oil well (Phillip, 2008). The drilling success rate is still low. For instance, in 2006, out of 119 Gulf of Mexico exploration wells drilled in deep water (300 m below) only 11 wells hit the pay due to murky seismic images. Therefore, there is need to improve on exploration and production technology so as to provide high quality results to reduce risk and frequency of dry wells (Alfaro *et al*., 2007 and Suslick *et al*., 2009). Seismic inversion is a sophisticated tool used by the oil and gas companies to integrate 3D seismic data with petrophysical measurements from wells to improve spatial resolution, reduce risk in exploration and enhance development and production operations. This technique combines well logs that measure many reservoir properties at high vertical resolution with sparse sampling laterally, with seismic data that provides nearly continuous lateral sampling at relatively low cost though with much less vertical resolution (Neves *et al*., 2004 and Avseth *et al.*, 2005).

Seismic data these days include not only full stack data but also data stacked at various offset and angle of incidence ranges to exploit AVO (amplitude variation with offset) /AVA (amplitude variation with angle) information in the data. Seismic amplitude interpretation ensures accurate estimation of elastic properties in target reservoir intervals (Chopra and Kuhn, 2001 and Singh *et al*., 2014). 2D seismic data has been helpful in building structural frame work of the subsurface

with certain degree of reliability to reveal prospects but has proven to be insufficient in complex structural settings while the introduction of 3D seismic data technology led to the adoption of seismic attribute analysis (Filippova *et al.*, 2011).

AVA seismic attributes are quantities extracted from the seismic volumes in order to enhance information that are subtle in a traditional seismic image, leading to a better geological and geophysical interpretation of data (Chopra and Marfurt, 2005; Sheriff, 1992). The usefulness of AVA seismic attributes increased dramatically when elastic inversion of partial stacks was introduced. This enabled some elastic parameters such as V_S/V_P ratio, Poisson's ratio, and λ/μ to be estimated that can be used to identify prospect zones and unravel ambiguity associated with complex areas (Rasmussen, 2004; Shaoming and George, 2004). There are several techniques for inverting seismic data for qualitative estimates of reservoir properties but all require some prior information to constrain the inversion depending on the type of inversion. The prior information may include a rock physics model and rock property trends to relate reservoir properties as demonstrated by Connolly and Hughes (2014). Using a broad-band seismic data with greater frequency content will significantly reduce the bias of a prior data input (Backus, 1987; Lortzer and Berkhout, 1992; Goodway *et al*., 1997 and Michel, 2010). Omudu *et al*. (2007) used cross-plots technique to discriminate fluids in reservoirs in the Niger Delta while Adekanle and Enikanselu (2013) used simultaneous inversion technique to predict porosity of a field in Niger Delta, southern part of Nigeria.

During the last decades, several techniques for estimating rock properties from seismic data were developed and tested to provide additional information for detailed reservoir modeling. The first deterministic inversion methods for acoustic impedance were developed in the late 1970s and became

to be known generally as recursive inversion (Lavergne and Willm, 1977; Lindseth, 1979). Nowadays, most of the research efforts in this field are focused in the inversion and interpretation of variations of seismic reflection amplitude with change in angle of incidence of prestack data. However, post stack data obtained from recorded P-waves are still widely used because of their ready availability and low time consuming processing. Most wells in a reservoir field are often spaced at hundreds to thousands of meters apart. The ultimate goal of seismic inversion is to provide models not only of acoustic impedance but also of other relevant seismic attributes for the inter well regions (Rijks and Jauffred, 1991; Lefeuvre *et al.,* 1995; Sancevero *et al*., 2005). Simultaneous and elastic impedance inversion techniques have demonstrated some advantages over some recently used methods. The integration of the two techniques with high quality datasets can provide vastly improved elastic volumes at much lower computational cost (Dolberg *et al.,* 2000; Dufour *et al*., 2002; Adekanle and Enikanselu, 2013; Kong *et al*., 2013). The Lame's parameters (λ, μ and ρ) that are of interest in this study are considered to be fundamental elastic constants that are applicable for exploration and development of reservoirs in various geological settings throughout the world (Goodway *et al*., 1997: Chen *et al*., 1998; Gray and Anderson 2000).

 In this study, Simultaneous and Elastic impedance inversion techniques were adopted to properly discriminate the lithology and fluid types of subtle features in 'Sandfish' Field, offshore Niger Delta. This will enhance hydrocarbon discovery and optimize development plans in 'Sandfish' Field.

1.2 Statement of the Problem

Mis-interpretation of seismic data which could be due to subtle features of complex reservoirs has resulted into bypass of hydrocarbon zones and drilling of many dry holes (Sheriff 1992; Allen and Peddy, 1993; Filippova *et al.*, 2011). Complex reservoirs are characterized by small acoustic contrast and fault shadow. This makes their identification through independent methodologies such as Multi-dimensional attribute analysis, Neural networks, AVO analysis, Inversion etc. difficult (Avseth *et al.*, 2005; Young *et al*., 2007; Omar *et al*., 2006; Adekanle and Enikanselu, 2013). However, seismic inversion has the capacity to properly discriminate lithology and fluid types of subtle features even beyond the drilled region. This has informed the integration of simultaneous and elastic impedance inversion techniques to improve the vertical and lateral variation of seismic and well data for better characterization of the lithology and fluid types identified in 'Sandfish' Field.

1.3 Aim and Objectives

The aim of this study is to use quantitative AVA attributes analysis involving Simultaneous and Elastic impedance inversion techniques to enhance hydrocarbon discovery and optimize development plans in 'Sandfish' Field, offshore, Niger Delta.

The objectives of the study are to;

i. carry out AVA sensitivity analysis on interval of interest in 'Sandfish' Field;

ii. generate elastic volumes from Simultaneous and Elastic impedance inversions;

iii. establish relationships between inverted volumes and petrophysical logs;

iv. carry out blind well test to validate inversion products away from well control;

v. compare inverted volumes from Simultaneous and Elastic impedance inversion techniques using cross plot and regression equation;

vi. generate fluid probability and lithology maps along horizon of interest.

1.4 Significance of the Study

The integration of seismic and well data involving simultaneous and elastic impedance inversion techniques will provide detailed subsurface information on the study area. The elastic volumes that would be generated will assist in estimating other reservoir properties which will enhance hydrocarbon discovery in 'Sandfish' Field. The knowledge of the lithology and fluid types will reduce the degree of uncertainty which in turn will optimize development plans in 'Sandfish' Field.

1.5 Definitions of Terms

ASCII: Generic Text file format used to import well data.

AVA Attributes: These are quantities extracted from the seismic volume in order to enhance information that are subtle in a traditional seismic image for better geological and geophysical interpretation.

Band-limited Volume: Seismic data is band-limited with inconsistent low frequency content.

Calibrated Volume: The inverted volume that will match both seismic and well data.

Constraints: These are conditions or factors used as guide for optimal inversion results that will match both seismic and well data.

Elastic Impedance Inversion: This is an approximation of acoustic impedance for variable incidence angle.

Full-bandwidth Volume: This is obtained when low frequency component from a different source e.g. well data is introduced into the seismic data to broaden the frequency spectrum.

Hydrocarbon Reservoirs: These are porous or fractured rock formations that contain oil or natural gas trapped by overlying rock formation with lower permeability.

SEG-Y: File format for storing geophysical data controlled by Society of Exploration Geophysicist (SEG).

Simultaneous Inversion: This is a technique that quantitatively integrates well data and AVA seismic data to produce calibrated 3D volume of rock properties.

1.6 List of Abbreviations

2D: Two Dimensions

3D: Three Dimensions

AVA: Amplitude Variation with Angle of Incidence

AVO: Amplitude Variation with Offset

DPR: Department of Petroleum Resources

DTC: Compressional Sonic log

DTS: Shear Sonic log

EI: Elastic Impedance

Frmg: Fluid replacement model for gas

Frmo: Fluid replacement model for oil

Frmw: Fluid replacement model for water

GR: Gamma ray log

HRS: Hampson Russell Software

PHIT: Total Porosity log

QC: Quality Control

RHOB: Density log

Sfn: Sandfish

Sw: Water Saturation

SWT: In-situ Water Saturation

TVD: True Vertical Depth

TVDSS: True Vertical Depth Sub-sea

Vp: Compressional Wave Velocity

Vs: Shear Wave Velocity

Vsand: Volume of Sand

Vshale: Volume of Shale

1.7 List of Symbols

%: Percentage

σ: Poisson's Ratio

(°): Degree

μρ: Mu-rho

ρ: Density

ϕ: Porosity

λρ: Lambda-rho

K: Bulk modulus

Vsh: Volume of shale

Z$_P$: P-impedance

Z$_S$: S-impedance

CHAPTER TWO

2.0 LITERATURE REVIEW

It is easier to understand the connection between reservoir properties and fundamental rock properties such as compressibility and rigidity than with traditional seismic attributes like amplitude and velocity. The application of extracted rock properties such as Z_P, Z_S and ρ has been helpful in exploration and reservoir development (Chen *et al.,* 1998 and Gray and Andersen, 2000). The estimation of spatial distributions of these elastic parameters (Z_P, Z_S and ρ) from pre-stack seismic amplitude data is of interest to both exploration and reservoir geophysicists. That is why most oil and gas industries adopt seismic inversion since it is one of the techniques that transforms seismic reflection data into quantitative rock property, descriptive of the reservoir (Pendrel *et al.,* 2000 and Contreras *et al.*, 2006).

2.1 Seismic Inversion

Berge *et al.* (2002) used seismic inversion to predict porosity and reservoir properties prior to a field development. Likewise, Young *et al.* (2007) demonstrated the inversion of a single seismic data set with the deterministic post partial and pre-stack seismic inversion algorithm in order to transform the estimated elastic parameters to porosity through well-calibrated transformations. This was used to characterize Miocene reservoirs in Anadarko's deep water Marco field. The model accurately revealed the major stratigraphic and structural features in the Marco Polo Field. The hydrocarbon saturated M-series reservoirs were characterized by anomalous low P-impedance. The pre-stack inverted volumes provided a better P-impedance estimate than the post partial stacks because the former fits more data. However, in the Marco Polo Field, the two estimates were nearly identical. Though, only pre-stack inversion resolved density and provided accurate model that revealed the porosity variations.

Filippova *et al.* (2011) demonstrated with a case study from Timano-Pechora province that reservoir properties could be predicted using geostatistical partial stacks inversion. The results provided high resolution 3D distribution of reservoir properties used to plan production well spacing which was further verified by drilling. Chen *et al.* (2014) used 3D Seismic pre-stack inversion technique to predict fracability attributes in Najmah oil Field, located North Kuwait in Western Asia. Najmah Formation is characterized as unconventional, organic rich shale with less natural fractures.

2.1.1 Simultaneous Inversion

Simultaneous inversion is a sophisticated technique that quantitatively integrates well data and AVA seismic data to produce calibrated 3D volume of rock properties such as P-impedance (Zp), S-impedance (Zs) and density (ρ*)* descriptive of reservoirs. It depends on compressional wave velocity, shear wave velocity, density and angle of incidence. The number of parameters solved for depends on the range of angle stacks and data quality (Berge *et al.*, 2002 and Jason, 2013). Hampson *et al.* (2005) adopted a new approach to the simultaneous pre-stack inversion PP and optional PS angle gathers for the estimation of P-impedance, S-impedance and density to predict the fluid and lithology properties of the sub-surface of the earth based on the assumptions that the linearized approximation for reflectivity holds, that PP and PS reflectivity as a function of angle can be given by the Aki-Richards equations, and that there is a linear relationship between the logarithm of P-impedance and both S-impedance and density. The method was applied to both models and real data sets and the approach works well for modeled gas sand. Contreras *et al.*, 2006 also used measurements acquired in deep water hydrocarbon reservoirs in the central Gulf of Mexico to generate synthetic data to evaluate the AVA simultaneous inversion results on actual field measurements. The results revealed the order of reliability of the inverted distribution of elastic parameters to be P-impedance followed by S-impedance and density. The study further

revealed that sufficient far-angle coverage was crucial for accurate and reliable reconstruction of spatial distribution of S-impedance and density.

2.1.2 Elastic Impedance Inversion

Elastic impedance is an approximation of acoustic impedance for variable incidence angle. It provides a framework to calibrate and invert non- zero-offset seismic data. It allows the well data to be tied directly to the high-angle seismic data which can then be calibrated and inverted without reference to the off-sets data (Connolly, 1999). Inverting for Near and Far elastic volumes provides additional measurement, which will improve prediction of reservoir properties at exploration targets (Veeken and Da Silva, 2004). Elastic impedance approximation is derived from a linearization of the Zoeppritz equation (Aki and Richards, 1980; Connolly, 1999 and Yilmaz, 2002). Nguyen and Larry (2008) used Near-mid-far angle stacks to predict the lithology and pore fluids in target reservoir. Cross plot analysis of AVO intercepts and gradient attributes were used to separate the lithology and fluid responses from the background trend. The result was used to map out specific fluid and lithology characteristics across the entire seismic survey which revealed the brine sands and oil saturated sands in the field.

2.2 Integrated Approach

Accurate prediction of subsurface structures, lithologies and pore fluids is of great interest in petroleum prospecting and reservoir characterization. Seismic reflection data are widely used to mark subsurface structures and lithologies (Miguel *et al*., 2012). However, only seismic data are not sufficient to mark the fluid heterogeneities present in pores. Kong *et al*. (2013) combined simultaneous seismic inversion with elastic impedance inversion for Near and Far angle stacks to reduce uncertainty on bright spot events identified on seismic data in offshore, Myanmar. The

result gave more reliable deductions on recognized seismic features as well as identifying interesting prospects. The inversion products provided vastly improved model of the sub-surface which led to large gas discovery. Adeoti *et al.* (2014) used Amplitude versus offset AVO analysis and forward modeling to predict the fluid type and seismic signature in a deep gas reservoir at 'Faith' Field, Niger Delta. The models used showed that any good quality seismic data acquired over the prospect would be useful in deriving reservoir properties from the identified reservoirs and would be effective in lithologic and hydrocarbon identification.

 Singh *et al.* (2014) conducted pre-stack seismic inversion and amplitude versus angle (AVA) modeling study over an Australian field to reduce the risk in hydrocarbon prospect evaluation. The result led to better reservoir prediction with delineation of sweet spots and improved volumetric prognosis. Khalid *et al.* (2015) also used an integrated seismic interpretation and rock physics attribute analysis for pore fluid discrimination in Ratana area of Northern Potwar, Pakistan. The result showed presence of hydrocarbon and that the reservoirs were capable of hydrocarbon production. Rajagopal *et al.* (2015) developed a joint inversion algorithm to estimate reservoir parameters using both seismic amplitude variation with angle of incidence (AVA) data and marine controlled source electromagnetic (CSEM) data over the North Sea Troll Field. The results provided improved fluid saturation and porosity estimates than the estimates obtained from only AVA or CSEM analysis. Naturally occurring gas hydrate are potential future energy source and since no direct measurements available for quantitative estimation this necessitated the use of effective medium theory and fluid substitution modeling over the sediments of the convergent continental margin of Pakistan. The result showed that some attributes like acoustic and shear impedances and AVO can be used as important proxies to detect gas hydrate saturations (Ehsan *et al.,* 2016).

Integrated techniques have always been used to image subsurface structures in Niger Delta for hydrocarbon exploration but at times results in some great loss (drilling of dry wells) due to small acoustic contrast, fault shadow, lithologies (thinning, thicken, disappearing) between wells of complex geology. Hence, there is need to use integrated technique that could reduce the degree of uncertainty and justify the drilling of exploration wells. This study integrated simultaneous and elastic impedance inversion techniques because of its ability to discriminate lithology and fluid types of subtle features. The reservoir properties estimated will better image and discriminate the lithology and fluid types in 'Sandfish' Field which in turn can guide well placement and reservoir development.

2.3   Location of Study Area

The study area 'Sandfish' Field is located in the near offshore, southwestern Niger Delta. It is situated on the Gulf of Guinea Basin, West Coast of Central Africa and covers about 614.4 km^2. It falls within the latitudes $4^o12'$ to $6^o36'$ N and longitudes $5^o00'$ to $7^o36'$ E of Niger Delta as shown in Figure 1. 'Sandfish' Field extends from about latitudes $5^o12'00''$ to $5^o24'00''$ N and longitude $5^o12'00''$ to $5^o24'00''$ E.
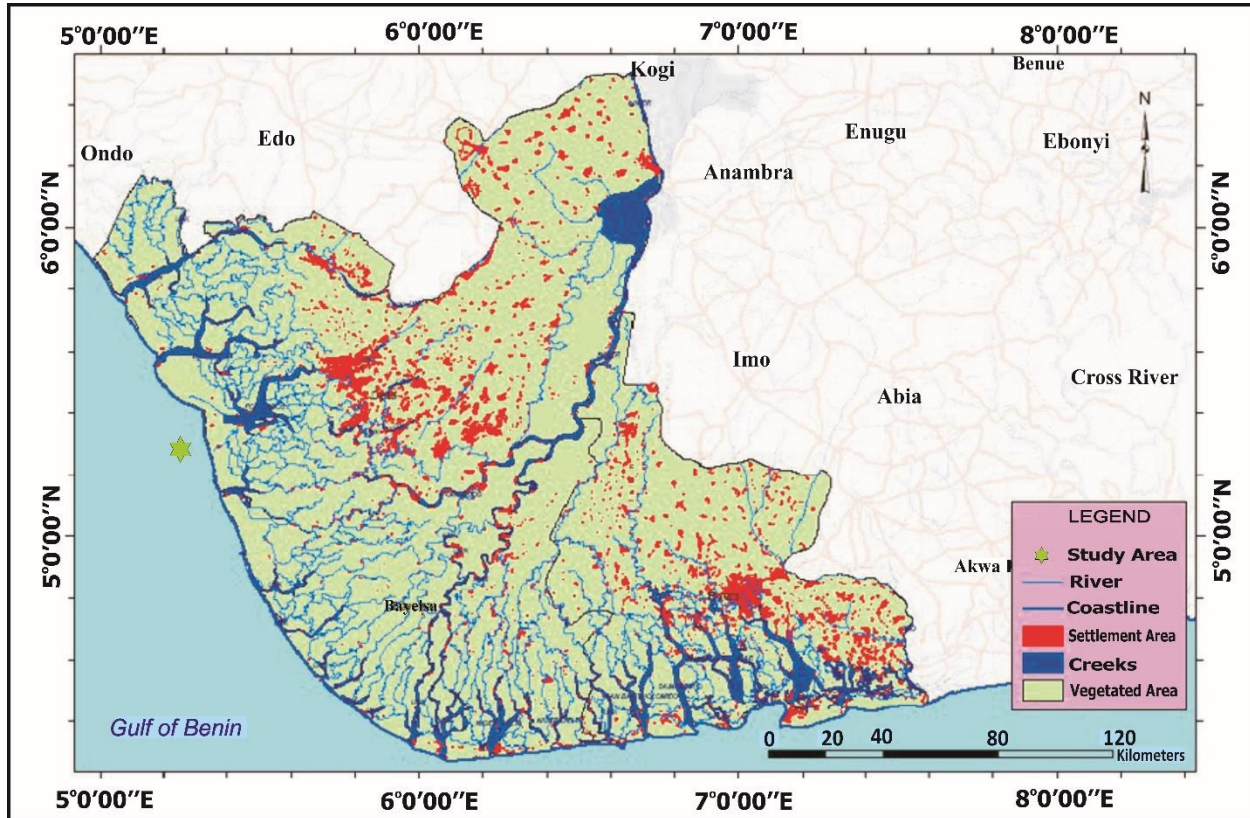
Figure 1: Map of Niger Delta showing the location of the study area.

2.4   Geology of Niger Delta

The Niger Delta is located at the southeastern end of Nigeria, bordering the Atlantic Ocean and extends from about latitudes $4^o\,00'$ to $6^o\,00'$ N and longitudes $3^o\,00'$ to $9^o\,00'$ E (Nwachukwu and Chukwura, 1986), three major stratigraphic units recognized in the Niger Delta oil and natural gas province are the Akata, Agbada and Benin Formations (Short and Stauble, 1967). The Niger Delta region (Figure 2) is known for its proficiency in hydrocarbon production among the sedimentary basins in Nigeria.
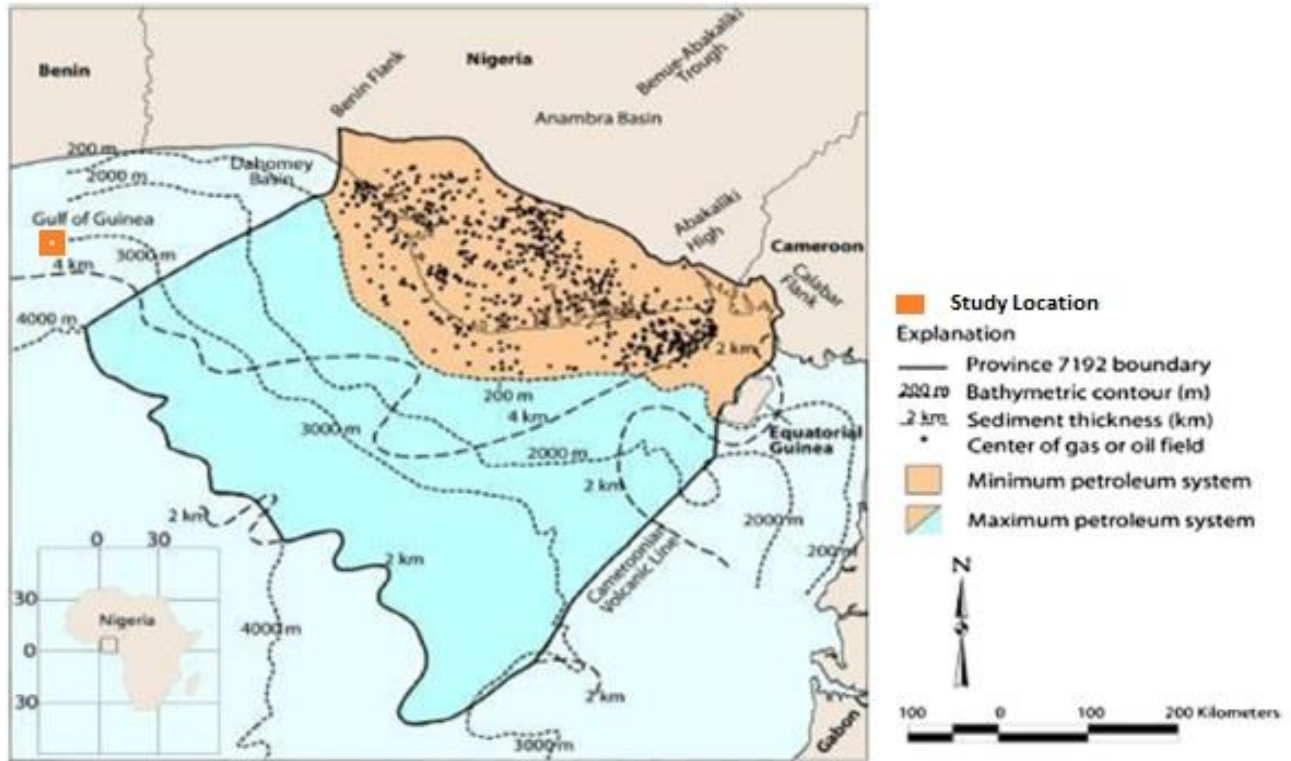
Figure 2: Map of the Niger Delta Province (Tuttle *et al*., 1999).

2.4.1 Stratigraphy

Lithologies of Cretaceous rocks deposited in what is now the Niger Delta Basin can only be extrapolated from the exposed Cretaceous section in the Anambra Basin (Figure 3).

From the Campanian through the Paleocene, the shoreline was concave into the Anambra Basin (Hospers, 1965), resulting in convergent longshore drift cells that produced tide-dominated deltaic sedimentation during transgressions and river-dominated sedimentation during regressions (Reijers *et al*., 1997). Shallow marine clastics were deposited farther offshore and, in the Anambra Basin, are represented by the Albian-Cenomanian Asu River Shale, Cenomanian-Santonian Eze-Uku and Awgu Shales, and Campanian/Maastrichtian Nkporo Shale, among others (Figures 3 and 4) (Nwachukwu, 1972; Reijers *et al.,* 1997). The distribution of Late Cretaceous Shale beneath the Niger Delta is unknown In the Paleocene, a major transgression (referred to as the Sokoto

transgression by Reijers *et al.,* 1997) began with the Imo Shale being deposited in the Anambra Basin to the northeast and the Akata Shale in the Niger Delta Basin area to the southwest (Figure 3). In the Eocene, the coastline shape became convexly curvilinear, the longshore drift cells switched to divergent, and sedimentation changed to being wave-dominated (Reijers *et al.,* 1997). At this time, deposition of paralic sediments began in the Niger Delta Basin proper and, as the sediments prograded south, the coastline became progressively more convex seaward. Today, delta sedimentation is still wave-dominated and longshore drift cells divergent (Burke, 1972). The Tertiary section of the Niger Delta is divided into three formations, representing prograding depositional facies that are distinguished mostly on the basis of sand-shale ratios. The type sections of these formations are described in Short and Stauble (1967) and summarized in a variety of papers (Avbobvo, 1978; Doust and Omatsola, 1990; Kulke, 1995). The Akata Formation at the base of the Delta is of marine origin and is composed of thick shale sequences (potential source rock), turbidite sand (potential reservoirs in deep water), and minor amounts of clay and silt (Figures 3, 4, and 5). Beginning in the Paleocene and through the Recent, the Akata Formation formed during lowstands when terrestrial organic matter and clays were transported to deep water areas characterized by low energy conditions and oxygen deficiency (Stacher, 1995).

Deposition of the overlying Agbada Formation is the major petroleum-bearing unit. It began in the Eocene and continues into the Recent (Figures 3, 4, and 5). The formation consists of paralic siliciclastics over 3700 meters thick and represents the actual deltaic portion of the sequence. The clastics accumulated in delta-front, delta-topset, and fluvio-deltaic environments. In the lower Agbada Formation, shale and sandstone beds were deposited in equal proportions, however, the upper portion is mostly sand with only minor shale interbeds. The Agbada Formation is overlain

by the third formation, the Benin Formation, a continental latest Eocene to Recent deposit of alluvial and upper coastal plain sands that are up to 2000 m thick (Avbovbo, 1978).
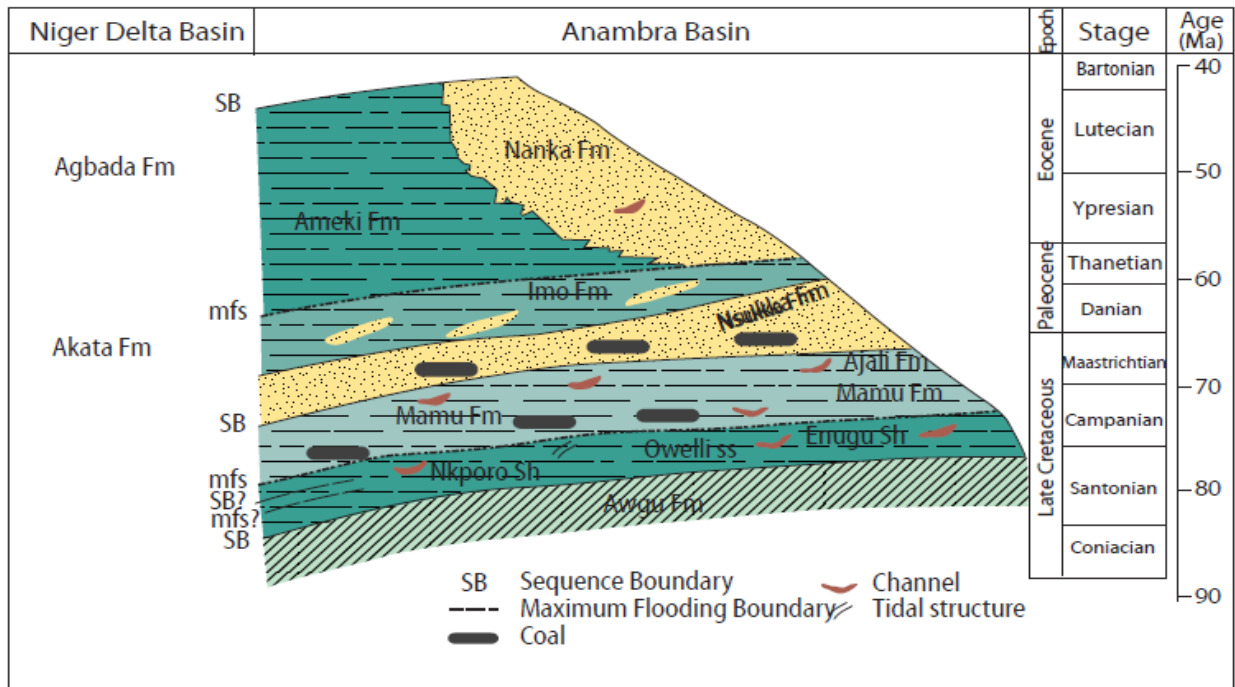
Figure 3: Stratigraphic Section of the Anambra Basin from the Late Cretaceous through the Eocene and time equivalent formations in the Niger Delta (Reijers *et al.*, 1997).
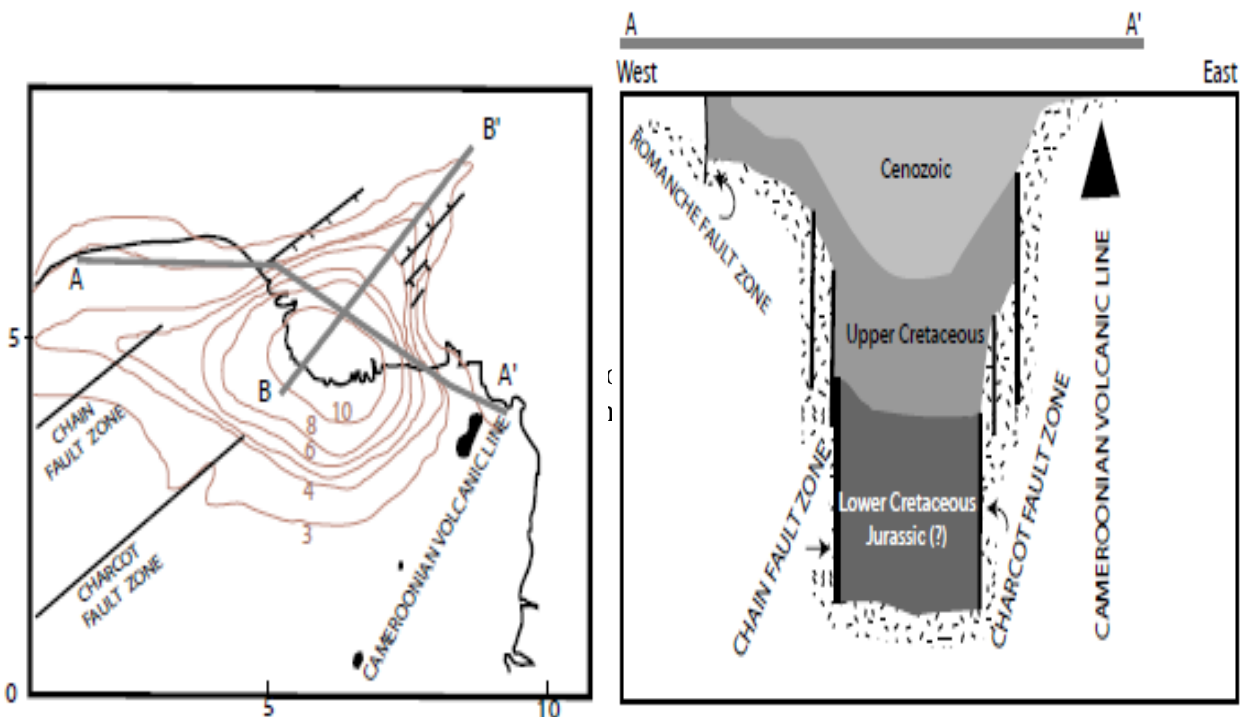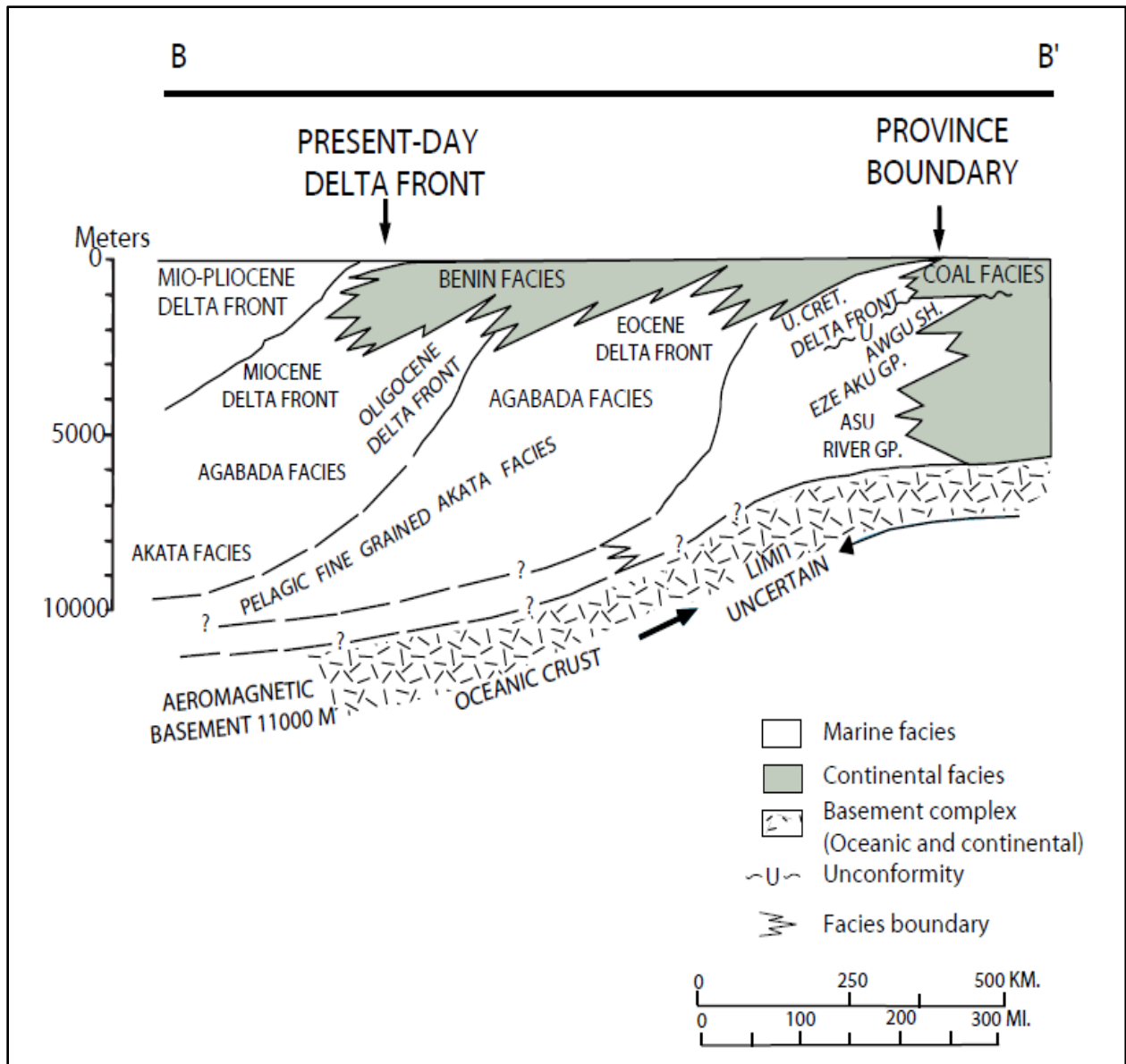
Figure 4: East-West (A-A') and Southwest-Northeast (B-B') cross sections through the Niger Delta Region; revealing sediment thickness and continental basement (Kaplan *et al*., 1994; Whiteman, 1982).
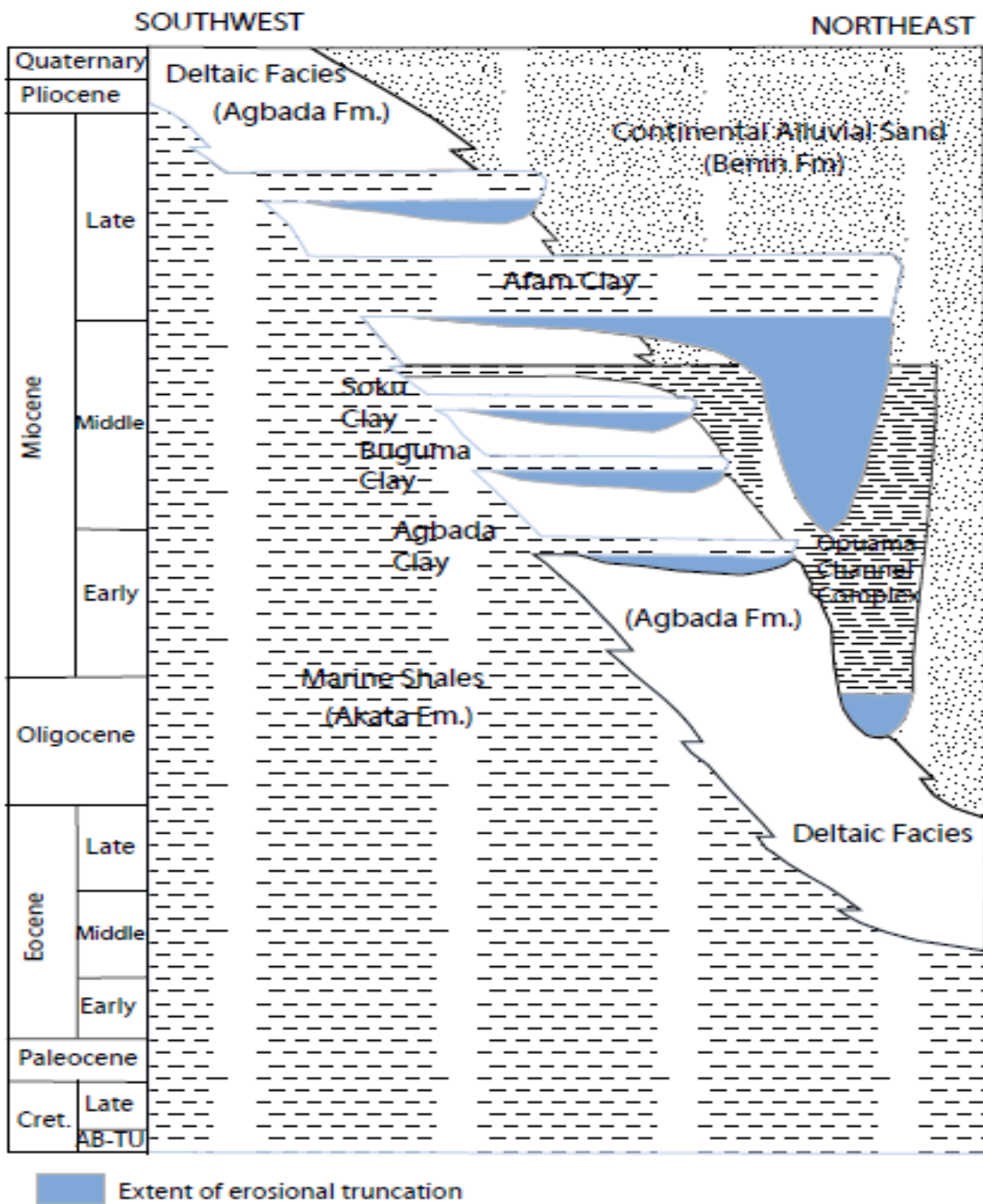
Figure 5: Stratigraphic column of the Niger Delta (Shannon and Naylor, 1989; Doust and Omatsola, 1990).

2.4.2   Structural Geology

The province covers 300,000 km^2 and includes the Tertiary Niger Delta Akata-Agbada Petroleum System. The tectonic framework of the continental margin along the West Coast of equatorial Africa is controlled by Cretaceous fracture zones expressed as trenches and ridges in the deep Atlantic. The fracture zone ridges subdivide the margin into individual basins, and in Nigeria, this form the boundary faults of the Cretaceous Benue-Abakaliki trough, which cuts far into the West African shield. In this region, rifting started in the Late Jurassic and persisted into the Middle Cretaceous (Lehner and De Ruiter, 1977). In the region of the Niger Delta, rifting diminished altogether in the Late Cretaceous as shown in Figure 6. First, shale diapirs formed from loading of poorly compacted, over-pressured, prodelta and delta-slope clays (Akata Formation) by the higher density delta-front sands (Agbada Formation). Second, slope instability occurred due to a lack of lateral, basin-ward, support for the under-compacted delta-slope clays (Akata Formation). For any given depobelt, gravity tectonics were completed before deposition of the Benin Formation and are expressed in complex structures, including shale diapirs, roll-over anticlines, collapsed growth fault crests, back-to-back features, and steeply dipping, closely spaced flank faults (Evamy *et al*., 1978; Xiao and Suppe, 1992). These faults mostly offset different parts of the Agbada Formation and flatten into detachment planes near the top of the Akata Formation.
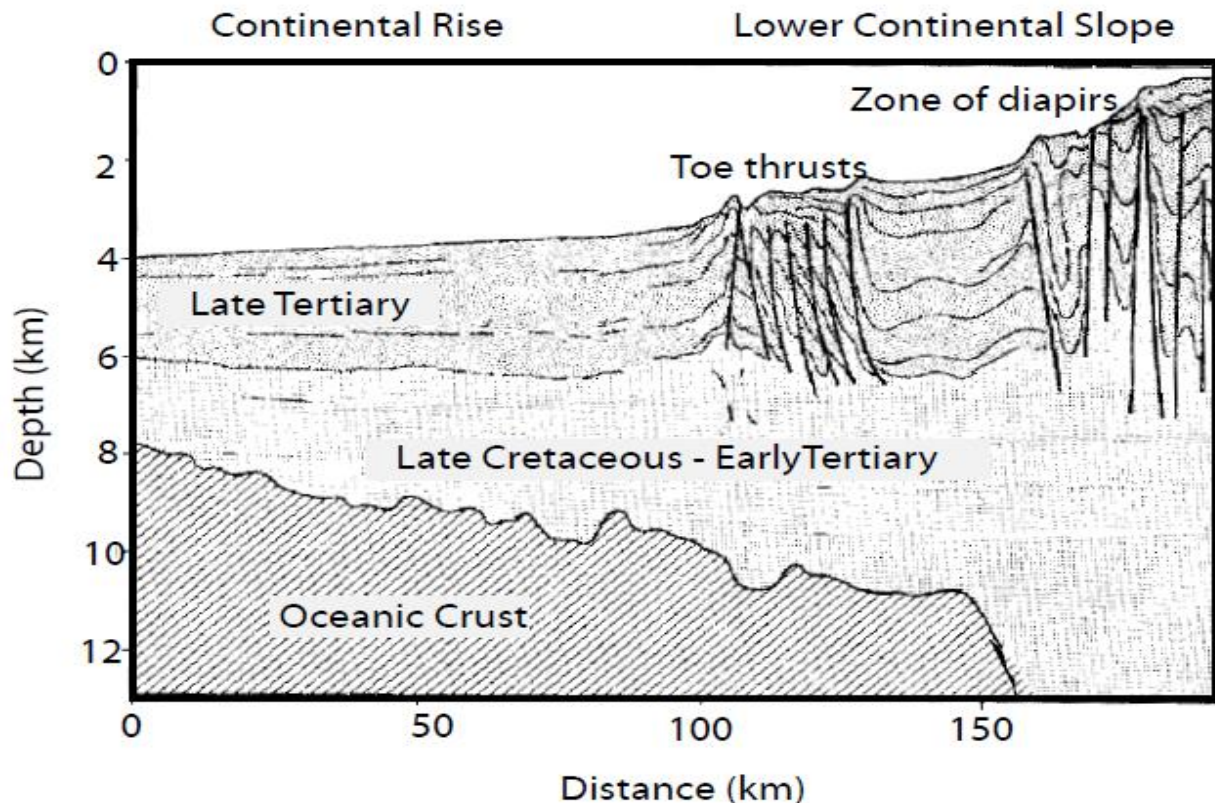
Figure 6: Niger Delta Distal Portion of Depobelt (Lehner and De Ruiter, 1977; Doust and Omatsola, 1990).

2.4.3 Petroleum System

2.4.3.1 Source Rock

There has been much discussion about the source rock for petroleum in the Niger Delta (Evamy *et al.*, 1978; Ekweozor *et al.,* 1979; Ekweozor and Okoye, 1980; Lambert-Aikhionbare and Ibe, 1984; Bustin, 1988; Doust and Omatsola, 1990). Possibilities include variable contributions from the marine interbedded Shale in the Agbada Formation and the marine Akata Shale, and a Cretaceous shale (Weber and Daukoru, 1975; Evamy *et al.,* 1978; Ekweozor and Okoye, 1980; Ekweozor and Daukoru, 1984; Lambert-Aikhionbare and Ibe, 1984; Doust and Omatsola, 1990; Stacher, 1995; Frost, 1977; Haack *et al.*, 1997).

The Agbada Formation has intervals that contain organic carbon contents sufficient to be considered good source rocks (Ekweozor and Okoye, 1980; Nwachukwu and Chukwura, 1986). The intervals, however, rarely reach thickness sufficient to produce a world-class oil province and are immature in various parts of the Delta (Evamy *et al.,* 1978; Stacher, 1995). The Akata Shale is present in large volumes beneath the Agbada Formation and is at least volumetrically sufficient to generate enough oil for a world class oil province such as the Niger Delta.

2.4.3.2 Petroleum Origination and Migration

Evamy *et al.* (1978) set the top of the present-day oil window in the Niger Delta at the 240°F (115° C) isotherm. In the northwestern portion of the Delta, the oil window (active source-rock interval) lies in the upper Akata Formation and the lower Agbada Formation as shown in Figure 7. To the southeast, the top of the oil window is stratigraphically lower (up to 4000' below the upper Akata/lower Agbada sequence; Evamy *et al.,* 1978). Some researchers (Nwachukwu and Chukwura, 1986; Doust and Omatsola, 1990; Stacher, 1995) attribute the distribution of the top of the oil window to the thickness and sand/shale ratios of the overburden rock (Benin Formation and variable proportions of the Agbada Fm.). The sandy continental sediment (Benin Fm.) has the lowest thermal gradient (1.3 to 1.8°C/100 m); the paralic Agbada Formation has an intermediate gradient (2.7°C/100 m); and the marine, over-pressured Akata Formation has the highest (5.5°C/100 m) (Ejedawe *et al.,* 1984). Therefore, within any depobelt, the depth to any temperature is dependent on the gross distribution of sand and shale. If sand/shale ratios were the only variable, the distal offshore subsurface temperatures would be elevated because sand percentages are lower. To the contrary, the depth of the hydrocarbon kitchen is expected to be deeper than in the delta proper, because the depth of oil generation is a combination of factors (temperature, time, and deformation related to tectonic effects) (Beka and Oti, 1995).

Migration from mature, over-pressured shales in the more distal portion of the delta may be similar to that described from over-pressured shales in the Gulf of Mexico. Hunt (1990) relates episodic expulsion of petroleum from abnormally pressured, mature source rocks to fracturing and resealing of the top seal of the over-pressured interval. In rapidly sinking Basins, such as the Gulf of Mexico, the fracturing/ resealing cycle occurs in intervals of thousands of years. This type cyclic expulsion is certainly plausible in the Niger Delta Basin where the Akata Formation is over-pressured. Beta and Oti (1995) predict a bias towards lighter hydrocarbons (gas and condensate) from the over-pressured shale as a result of down-slope dilution of organic matter as well as differentiation associated with expulsion from over-pressured sources.
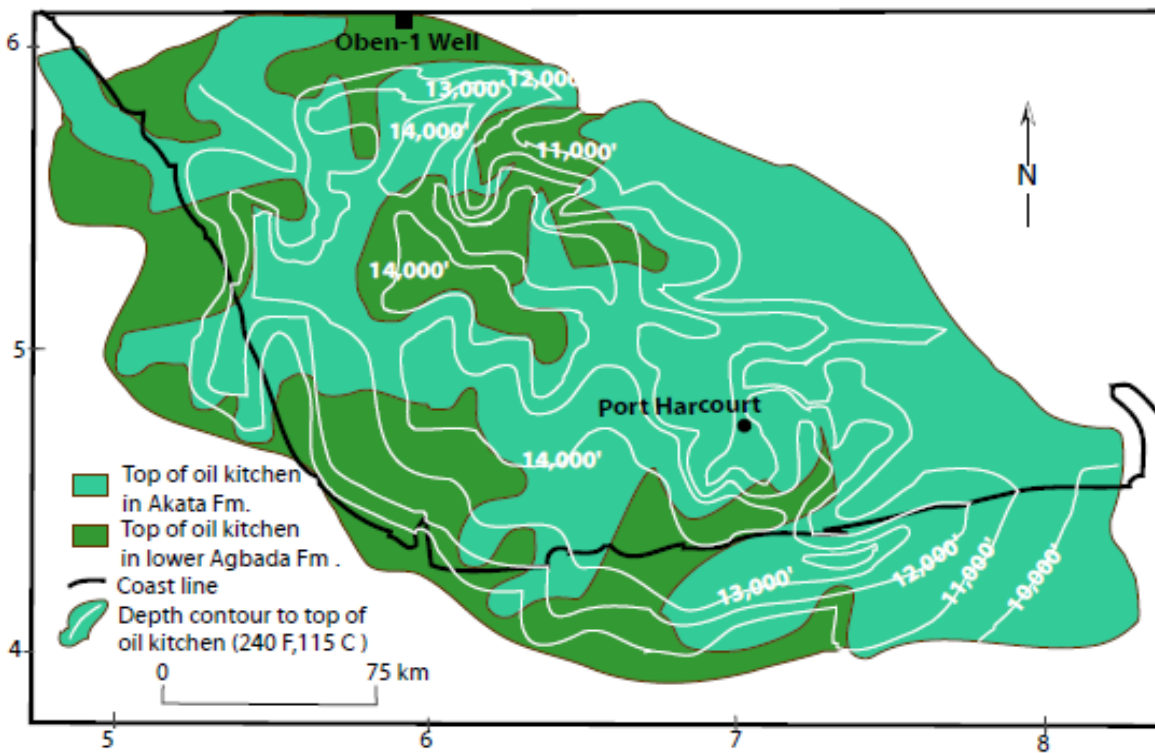
Figure 7: Subsurface depth to top of Niger Delta oil kitchen in Akata and lower Agbada Formation (Evamy _et al.,_ 1978).

2.4.3.3 Reservoir Rock

Petroleum in the Niger Delta is produced from sandstone and unconsolidated sands predominantly in the Agbada Formation. Characteristics of the reservoirs in the Agbada Formation are controlled by depositional environment and by depth of burial. Known reservoir rocks are Eocene to Pliocene in age, and are often stacked, ranging in thickness from less than 15 meters to 10% having greater than 45 meters thickness (Evamy *et al.*, 1978). The thicker reservoirs likely represent composite bodies of stacked channels (Doust and Omatsola, 1990). Based on reservoir geometry and quality, Kulke (1995) describes the most important reservoir types as point bars of distributary channels and coastal barrier bars intermittently cut by sand-filled channels. Edwards and Santogrossi (1990) describe the primary Niger Delta reservoirs as Miocene paralic sandstones with 40% porosity, 2 darcys permeability, and a thickness of 100 meters. The lateral variation in reservoir thickness is strongly controlled by growth faults; the reservoir thickens towards the fault within the down-thrown block (Weber and Daukoru, 1975). The grain size of the reservoir sandstone is highly variable with fluvial sandstones tending to be coarser than their delta front counterparts; point bars fine upward, and barrier bars tend to have the best grain sorting. Much of this sandstone is nearly unconsolidated, some with a minor component of argillo-silicic cement (Kulke, 1995). Porosity only slowly decreases with depth because of the young age of the sediment and the coolness of the delta complex.

In the outer portion of the delta complex, deep-sea channel sands, low-stand sand bodies, and proximal turbidites create potential reservoirs (Beka and Oti, 1995). Burke (1972) describes three deep-water fans that have likely been active through much of the delta's history (Figure 8). The fans are smaller than those associated with other large deltas because much of the sand of the2 Niger-Benue system is deposited on top of the delta, and buried along with the proximal parts of

the fans as the position of the successive depobelts moves seaward (Burke, 1972). The distribution, thickness, shaliness, and porosity/ permeability characteristics of these fans are poorly understood (Kulke, 1995).

Tectono-stratigraphy computer experiments show that local fault movement along the slope edge controls thickness and lithofacies of potential reservoir sands downdip (Smith-Rouch *et al.,* 1996). The slope-edge fault simulation from these experiments is shown in Figure 9. Smith-Rouch (1998) states that "by extrapolating the results to other areas along the shelf margin, new potential reservoirs are identified."
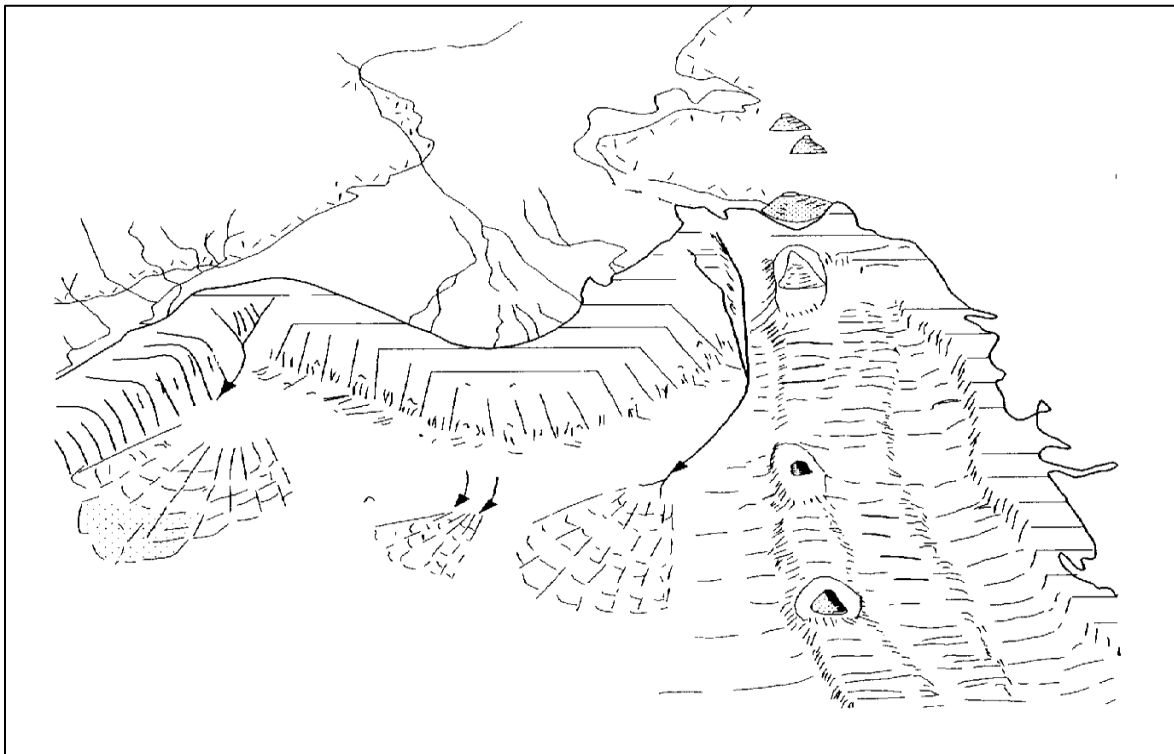
Figure 8: Deep marine sediments in the Gulf of Guinea off the Niger Delta (Modified from Burke, 1972 and Reijers *et al*., 1997).
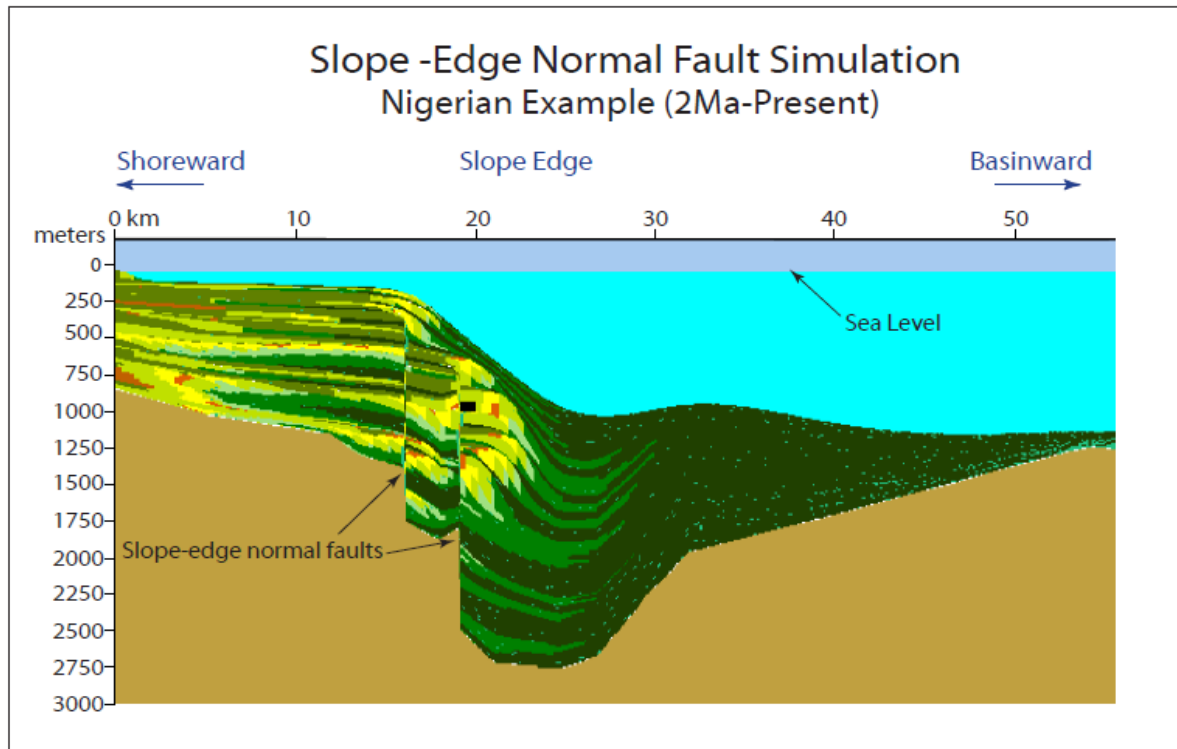
Figure 9: Slope edge normal fault simulation (2Ma-present) for the Niger Delta. Bright intervals are sands (Tuttle *et al.,* 1999).

2.4.3.4 Trap

Most of the traps in Niger Delta are structural although stratigraphic traps are equally common (Figure 10). The structural traps are formed during synsedimentary deformation of the Agbada paralic sequence (Tuttle *et al*., 1999; Evamy *et al*., 1978; Stacher, 1995). The structural complexity increases from the earlier formed depobelts in the north to the later formed depobelts in the south in response to increasing instability of the under-compacted, over-pressured shale (Doust and Omatsola, 1990).

On the flanks of the delta, pockets of sandstone occur between diapiric structures. Towards the delta tow (base of distal slope), this alternating sequence of sandstone and shale gradually grades to essentially sandstone.
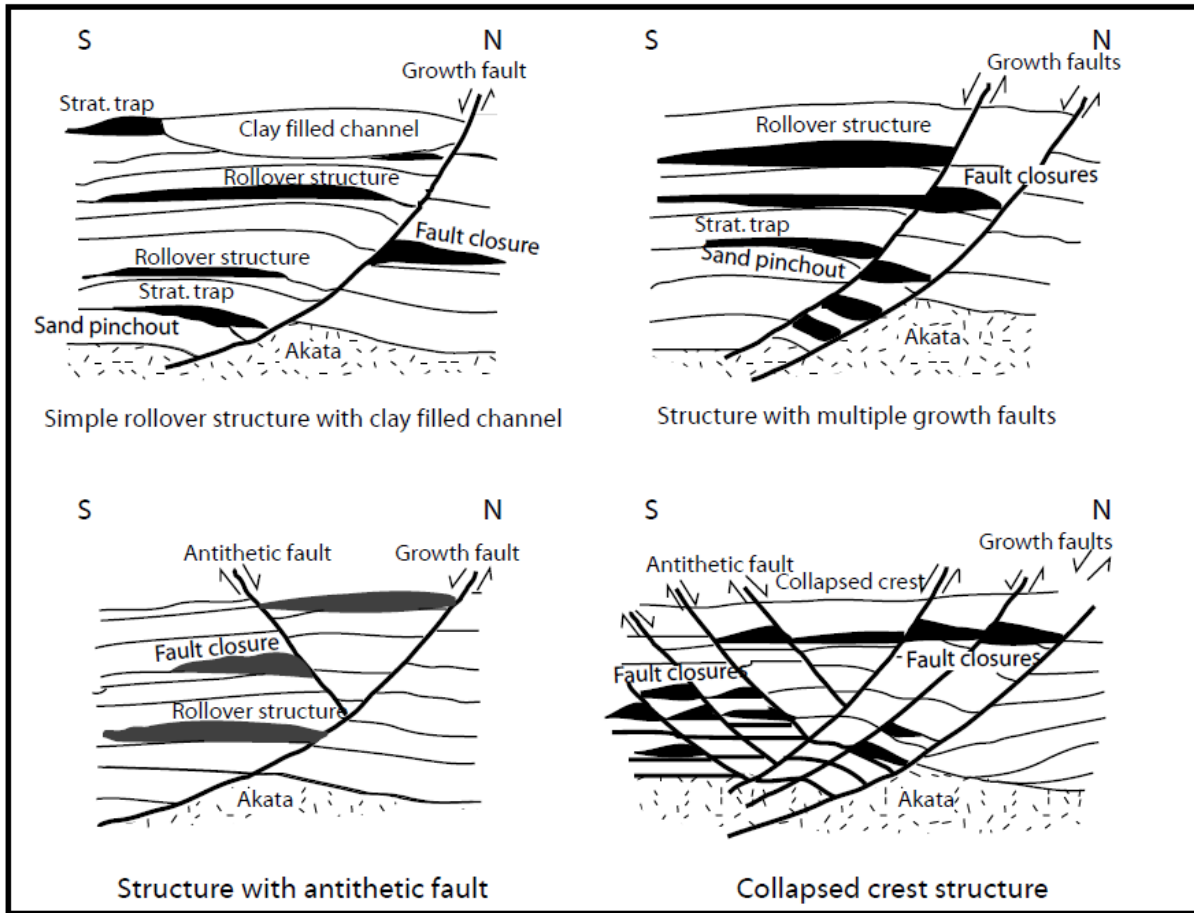
Figure 10: Niger Delta oil field structures and associated trap types (Doust and Omatsola, 1990; Stacher, 1995).

2.4.3.5 Seal

The primary seal rock in the Niger Delta is the interbedded shale within the Agbada Formation. The shale provides three types of seals – clay smears along faults, interbedded sealing units against which reservoir sands are juxtaposed due to faulting, and vertical seals (Doust and Omatsola, 1990; Tuttle *et al*., 1999). Major erosional events of early to middle Miocene age forming canyons that are now clay-filled on the flanks of the delta (Figure 6). These clays form the top seals for some important offshore fields (Doust and Omatsola, 1990).

2.5 Theoretical Concepts

2.5.1 Basic AVO/AVA Theory and Equations

When seismic waves travel into the earth and encounter layer boundaries with velocity (V) and density (ρ) contrasts, the energy of the incident wave is partitioned at each boundary as shown in Figure 12. Part of the incident energy associated with compressional source is converted to shear wave. The compressional (P) and shear wave (SV) energy are partly reflected and transmitted through each layer boundaries. The fraction of the incident energy reflected depends on the incidence angle. The analysis of seismic reflection amplitude as a function of incidence angle (AVA) allows better assessment of reservoir rock properties for hydrocarbon detection, lithology identification and fluid prediction (Feng and Bancroft, 2006).
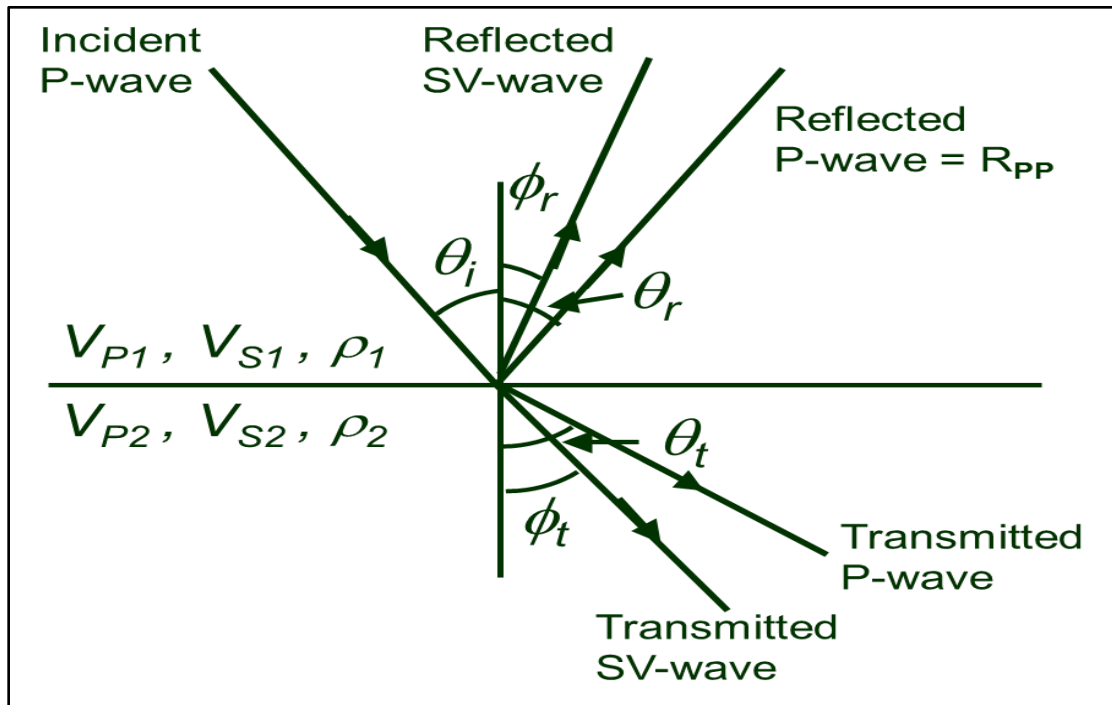
Figure 11: Wave energy reflections at surface boundary (Feng and Bancroft, 2006).

2.5.2 Seismic Reflection Theory

Seismic reflection technique has become a key tool for oil and gas industry, revealing shapes of subsurface structures and indicating drilling targets. Changes in the character of seismic pulses returning from a reflector could be used to ascertain rock type in a layer and the nature of pore fluid. The general expressions for the reflection of compressional and shear waves at a boundary as a function of densities and velocities of the layers in contact are credited to Karl Zoeppritz. Karl Zoeppritz found that amplitudes increase, decrease or remain constant with changing angle of incidence, depending on the contrast in density (ρ), compressional velocity (V_P), and shear velocity (V_S) across the boundary. The ability of rock to pass the elastic wave is called acoustic impedance. Acoustic impedance depends on velocity and density as expressed in equation 1.

$$Z = \rho * V \qquad\qquad\qquad 1$$

where;

Z is Acoustic impedance, ρ is Bulk density and V is Velocity of medium.

When a compressional seismic wave arrives vertically at a horizontal interface, the amplitude of the reflected wave is proportional to the amplitude of the incoming wave, thus the normal incidence reflection coefficient is expressed as equation 2 (Montazeri, 2013).

$$R_i = \frac{Z_{i+1} - Z_i}{Z_{i+1} + Z_i} \qquad\qquad\qquad 2$$

where;

Z_i = Acoustic impedance of layer i[th] (first layer)

Z_{i+1} = Acoustic impedance of the second layer i[th]

R_i = Reflection coefficient of the layer i[th]

When a seismic wave arrives obliquely, the compressional reflection coefficient is a function of angle of incidence, densities (ρ), compressional velocity (V_P) and shear velocity (V_S) of the two layers in contact as expressed by Karl Zoeppritz in equation 3.

$$
\begin{bmatrix} r_P \\ r_S \\ T_P \\ T_S \end{bmatrix} = \begin{bmatrix} -\sin\theta_1 & -\cos\phi_1 & \sin\theta_2 & \cos\phi_2 \\ \cos\theta_1 & -\sin\phi_1 & \cos\theta_2 & -\sin\phi_2 \\ \sin 2\theta_1 & \dfrac{V_{P1}}{V_{S1}}\cos 2\phi_1 & \dfrac{\rho_2 V_{S2}^2 V_{P1}}{\rho_1 V_{S1}^2 V_{P2}}\cos 2\phi_1 & \dfrac{\rho_2 V_{S2} V_{P1}}{\rho_1 V_{S1}^2}\cos 2\phi_2 \\ -\cos 2\phi_1 & \dfrac{V_{S1}}{V_{P1}}\sin 2\phi_1 & \dfrac{\rho_2 V_{P2}}{\rho_1 V_{P1}}\cos 2\phi_2 & -\dfrac{\rho_2 V_{S2}}{\rho_1 V_{P1}}\sin 2\phi_2 \end{bmatrix}^{-1} \begin{bmatrix} \sin\theta_1 \\ \cos\theta_1 \\ \sin 2\theta_1 \\ \cos 2\phi_1 \end{bmatrix}
$$
3

r_P, r_S, T_P, T_S are the reflected P and reflected S, transmitted P and transmitted S wave amplitude coefficients.

Aki-Richard Approximation

The Aki-Richard (1980) approximate equation of Zoeppritz formula expressed in equation 4 was used in this study. This was used because it allows the estimation of three parameters (Z_P, Z_S and ρ). The reflection coefficient (R_{PP}) was obtained from the linear combination of the three elastic parameters P –wave velocity, S-wave velocity and density. This approximation of the Zoeppritz's equation is only valid for small angles and it assumes a horizontal layered earth model (Aki and Richards, 2002).

$$
R_{pp}(\theta) \approx \frac{1}{2}\left(\frac{\Delta Vp}{Vp} + \frac{\Delta\rho}{\rho}\right) + \left(\frac{1}{2}\frac{\Delta Vp}{Vp} - \frac{Vs^2}{Vp^2}\left(\frac{\Delta\rho}{\rho} + \frac{\Delta Vs}{Vs}\right)\right)\sin^2\theta + \frac{1}{2}\frac{\Delta Vp}{Vp}(\tan^2\theta - \sin^2\theta)
$$
4

or

$$R_{pp}(\theta) \approx \frac{1}{2}\left(\frac{\Delta Vp}{Vp} + \frac{\Delta\rho}{\rho}\right) - \left(\frac{Vs^2}{Vp^2}\left(\frac{\Delta\rho}{\rho} + \frac{\Delta Vs}{Vs}\right)\right)\sin^2\theta + \frac{1}{2}\frac{\Delta Vp}{Vp}(\tan^2\theta) \qquad 5$$

or

$$R_{pp}(\theta) \approx \frac{1}{2}(1 + \tan^2\theta)\frac{\Delta\alpha}{\alpha} - \left(4\frac{\beta^2}{\alpha^2}\sin^2\theta\right)\frac{\Delta\beta}{\beta} + \left(\frac{1}{2}\left(1 - 4\frac{\beta^2}{\alpha^2}\sin^2\theta\right)\right)\frac{\Delta\rho}{\rho} \qquad 6$$

Where;

$$\text{P-impedance term} = \frac{1}{2}(1 + \tan^2\theta)\frac{\Delta\alpha}{\alpha}$$

$$\text{S-impedance term} = -\left(4\frac{\beta^2}{\alpha^2}\sin^2\theta\right)\frac{\Delta\beta}{\beta}$$

$$\text{Density term} = \left(\frac{1}{2}\left(1 - 4\frac{\beta^2}{\alpha^2}\sin^2\theta\right)\right)\frac{\Delta\rho}{\rho}$$

The equation 6 can be expressed in simpler form as equation 7;

$$R_{pp}(\theta) \approx A + B\sin^2\theta + C\sin^2\theta\tan^2\theta \qquad 7$$

where;

$R_{pp}(\theta)$ = reflection coefficient at a given angle.

θ = average of the incidence and transmission angles at a plane reflecting interface.

A = Intercept; it's the normal incidence reflection coefficient.

B = AVO Gradient; it describes the variation at intermediate offsets.

C = AVO curvature; it dominates at far offsets near the critical angle.

Shuey's Approximation

Shuey (1985) published a closed form approximation of the Zeoppritz equations stated in equation 8

$$R(\theta) = R_P + G \sin^2 \theta \qquad\qquad 8$$

where

$R(\theta)$ = Seismic reflection coefficient at a given angle

R_P = AVO intercept

G = AVO Gradient

Elastic Impedance Approximations

The variation of impedance with angle of incidence is termed Elastic impedance and it is expressed in equation 9

$$R_{EI} = \frac{1}{2}\frac{\Delta EI(\theta)}{EI(\theta)} \approx \frac{1}{2}\Delta \ln EI(\theta) \qquad\qquad 9$$

Conolly's Equation

The Elastic impedance according to conolly (1999) can be estimated using equation 10

$$\mathbf{EI}(\boldsymbol{\theta}) = \alpha^a \beta^b \rho^c \qquad\qquad 10$$

Whitcombe's Equation

The Elastic impedance according to Whitcombe (2002) can be estimated using equation 11

$$\mathbf{EI}(\boldsymbol{\theta}) = \boldsymbol{\alpha_0 \rho_0} \left[\left(\left(\frac{\alpha}{\alpha_0}\right)^a \left(\frac{\beta}{\beta_0}\right)^b \left(\frac{\rho}{\rho_0}\right)^c\right)\right] \qquad\qquad 11$$

where

α = compressional velocity, β =Shear velocity, ρ = density
and $\alpha_0, \beta_0, \rho_0$ are constant reference values

$a = 1 + \tan^2 \theta$, $b = -8K\sin^2 \theta$, $c = 1 - 4K\sin^2 \theta$ and $K = \left(\frac{\beta}{\alpha}\right)^2$.

2.5.3 P-wave velocity (V_P) and S-Wave Velocity (V_S)

Seismic waves induce elastic deformation along the propagation path in the subsurface. The fundamental elastic waves that propagate in the earth are the compressional waves (P-waves) and the shear waves (S-waves). When a P-wave is applied to a unit of rock it will change the volume

and shape of the rock but when S-wave is applied it will only change the shape. Seismic wave velocity is grouped according to how the wave travels and propagates. P-waves are waves with particle motion in the direction of wave propagation having the highest velocity for a given medium and are called Primary waves while S-waves are waves with particle motion perpendicular to the direction of the wave propagation and are called Secondary waves. Relationship between P-wave (V_P) and S-wave (V_S) is expressed as equations 12 and 13.

$$V_P = \sqrt{\frac{\lambda + 2\mu}{\rho}} = \sqrt{\frac{K + \frac{4}{3}\mu}{\rho}} \qquad\qquad 12$$

$$V_S = \sqrt{\frac{\mu}{\rho}} \qquad\qquad 13$$

where:

λ = Lambda coefficient

K = Bulk modulus

μ = Shear modulus

ρ = Density

2.5.4 Poisson ratio (σ)

Poisson's ratio expresses the ratio between the strain parallel to a compressional or tensile stress, and the strain perpendicular to that stress. Changes in the Poisson's ratio can occur due to pore fluid changes and it can be calculated as shown in equations 14 and 15 (Montazeri, 2013).

$$\sigma = \frac{\gamma - 2}{2(\gamma - 1)} = \frac{(\frac{V_P}{V_S})^2 - 2}{2(\frac{V_P}{V_S})^2 - 2} \qquad\qquad 14$$

where:

σ is Poisson's ratio and γ is $\left(\dfrac{V_P}{V_S}\right)^2$ 15

V_P is Compressional wave velocity and V_S is Shear wave velocity.

2.5.5 Lambda-rho ($\lambda\rho$)

Lambda-rho or Incompressibility can be estimated from the square difference of P-impedance and S-impedance expressed in equation 16. It is a fundamental property that is easier to understand its connection to reservoir properties compared to the traditional seismic attributes like amplitude and velocity (Gray and Anderson, 2000). Lambda-rho can be used as an indicator for both lithology and pore fluid. Low Incompressibility values are associated with gas sand (Goodway *et al*., 1997).

$$\lambda\rho = Z_s{}^2 - Z_s{}^2 \qquad\qquad\qquad 16$$

where;

$\lambda\rho$ = Lambda-rho (Incompressibility)

Z_p = P-impedance

Z_s = S-impedance

$Z_p{}^2 = (\rho V_P)^2 = (\lambda + 2\mu)\rho$

$Z_s{}^2 = (\rho V_S)^2 = \mu\rho$

2.5.6 Mu-rho ($\mu\rho$)

Mu-rho or Rigidity is sensitive to rock's matrix and not influenced by fluid. It can therefore be used for lithology indicator. Mu-rho can be estimated from the product of shear modulus and density as expressed in equation 17. Low rigidity values are associated with coals/shales while high values indicate sands (Goodway *et al*., 1997).

$$Z_S{}^2 = (\rho V_S)^2 = \mu\rho \text{ (Rigidity)} \qquad\qquad 17$$

2.5.7 Density (ρ)

Density is a mass per unit volume with the unit kg/m^3. It is a parameter used in this study for P-wave, S-wave and acoustic impedance equations where they all give impact on how subsurface seismic responds. Density values drop in hydrocarbon reservoirs compare to non-hydrocarbon reservoirs. This characteristic property is very important for seismic interpretation to enhance hydrocarbon discovery and production.

2.5.8   Porosity (ϕ)

Porosity is related to rock properties, it is known as the ratio of pore volume to bulk volume. It ranges from 0 to 1 and could also be expressed in percentage (0% - 100%) as reflected in Table 1 (Etu-Efeotor, 1997). The porosity values do not give any information about the size and distribution of pores or its connection.

Table 1: Qualitative Evaluation of Porosity (Etu-Efeotor, 1997)

Percentage Porosity	Quality Evaluation
0 – 5	Negligible
5 – 10	Poor
15 – 20	Good
20 – 25	Very Good
Over 30	Excellent

2.5.9 The Biot Gassman Theory

The Biot-Gassmann modeling theory (Gregory, 1977) is used for AVO analysis. By importing the P-wave velocities and densities of rocks with the known porosity and water saturation, new P and S-wave velocities and densities based on new porosity or water saturation values could be derived. In this calculation, equations 18 and 19, some parameters such as bulk modulus of the water, hydrocarbon and matrix are known

$$K_{sat} = K_{dry} + \left\{ \frac{\beta^2}{[(\frac{\emptyset}{K_f}) + (\frac{\beta - \emptyset}{K_m})]} \right\} \qquad\qquad 18$$

where $\beta = 1 - (\frac{K_{dry}}{K_m})$ = Biot coefficient $\qquad\qquad 19$

K_{sat} : Bulk modulus of saturated rock

K_f: Bulk modulus of the fluid; known

K_{bulk}: Bulk modulus of dry rock

K_m: Bulk modulus of mineral components; known

By using V_p -V_s values, equation 19 could be re-written into equation 20

$$K_{sat} = \rho_{sat}V_p{}^2 - (\frac{4}{3}\rho_{sat}V_s{}^2) \qquad\qquad 20$$

2.5.10 Fluid Replacement modeling (Frm)

FRM modules allow one to see how changing certain properties within different fluid could vary the logs values and explain the petrophysical concepts. The different rock properties are investigated in the synthetic and the real models to interpret variations (HRS Documentation).

Fluid substitution is an important part of seismic attribute studies because it provides the interpreter with a valuable tool for modeling various fluid scenarios, which might explain an observed

amplitude variation with offset anomaly (Smith *et al.*, 2003). The Biot-Gassmann modeling theory will be used for fluid substitution in this study.

2.5.11 AVO Classifications

Based on Rutherford and Williams (1989) classification, there are three main classes of AVO anomalies (Figure 12). Class I sands have higher impedance than the encasing shale, with relatively large positive zero-offset reflection coefficient (Ro). Class II sands have nearly the same impedance as the encasing shale and are characterized by near-zero Ro. Class III sands have lower impedance than the encasing shale with large negative values for Ro. It was demonstrated by Castagna and Swan (1997) that the same gas sand produces very different AVO behaviour depending on its overlying shale, and it would therefore be incorrect to classify a reflector based on the property of sand alone. They proposed Class IV, low impedance gas sand with negative reflection coefficient, which decreases with offset (Figure 13). These four responses were also classified based on the position of AVO anomalies on the A-B plane, as shown in Figure 13.
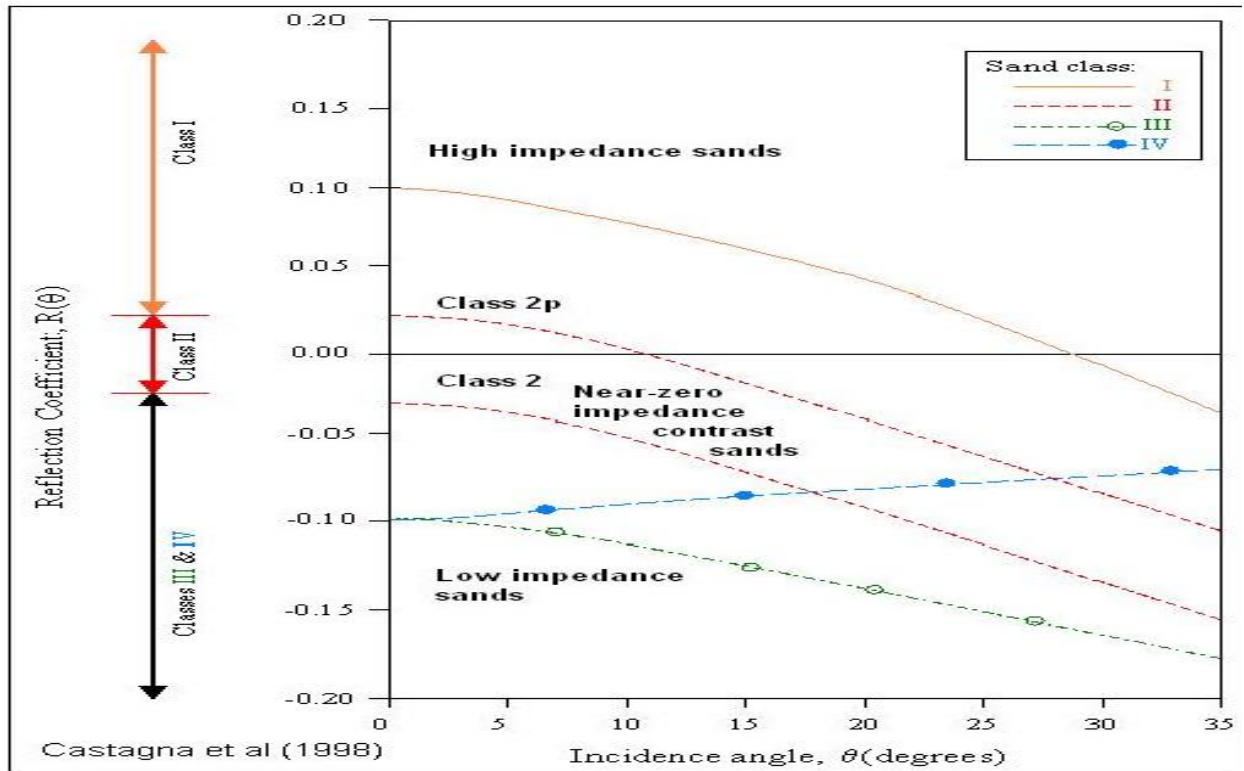
Figure 12: AVO Classes- Plot of seismic reflection coefficient against incidence angle (Rutherford and Williams, 1989).
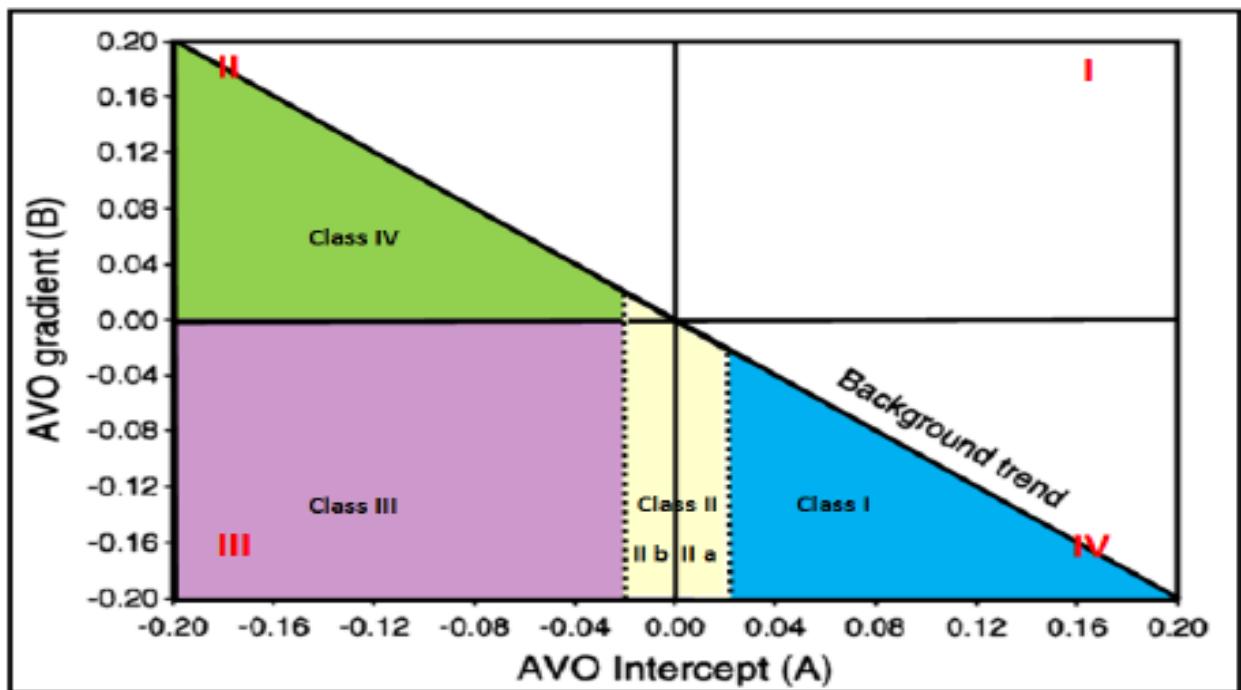
Figure 13: Plot of AVO Gradient (B) against AVO Intercept (A) (Castagna and Swan, 1997).

Table 2 summarizes the characteristics of each AVO class as it is being plotted on different quadrants, the corresponding A-B value and whether the offset is decreasing or increasing is used to study the AVO behavior of gas sands.

Table 2: AVO Behaviour for Gas Sands (modified from Castagna and Swan, 1997)

Class	Relative Impedance	Quadrant	A	B	Amplitude vs. Offset
I	Higher that overlying unit	IV	+	-	Decreases
II	About the same as the overlying unit	III, or IV	+ or -	-	Increase or decrease may change sign
III	Lower than overlying unit	III	-	-	Increase
IV	Lower than overlying unit	II	-	+	Decreases

CHAPTER THREE

3.0 MATERIALS AND METHODS

3.1 DATA GATHERING

The data used for this study were obtained from Chevron Nigeria Limited with permission of the Department of Petroleum Resources (DPR), Lagos. The data were acquired from 'Sandfish' Field in Niger Delta, Southern Nigeria. The data include;

1. 3D seismic data of five angle stacks (6°- 12°, 12°- 18°, 18°- 26°, 26°- 32° and 32°-42°) with zero-degree phase rotation at 25Hz dominant frequency from 'Sandfish' Field.

2. Wells (01, 02, 04 and 05) with petrophysical logs (P-sonic, S-sonic, gamma, resistivity, density, water saturation and volume of shale).

3. Interpreted horizons (E01, K01, N01 and P01) and check shots.
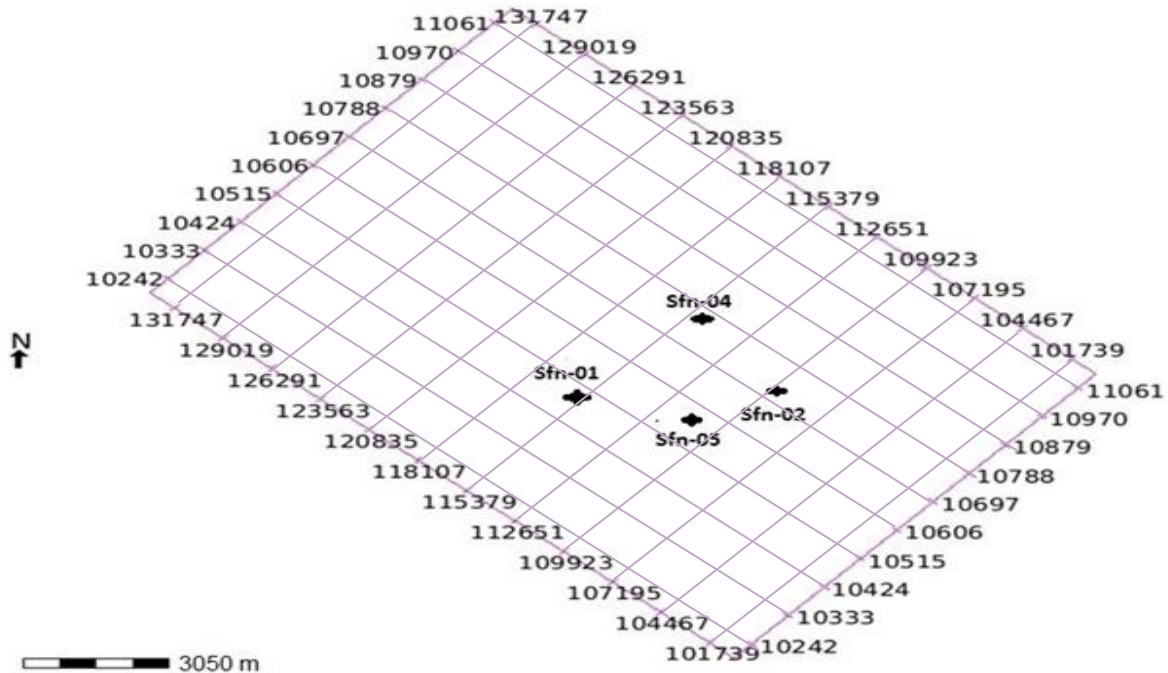
Figure 14: Base Map of 'Sandfish' field showing the seismic coverage and the well locations.

3.2 DATA LOADING

The data set were loaded into Jason (8.3c version) and Hampson Russell (9.0 version) software programs. The seismic data was loaded in SEG-Y format while the well data and check shots were loaded in ASCII format. The interpreted seismic horizons were equally loaded. The quality of each data was checked and reformatted to ensure the proper import and calibration.

3.3 DATA VALIDATION AND QUALITY CONTROL (QC)

3.3.1 Seismic Data and QC

3D seismic data of five partial angle stacks ranging from (6°- 12°) with bandwidth frequency of approximately (6 to 55) Hz were used for the inversion. The seismic sampling interval used is 4 ms with seismic survey in-lines (10248-11064) and cross lines (101739-131747) spaced by 25 m and 1 m respectively. Figure 15 shows good seismic data import because the peak of the amplitude is at zero (Jason, 2013). Figures 16a is the seismic amplitude section while 16b is seismic frequency section for the near and far-far stacks. Figure 17 is the amplitude alignment of near and far-far stacks. This Quality Control (QC) helps to check the consistency of the seismic amplitude and frequency content of data.
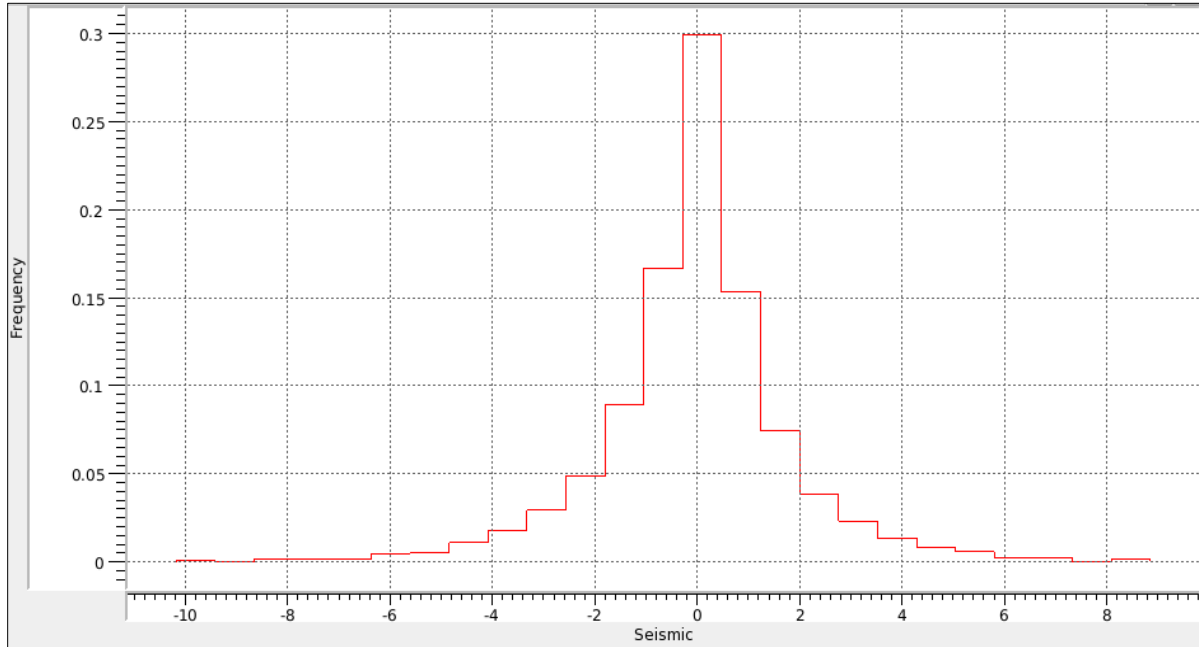
Figure 15: Seismic (near stack) data import with the peak amplitude at zero of the histogram.
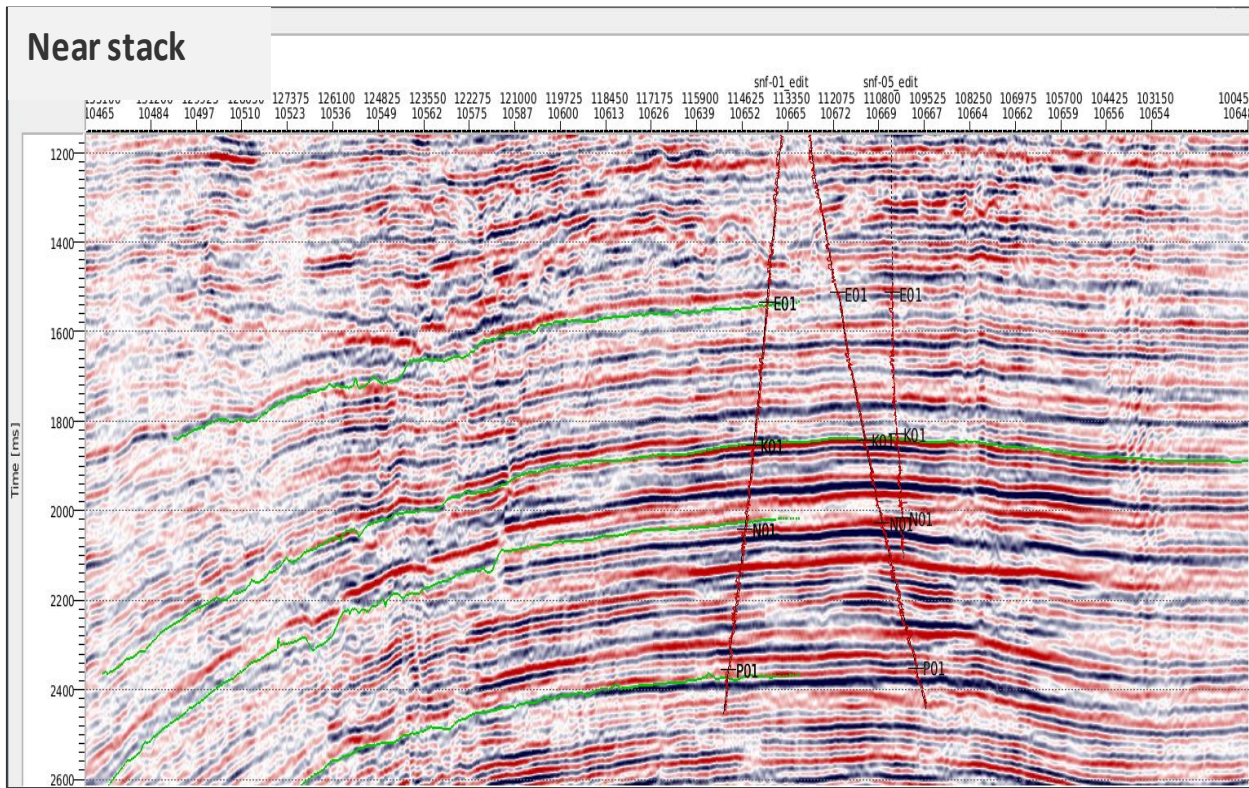
Figure 16a: Near stack with Sfn (01, 02 and 05) and the four interpreted horizons.
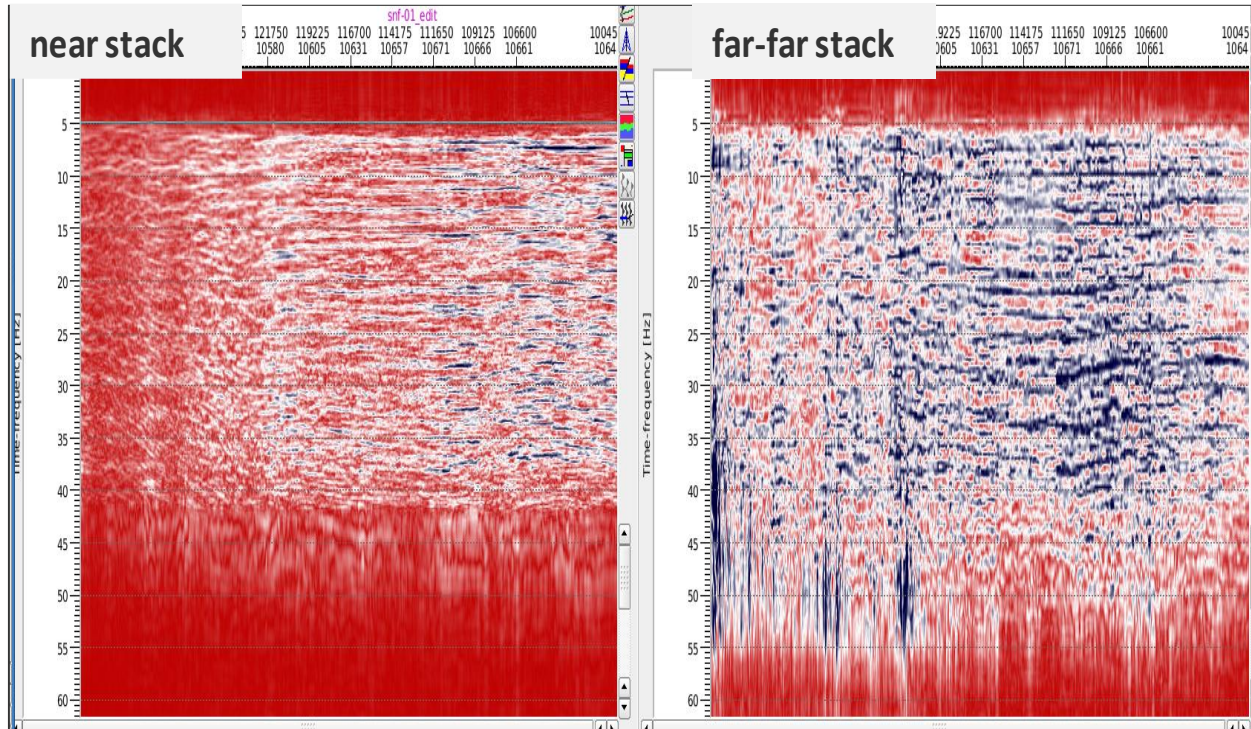
Figure 16b: Fairly constant frequency spectrum from Near to Far-far stack.
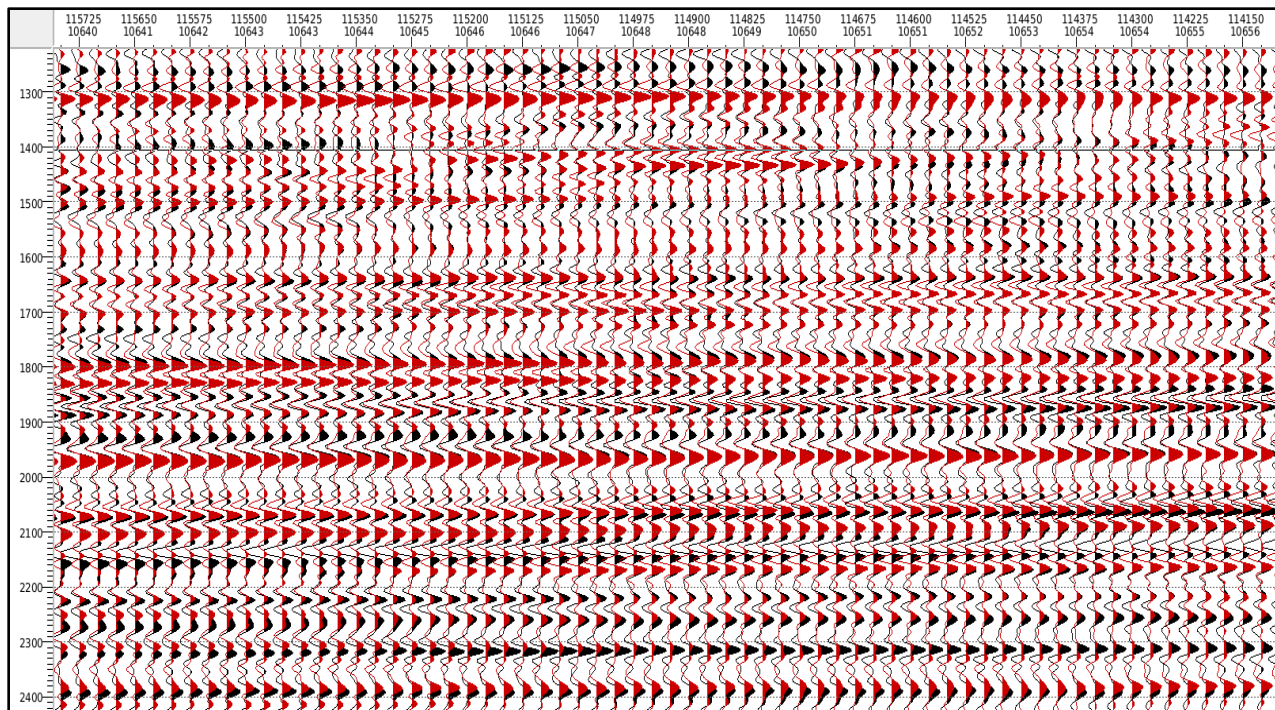
Figure 17: Far-far (red wiggle) amplitude spectrum overlain on the near (black wiggle) Amplitude spectrum.

3.**3.2 Well Data and QC**

The 'Sandfish' Field well data consisted of four wells but only three wells (Sfn-01, Sfn-02, Sfn-05) with the required petrophysical logs (Vp, Vs, density, porosity, gamma, resistivity and water saturation) were used in the inversion. The Sfn-04 was used to validate inversion products away from well control as a blind test. Figure 18 is the display of the well logs. All the wells used are deviated. The wells were displayed in TVD (True vertical depth) though represents TVDSS (True vertical depth sub-sea). The sonic (Vp and Vs) and density logs were used to generate P-impedance and S-impedance values at each well while the combination of gamma ray and resistivity logs was used for qualitative interpretation (in picking the sand tops at the zones of interest). The check shot was used for the time-depth conversion.
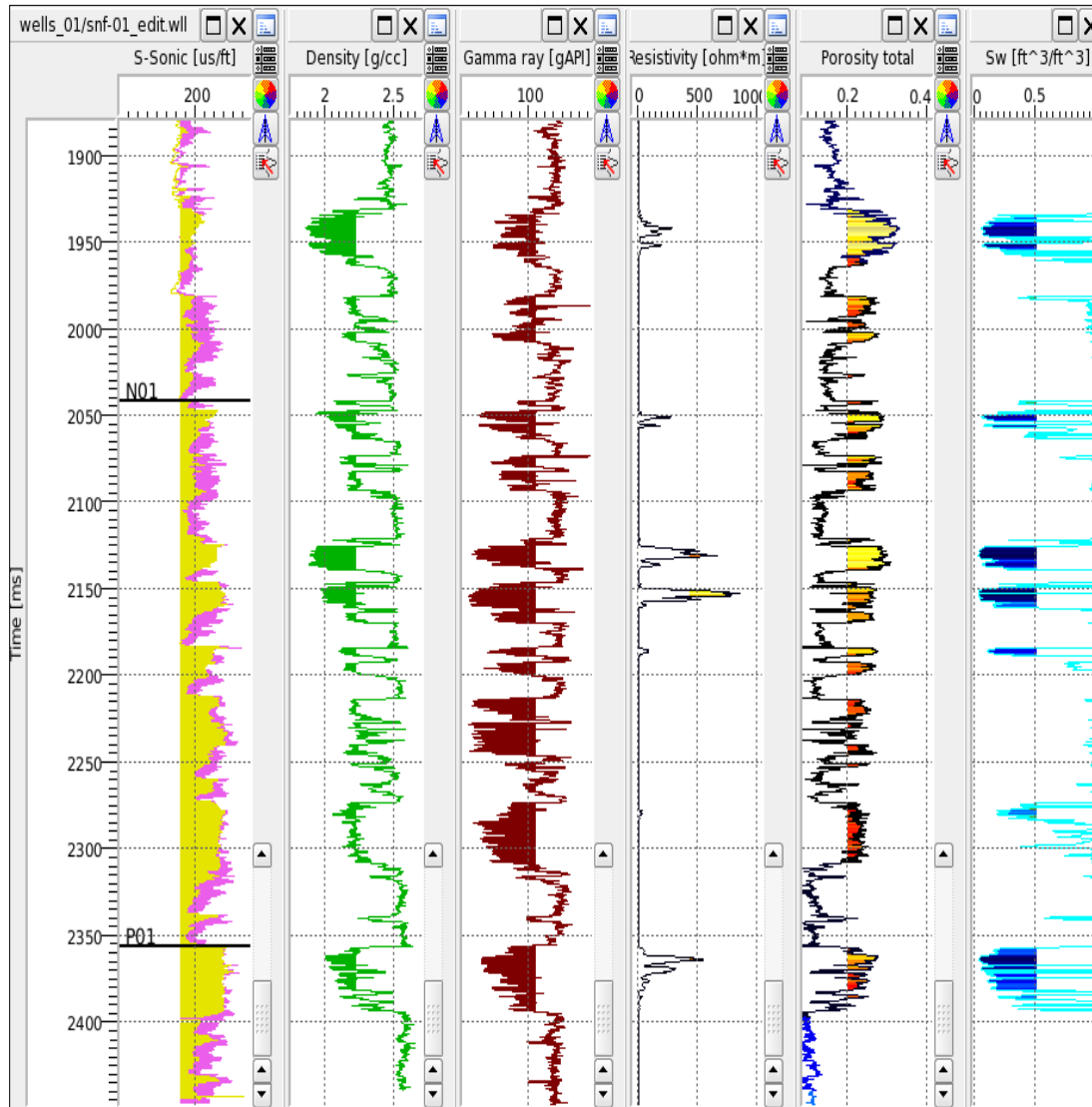
Figure 18: Well Sfn-01 with displayed P- Sonic log (pink), S- Sonic log (gold), Density log (green), Gamma-ray log (brown), Resistivity log (black), Porosity log (brownish-yellow) and Water saturation log (cyan) with Sand tops (black marker).

3.3.3 Horizon

The interpreted four horizons (E01, N01, P01, K01) ranging from 1500 to 2500 ms were correlated to the well logs. The correlation of gamma ray and resistivity logs with the seismic section (seismic horizons) was used to identify tops of the sand used for seismic inversion.

Figure 19 is the display of the interpreted horizons used in the study. E01 is the shallowest horizon of the field, K01 is the second horizon, and N01 is the third horizon which is the most promising zone while P01 is the deepest horizon. The impedance logs guided by the four interpreted horizons were used to create the low frequency model, which in turn was used to constrain the inversion process.
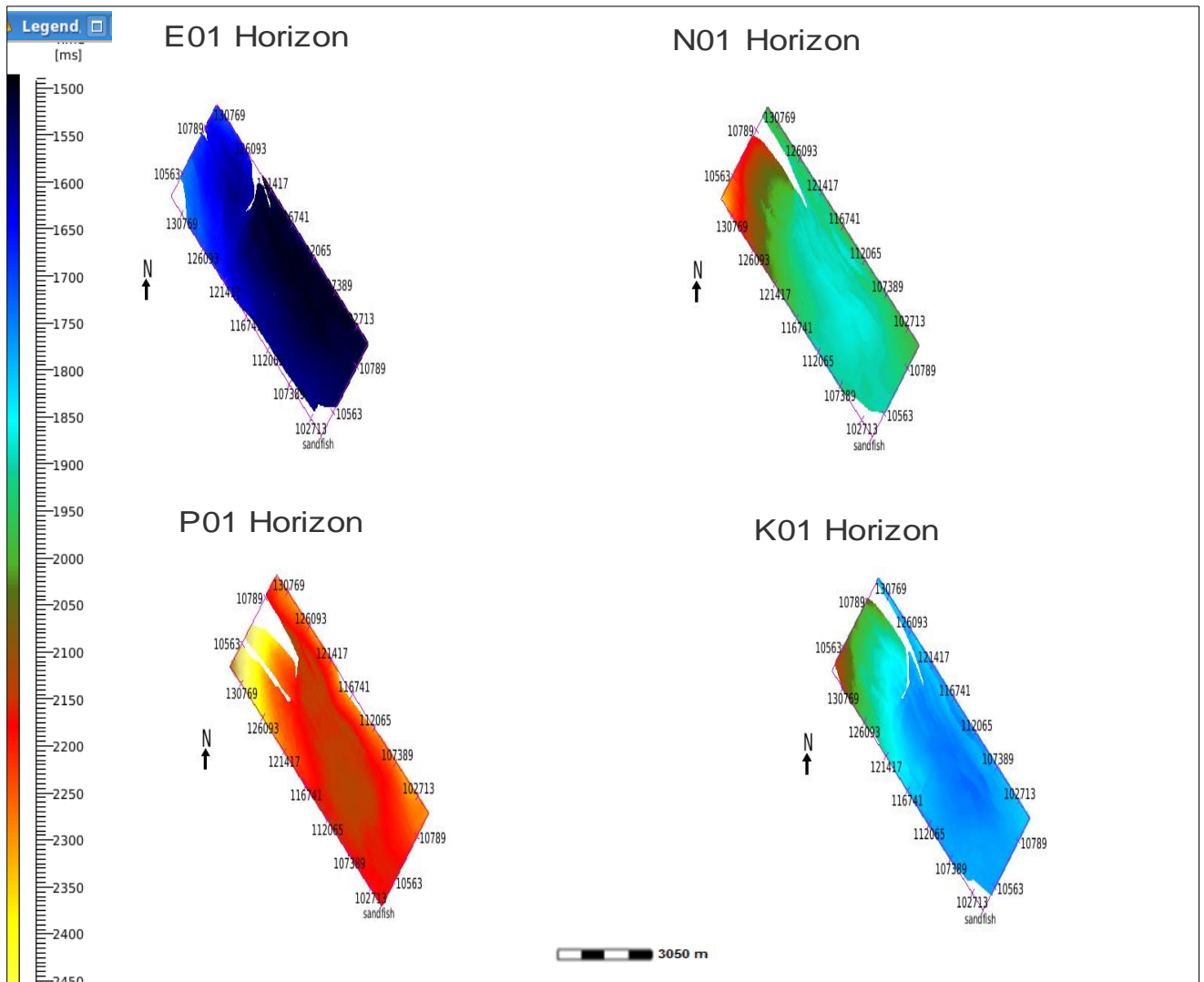
Figure 19: Interpreted Horizons (E01, K01, N01 and P01).

3.3.4 Correlation of Seismic and Well Data

The well to seismic tie for wells Sfn-01, Sfn-02, and Sfn-05 was achieved by convolving well reflectivity series computed with Aki-Richards (1980) equation from the impedance logs with the estimated wavelets from each of the partial angle stacks to generate a synthetic trace. The seismogram generated from each of the five angle stacks were then matched with the corresponding angle stack to get the best tie. The best tie was achieved by correlating the seismic data and synthetic trace.

In this study wavelets were extracted from seismic data at an interval of 1500 – 2500 ms with a wavelength 100 ms and taper length 25 with minimized unwanted lobes. The near (6°-12°) stack tie with wells (Sfn-01, Sfn-02 and Sfn-05) are displayed in Figures 22 (a-c) while the near mid, mid, far and far-far stacks tie with Sfn-01, Sfn-02 and Sfn-05 are displayed in Figures 20 (d-o) in Appendix A. The near (6°-12°) stack with Sfn-05 had the best tie with correlation coefficient of 77% shown in Figure 20c. The angle stack is displayed in the first panel, synthetic data in second panel, correlation coefficient in third panel while Z_P and Z_S logs are displayed in fourth panel Figures 20 (a-c). The extracted wavelets from each of the five angle stacks are displayed in Figures 21 (a-c).
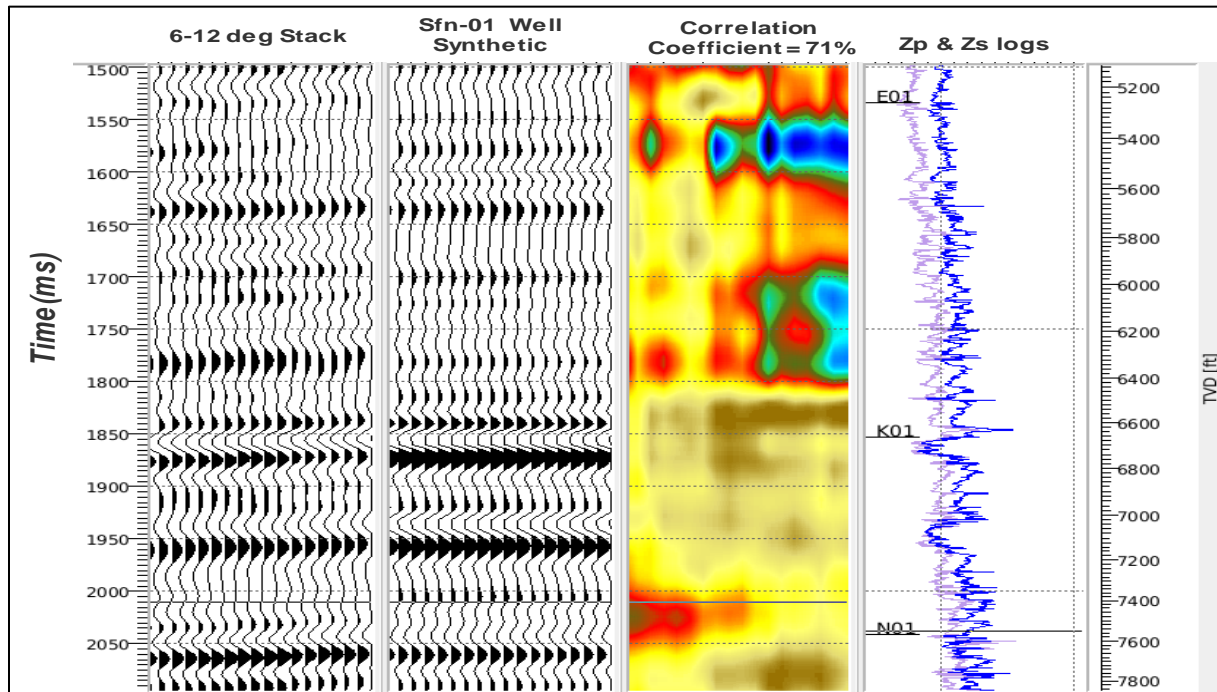
Figure 20a: Seismic to well tie using the near (6°-12°) stack and Sfn-01.
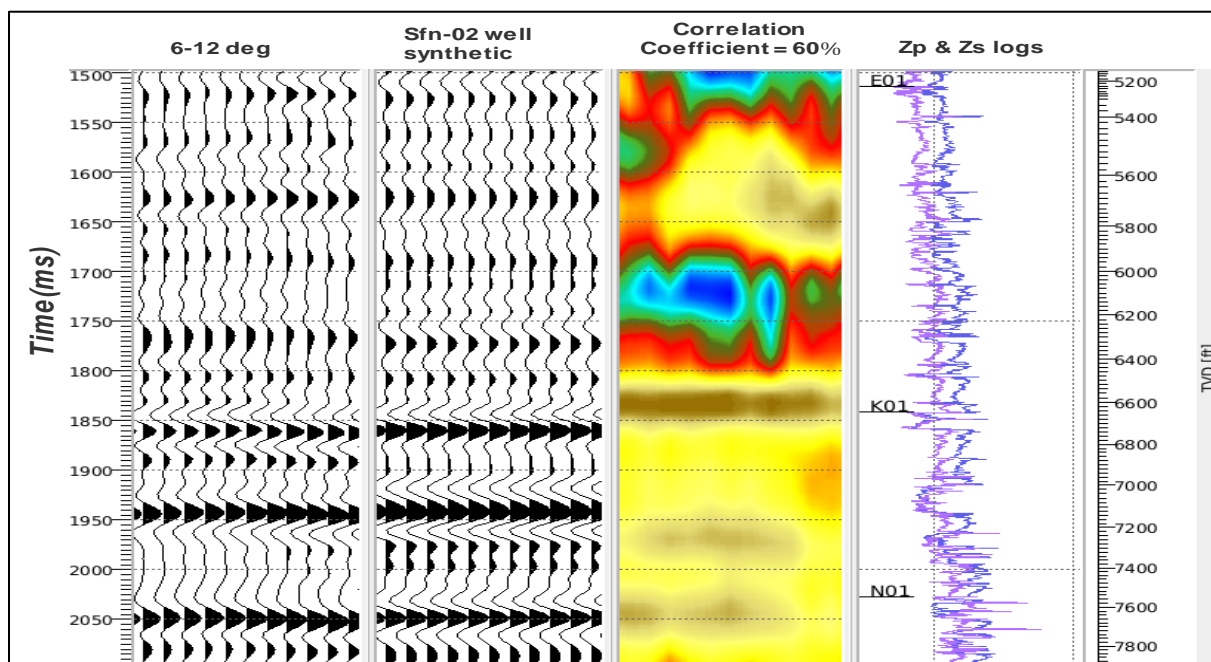
Figure 20b: Seismic to well tie using the near (6°-12°) stack and Sfn-02.
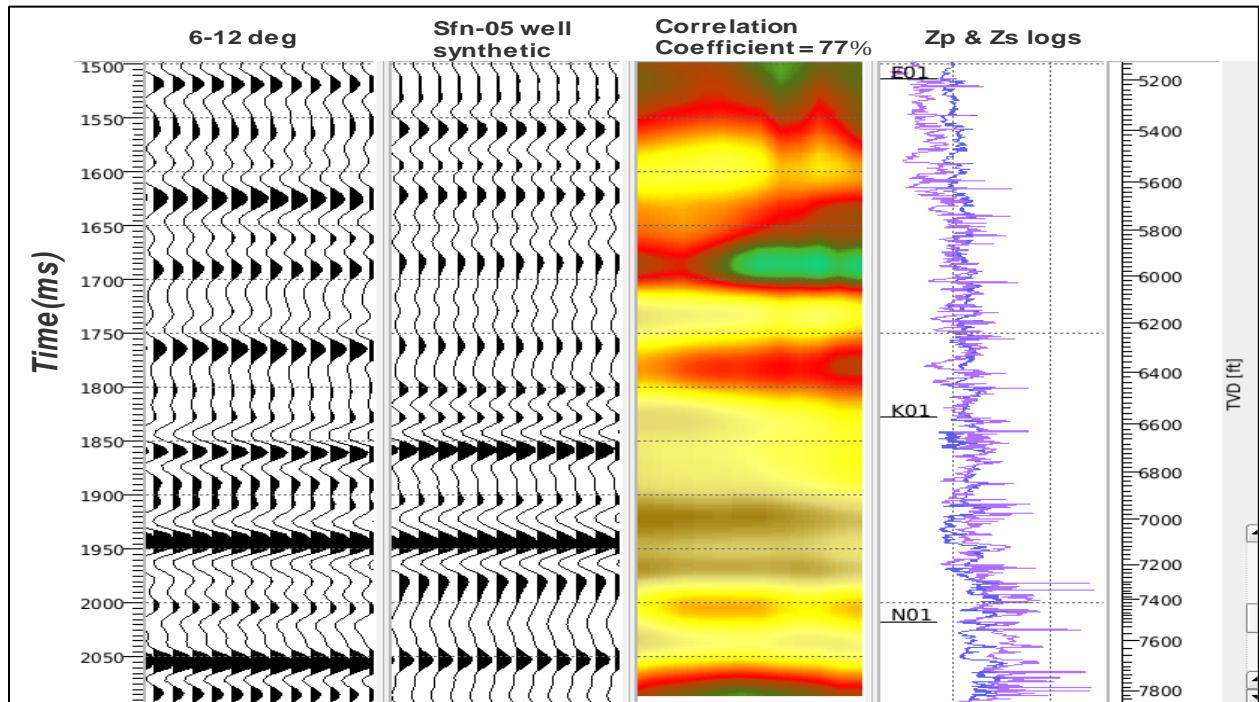
Figure 20c: Seismic to well tie using the near (6°-12°) stack and Sfn-05.

3.2.3 Wavelet Extraction
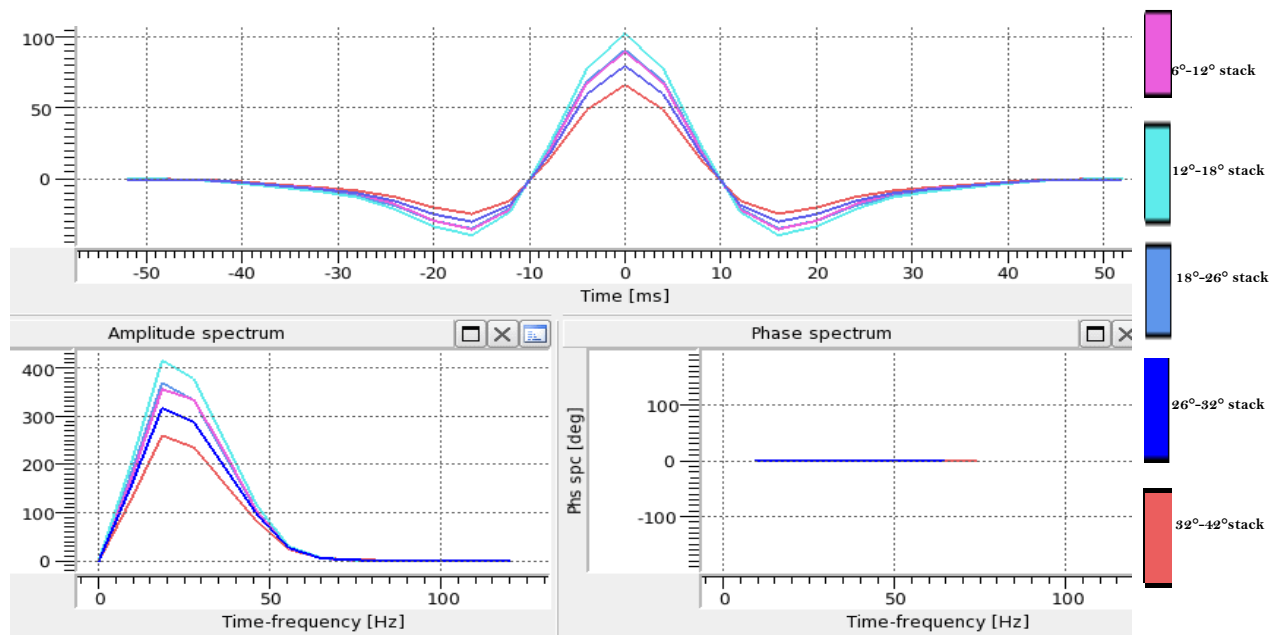
Figure 21a: Wavelet amplitude spectrum.
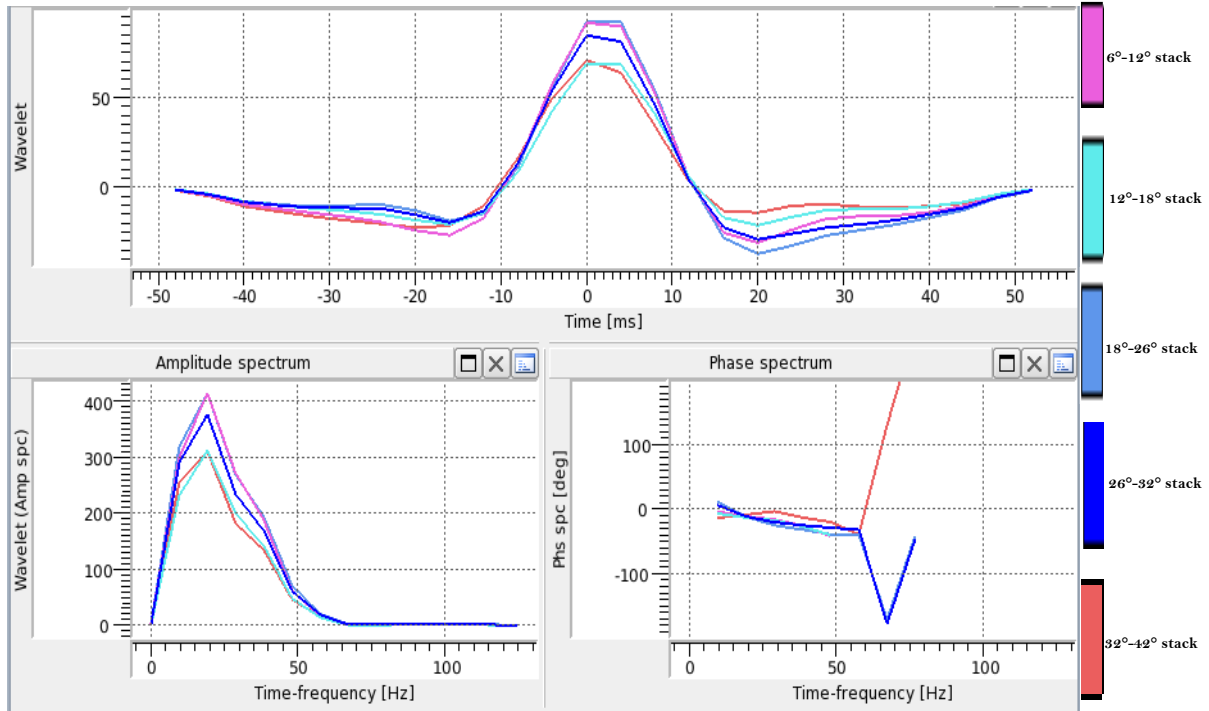
Figure 21b: Wavelet amplitude spectrum and phase.
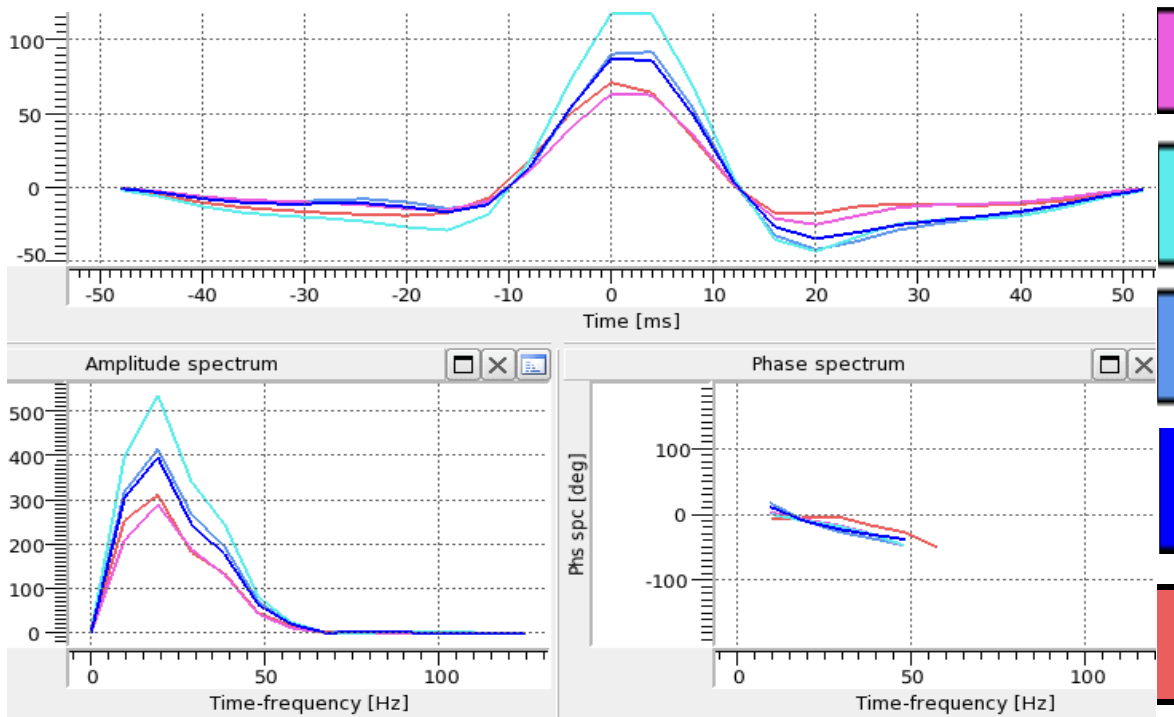
Figure 21c: Transform wavelets.

51

The wavelets QC are displayed in Figures 22 (a and b). Figure 22a is the wavelet autocorrelation QC in time along with the amplitudes and Phase spectrum. The upper panel show the wavelets displayed in time, smooth with small side lobes that taper quickly to zero while the bottom left panel show the amplitude spectrum, smooth with single peak without notches over the seismic bandwidth. The bottom right panel revealed the phase spectrum which are approximately flat through the seismic bandwidth. Figure 22b shows the comparison between wavelet spectrum (orange) and seismic spectrum (green). This reflects that good wavelet is extracted for the inversion. Figure 23 is the time-depth relationship used for seismic to well tie and wavelet extraction.
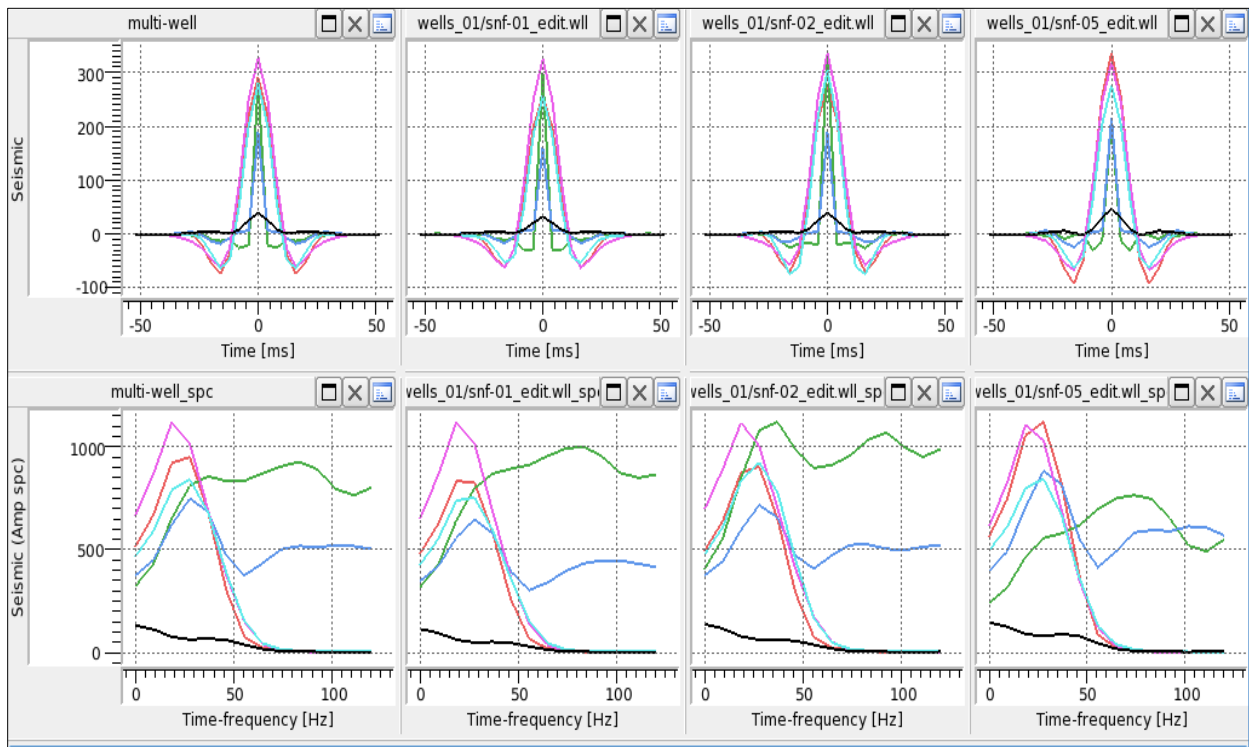
Figure 22a: Wavelet Autocorrelation QC.
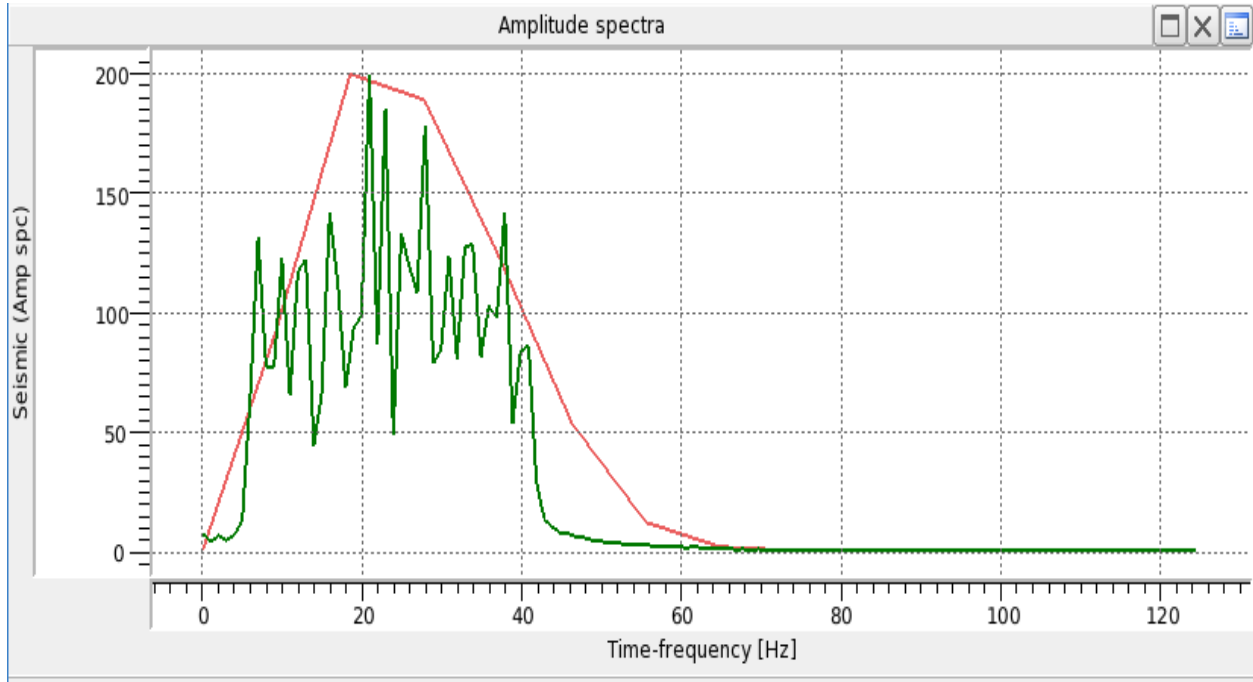
Figure 22b: Comparison between wavelet spectrum (orange) and seismic spectrum (green).
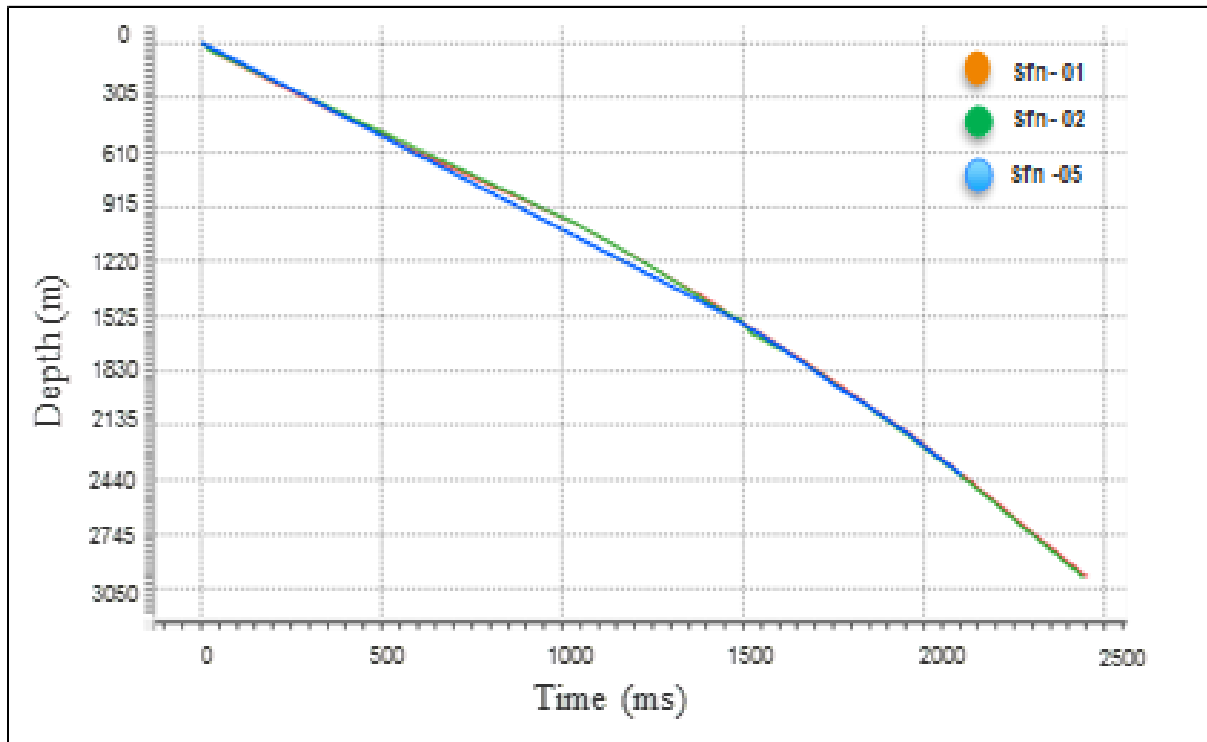
Figure 23: Time-depth curve for the three wells.

3.4 AVA SENSITIVITY ANALYSIS

3.4.1 Cross plot Analysis

Cross plot analysis of well data was first carried out to understand the relationships between various elastic and petrophysical properties. The sensitivity of each well property to lithology and fluid type variation was carried out by plotting P-impedance against S-impedance colored by Vshale, the plot of P-impedance and S-impedance was colored by water saturation while the plot of mu-rho and lambda-rho was colored by Vshale. The cross plot of Porosity with Density colored by Vshale, plot of Porosity with Density colored by water saturation, plot of Poisson's ratio and P-impedance colored by Vshale and the plot of lambda-rho and P-impedance colored by water saturation further revealed relationships between various elastic properties.

3.4.2 Fluid Substitution Analysis

Fluid substitution analysis was carried out to predict the sensitivity of rock properties to pore-fill types. The rock frame was initially 100% saturated with brine and later substituted with 80% oil then 80% gas. The cutoffs used for Paysand were $V_{Shale} \leq 0.3$, porosity 12% and $S_w \leq 0.65$ while the cutoffs for wet sand were $V_{Shale} \leq 0.3$, porosity 12% and $S_w \geq 0.8$. For each fluid type (water, oil and gas) V_P, V_S and ρ were generated and used to build the fluid-substituted models. This was accomplished using Biot − Gassmann theory (Gassmann, 1951 and Biot, 1956). The plot of the amplitude reflection coefficient with incidence angle was classified according to Rutherford and Williams (1989) while the AVA intercept versus gradient plot was classified according to Castagna and Swan (1997).

3.5 BUILDING LOW FREQUENCY MODELS

Seismic data is band-limited with inconsistent low frequency content. It is therefore necessary to introduce low frequency component from a different source (well data) into the seismic data prior to inversion to generate high quality inverted volumes. A geologic model known as the earth model was created and displayed as shown in Figure 24. The earth model was built based on the interval of interest and interpreted horizons based on their relationships to the top and base of the target reservoir. The P-impedance, S-impedance and density derived from well data were interpolated within the macro layers. The models generated showed high frequency as shown in Figure 25 (a - c) which could introduce errors into the inversion if used directly. As a result, high cut filter was applied to remove the high frequency content. The low frequency models created are displayed in Figure 26 (a - c).
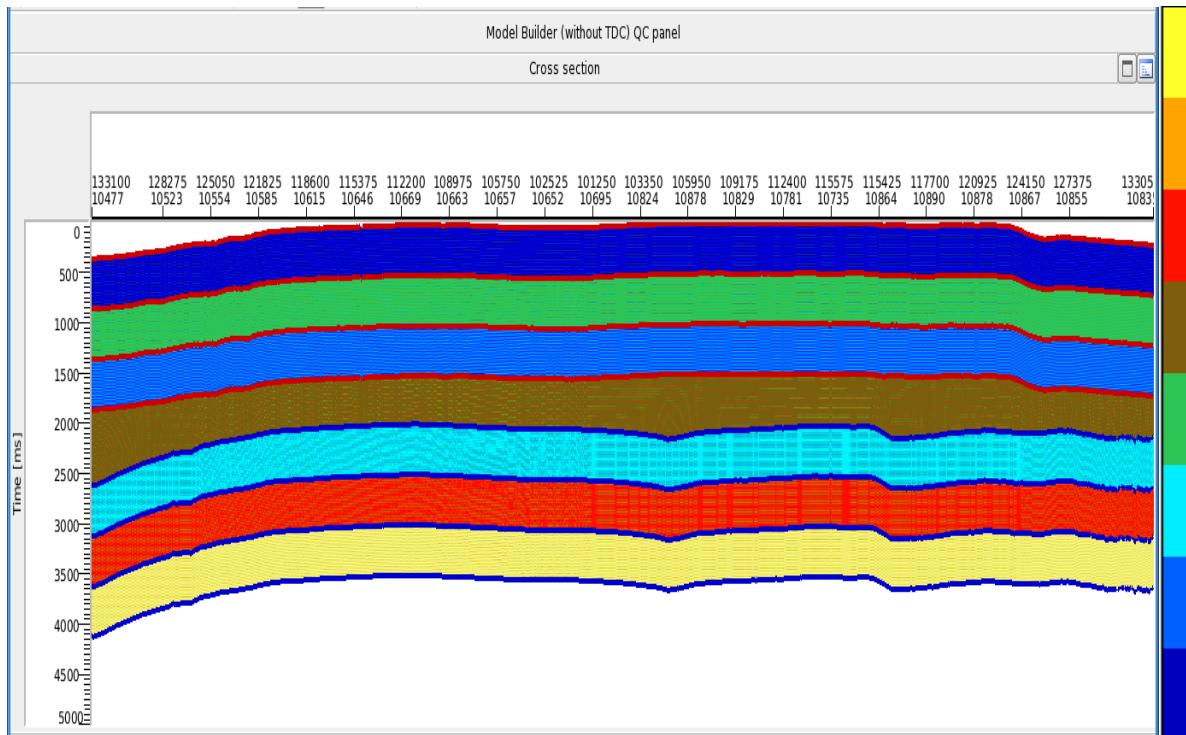
Figure 24: Earth model
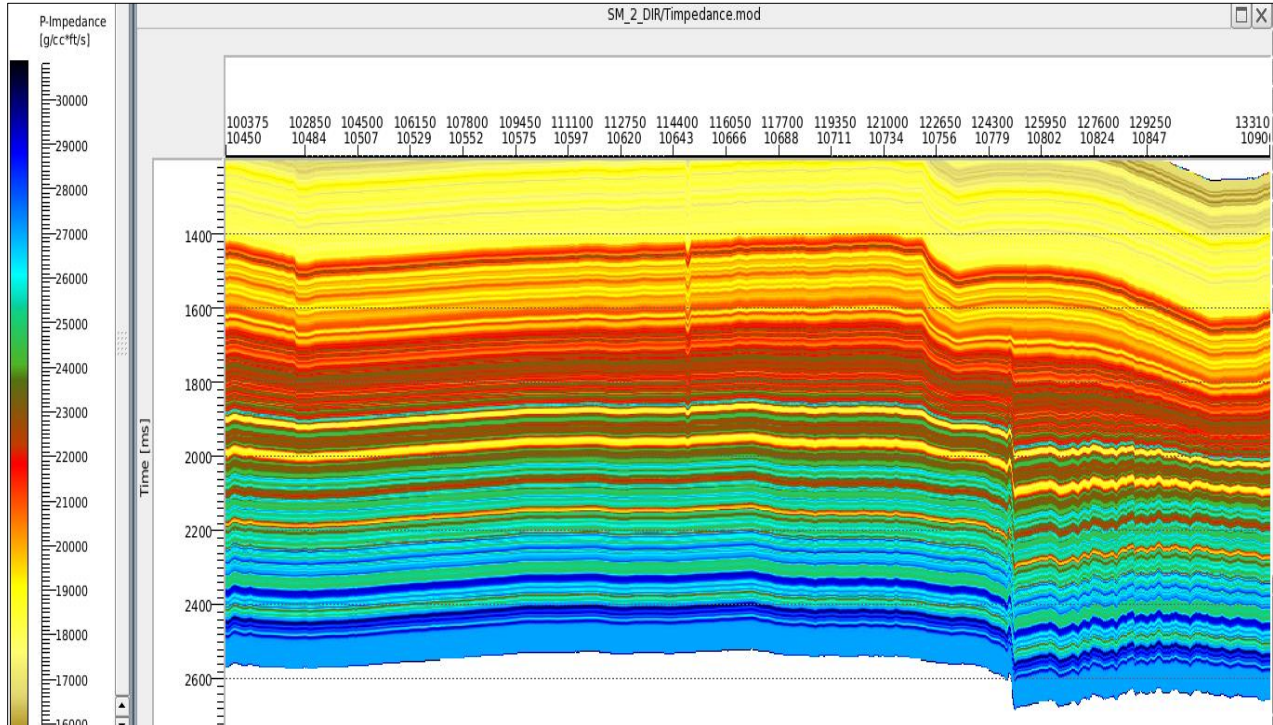
Figure 25a: P-impedance with high frequency content.
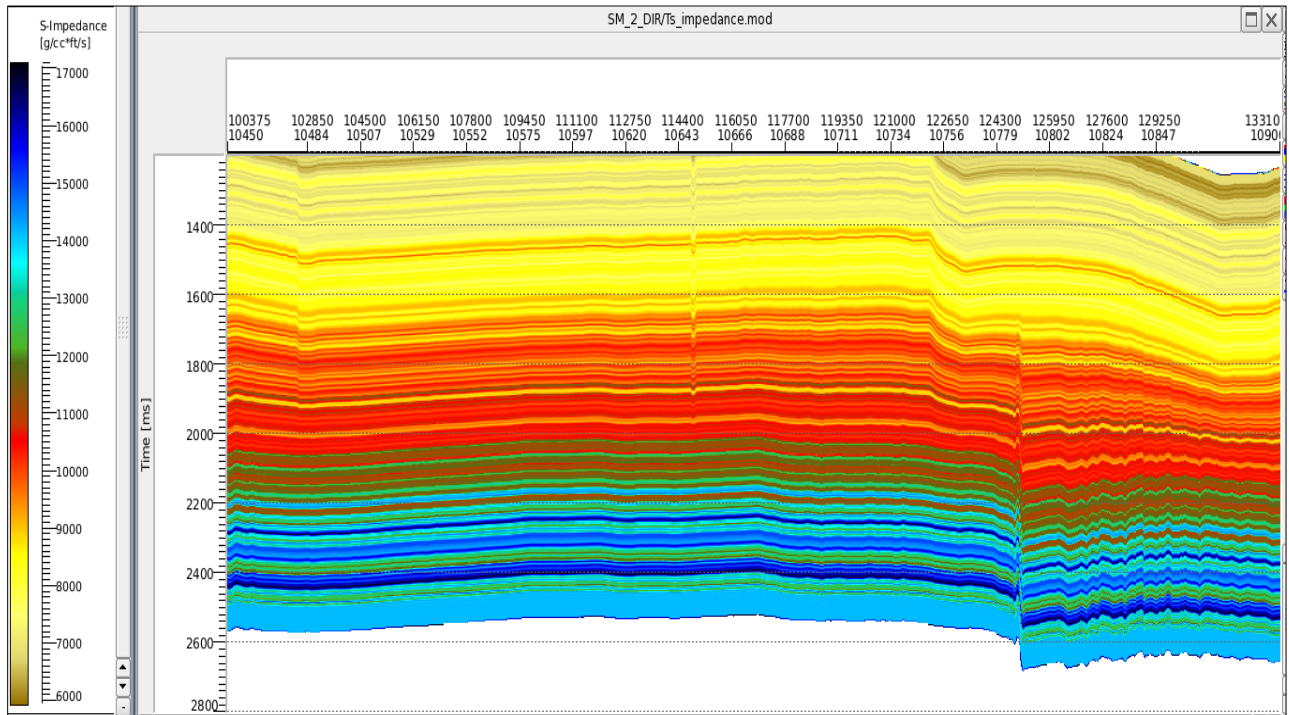
Figure 25b: S-impedance with high frequency content.
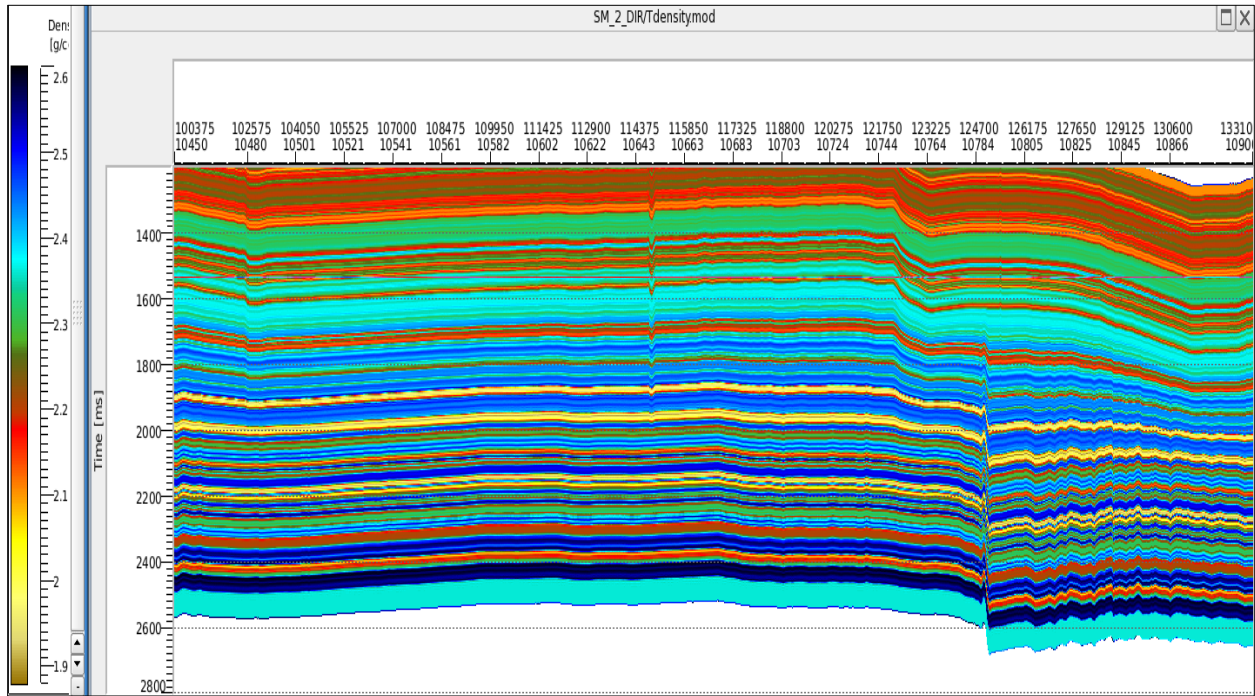
Figure 25c: Density with high frequency content.
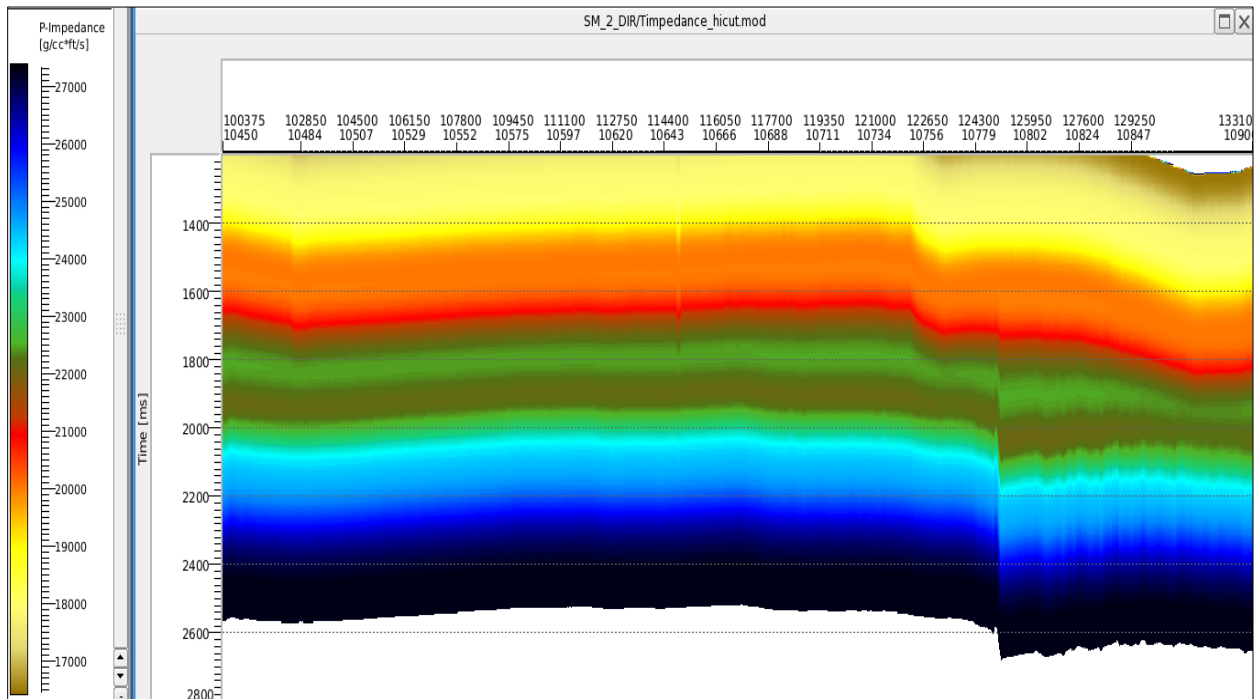
Figure 26a: P-impedance with low frequency content.
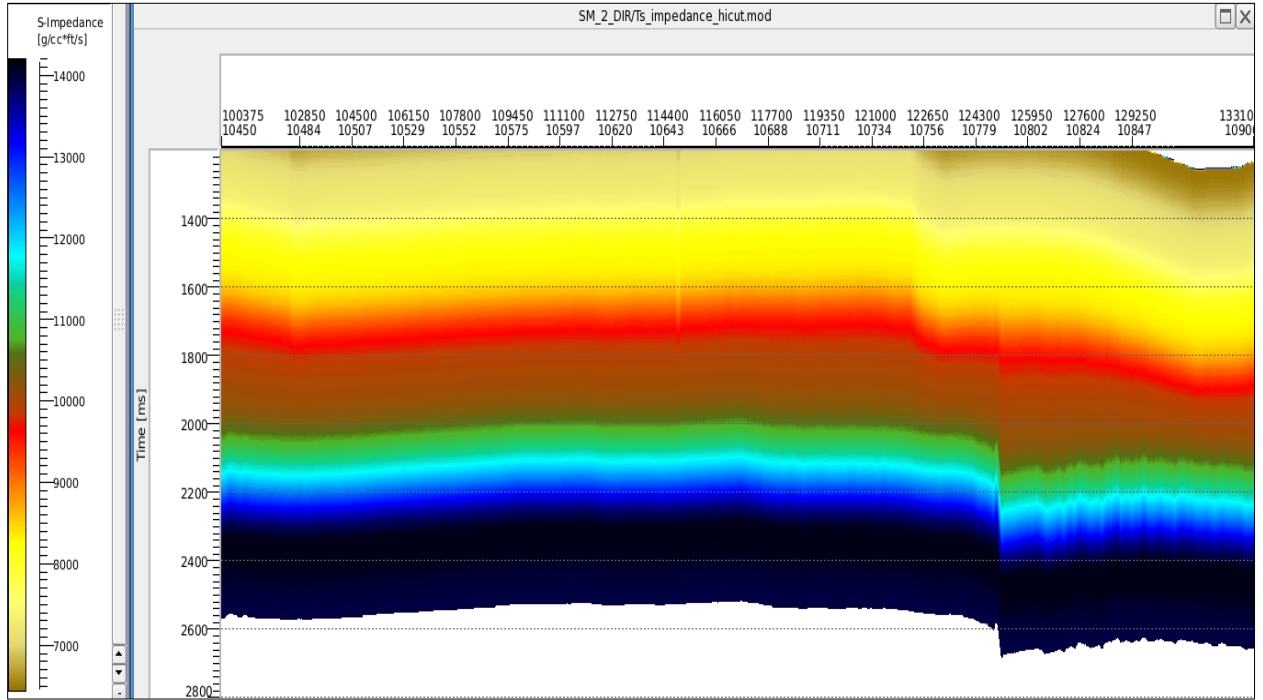
Figure 26b: S-impedance with low frequency content.
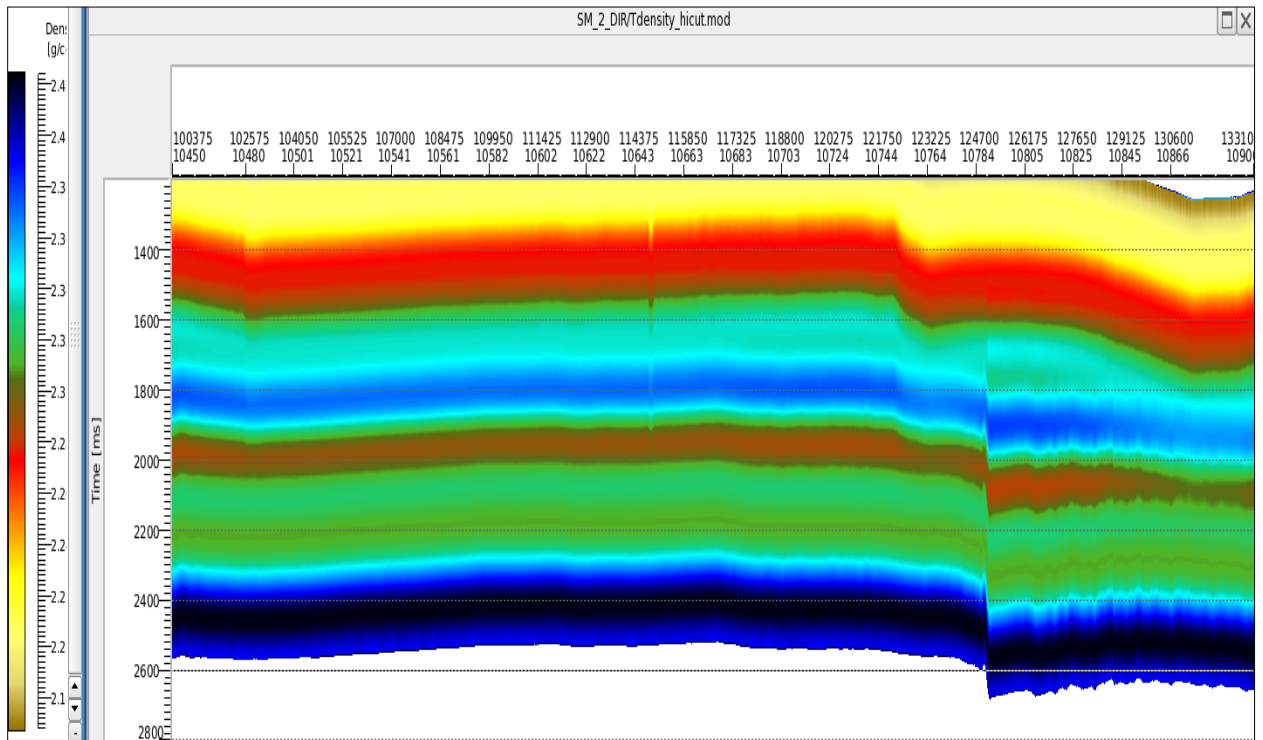
Figure 26c: Density with low frequency content.

3.5.1 Low Frequency Model QC

The P-impedance, S-impedance and density from the low frequency models were extracted at each well location to check their trends with the well P-impedance, S-impedance and density as shown in Figures 27 (a-c). In order to ensure that the background model have similar frequency content with the well data high cut filter was applied.

3.5.2 Low Frequency Trend (Compaction effect)
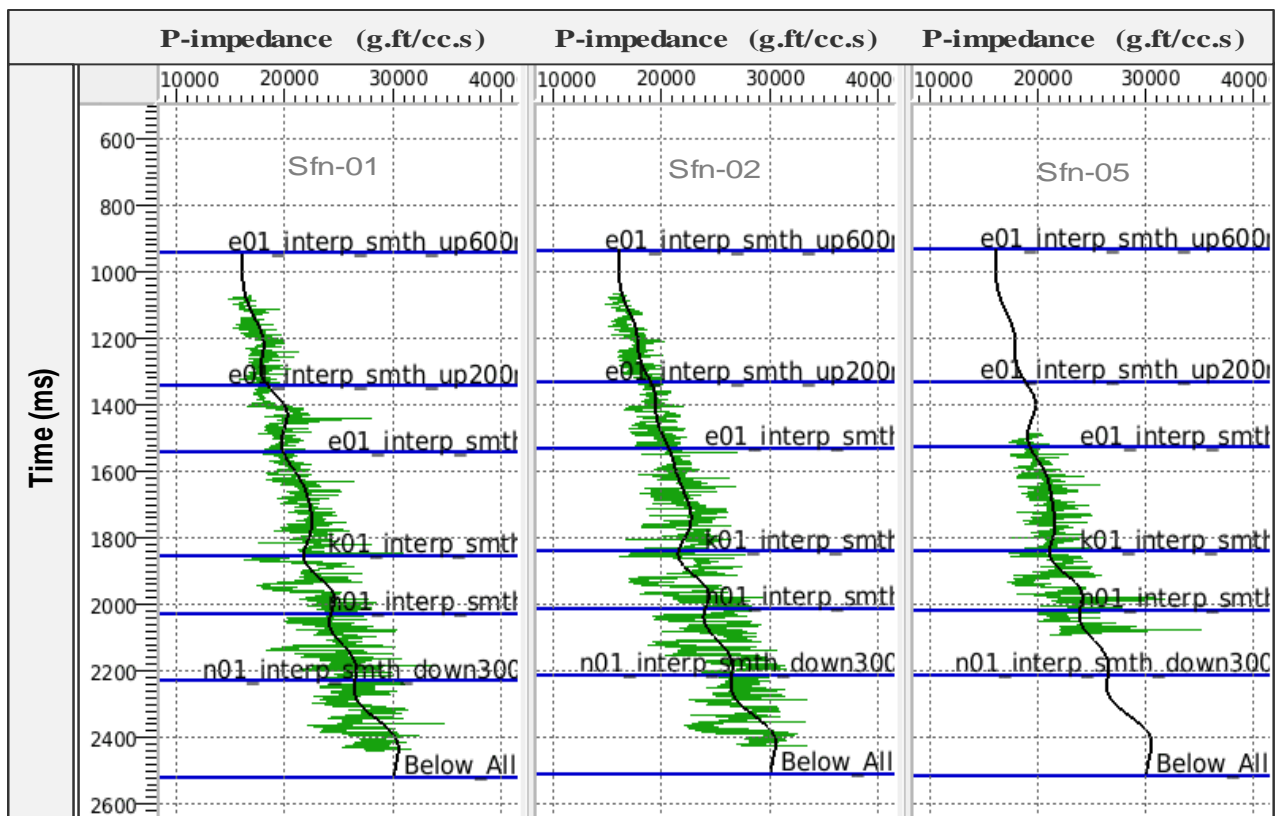
Figure 27a: P-impedance at the well (olive green) overlain by high-cut filtered interpolated P-impedance (black).
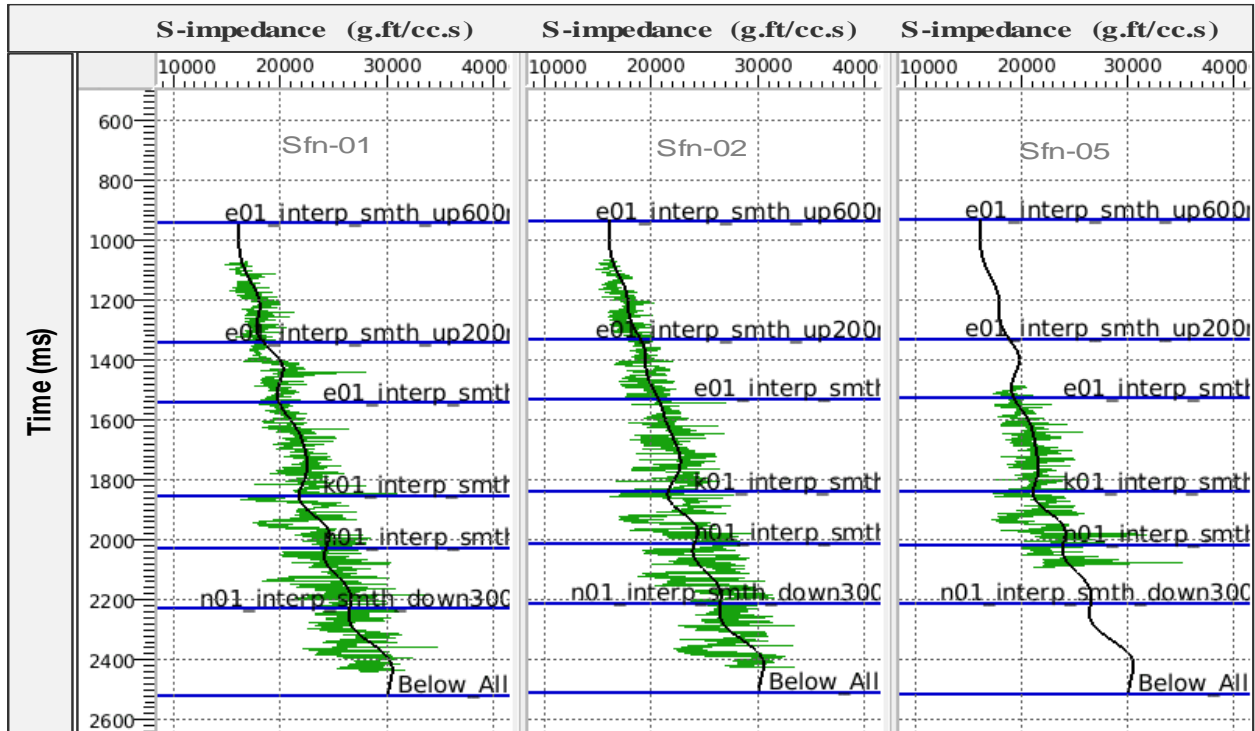
Figure 27b: S-impedance at the well (olive green) overlain by high-cut filtered interpolated S-impedance (black).
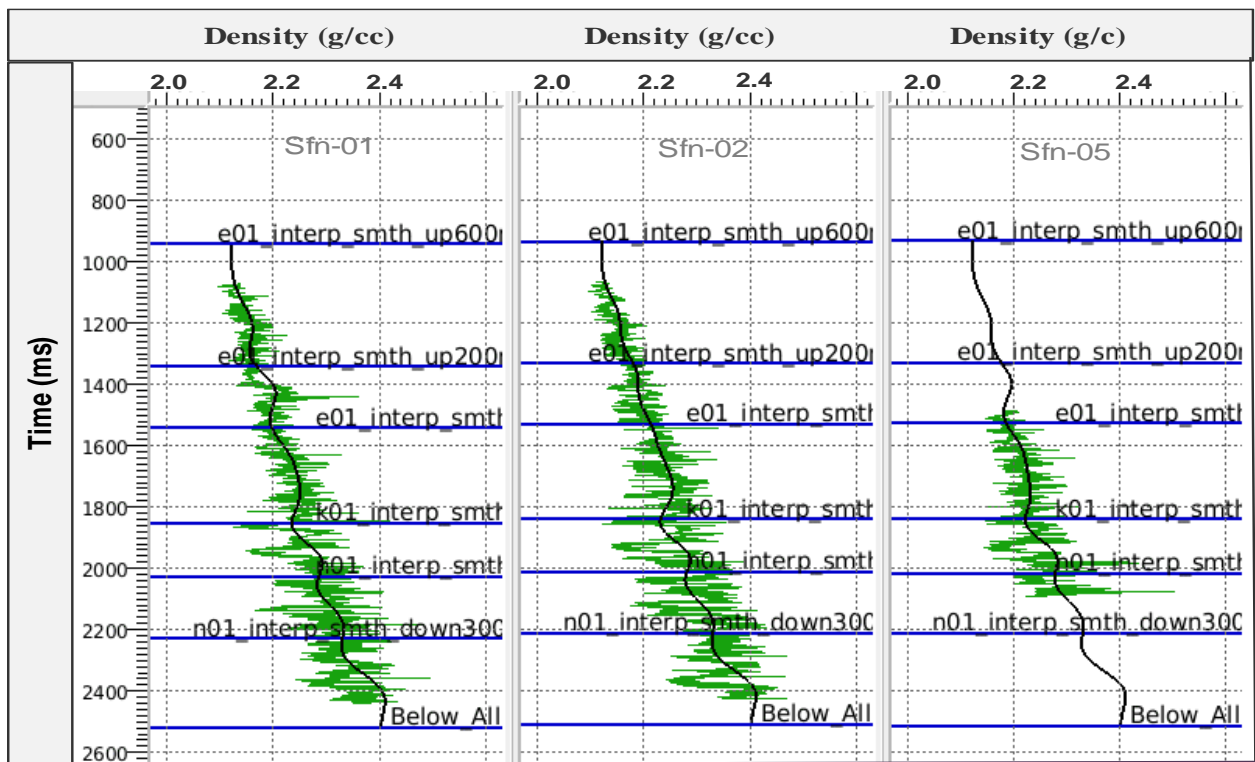
Figure 27c: Density at the well (olive green) overlain by high-cut filtered interpolated density (black).

A compaction trend was generated from P- impedance, S- impedance and density based on their interpolation from the Sonic logs guided by the interpreted seismic horizons for the entire volume. Since, shales usually have background effect in most reservoirs therefore the deviation from the trend would be indicative of anomalous signature (most likely sands).

Figures 28 (a-c) are the compaction trends for P-impedance (black), S-impedance (black) and density (black). The lines were matched from well to well and the values generated are constant at the horizon picked. The low frequency model is built based on the wells and does not introduce information absent in the seismic data.
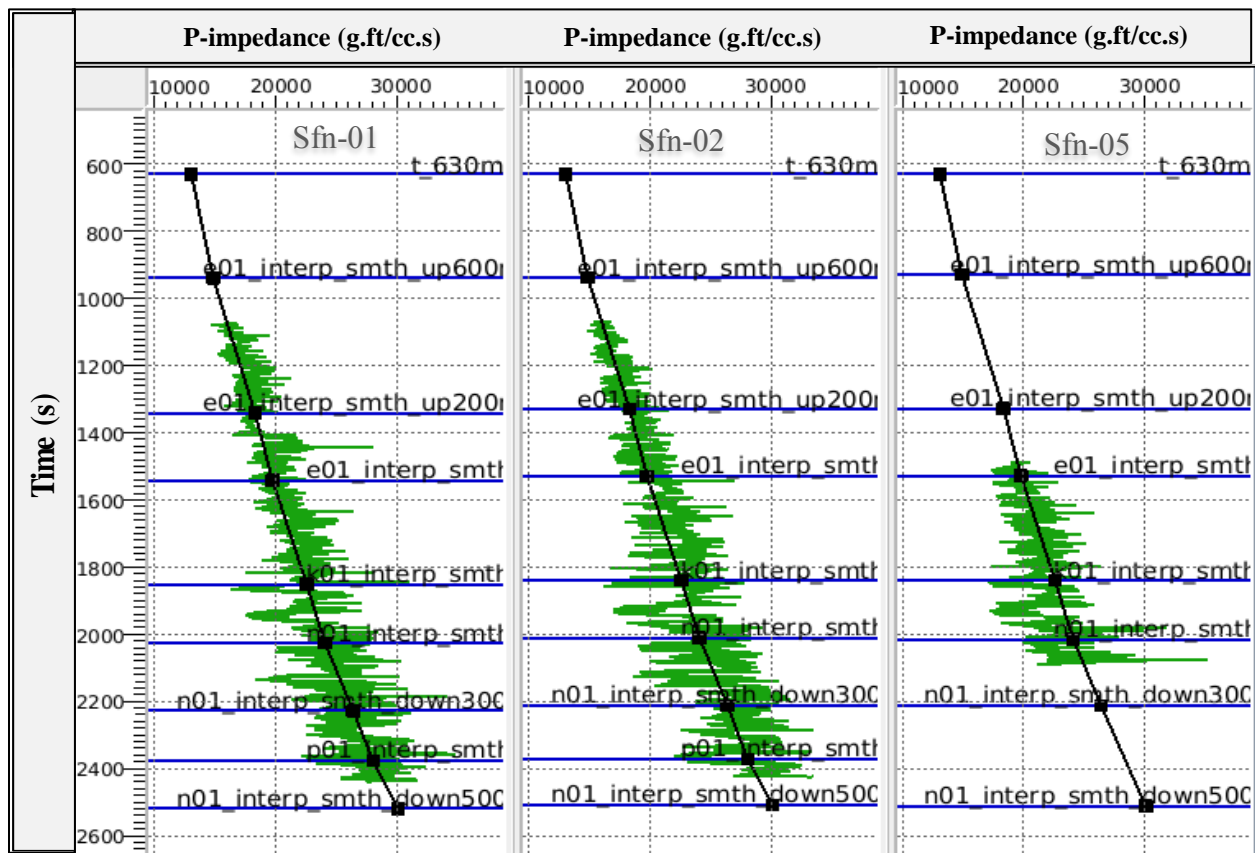
Figure 28a: P-impedance compaction trend.
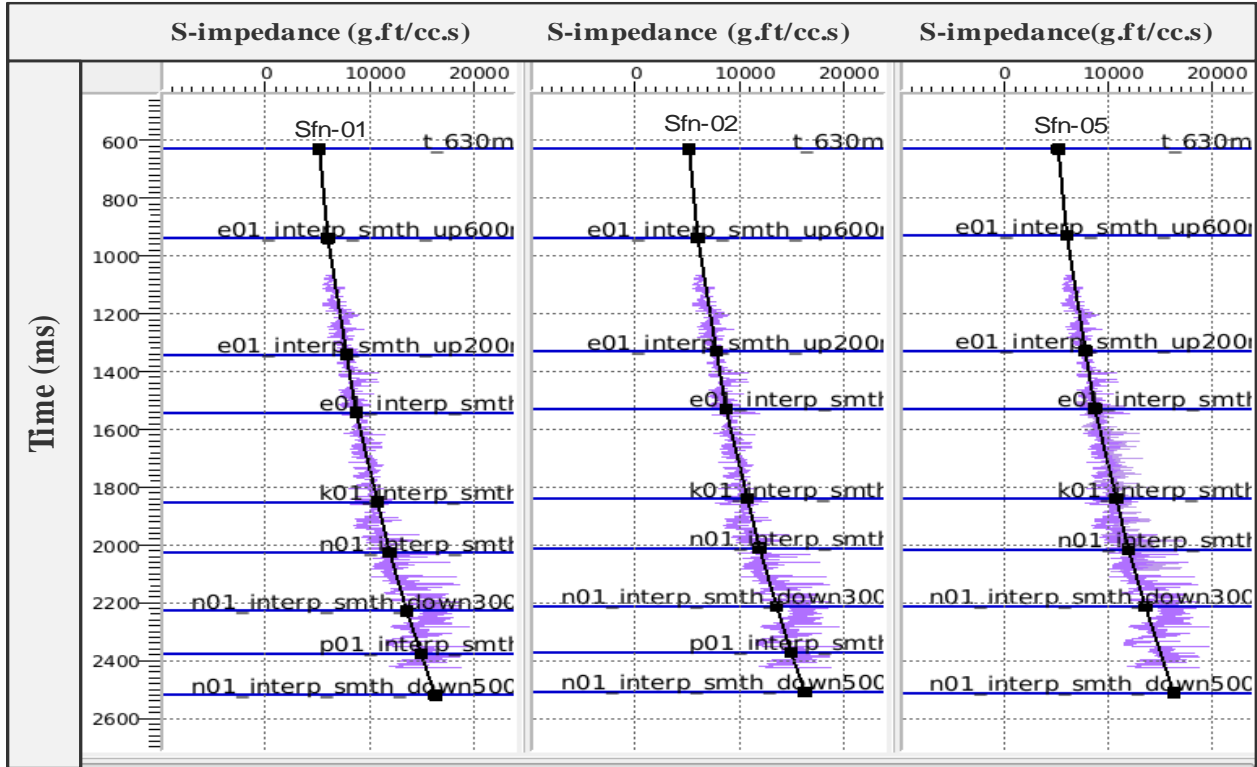
Figure 28b: S-impedance compaction trend.
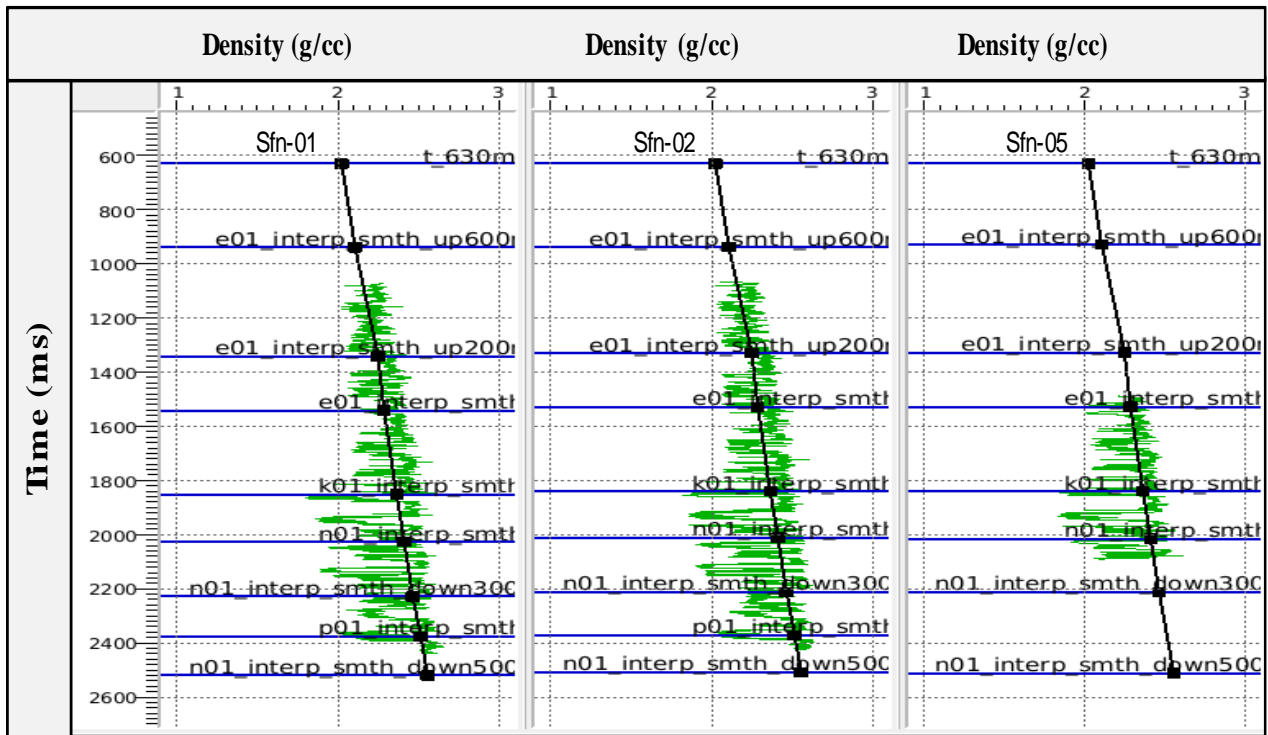
Figure 28c: Density compaction trend.

Table 3: P-impedance, S-impedance and Density values at the various horizons

S/N	Horizon	P-impedance (g.ft/cc.s)	S-impedance (g.ft/cc.s)	Density (g/cc)
1.	p01_interp_smth	28055	15000	2.5
2.	n01_interp_smth	24111	12502	2.3
3.	k01_interp_smth	22598	10500	2.3
4.	e01_interp_smth	19800	81108	2.3
5.	n01_interp_smth_down300 ms	26418	13042	2.4
6.	e01_interp_smth_up200 ms	18350	7350	2.3
7.	t_630 ms	13116	5104	2.0
8.	n01_interp_smth_down500 ms	30102	16502	2.5
9.	e01_interp_smth_up600 ms	14908	6308	2.1

3.6 TESTING OF INVERSION PARAMETERS

Optimal inversion parameters were selected prior to inversion so as to ensure quality inversion results. This was achieved by performing inversion on selected well locations and testing range of inversion parameters to check the quality of inversion products as shown in Figure 29. The inversion parameters tested for are Seismic misfit signal to noise ratio, Contrast misfit uncertainty, Wavelet scale factor, Merge cut off frequency. The soft trend constraints, Soft spatial constraint, AVO/AVA modeling method and the hard trend constraint.

Sequence for testing the inversion parameters is presented as follows:

- Seismic misfit signal to noise ratio

- Contrast misfit uncertainty

- Wavelet scale factor

- Merge cut off frequency

- The soft trend constraints

- Soft spatial constraint

- AVO/AVA modeling method

- The hard trend constraint

Seismic misfit signal to noise ratio: This was carried out to ensure seismic to synthetic match. It was set to optimum value of 15dB which gave quality inversion results prior to the final inversion.

Contrast misfit uncertainty: This was done to ensure variability of the elastic parameters around the low frequency trend. The contrast misfit uncertainty value was decreased to 0.01 to obtain tighter constraint for the inversion.

Wavelet scale factor: An optimum scaling factor of 1 was used to enhance the seismic to synthetic match.

Merge cut off frequency: This was used to constrain the inversion algorithm. It stabilized the inconsistent low frequencies in seismic data by merging low frequency content derived from well data prior to inversion. The low frequency content was obtained from the high cut filtered volumes created from the interpolation of well data. Setting the merge frequency too high can cause the model to generate inversion results within the seismic bandwidth. Setting it too low can allow noise to cause striping in the inversion results. The combination of low frequency with high frequency from the seismic data was used to generate absolute acoustic and elastic reservoir properties. The merge cut off filter frequency used is shown in Figure 30.

The soft spatial constraint was toggled off, AVO/AVA modeling method used was Aki-Richards and the hard trend constraint was also disabled off.
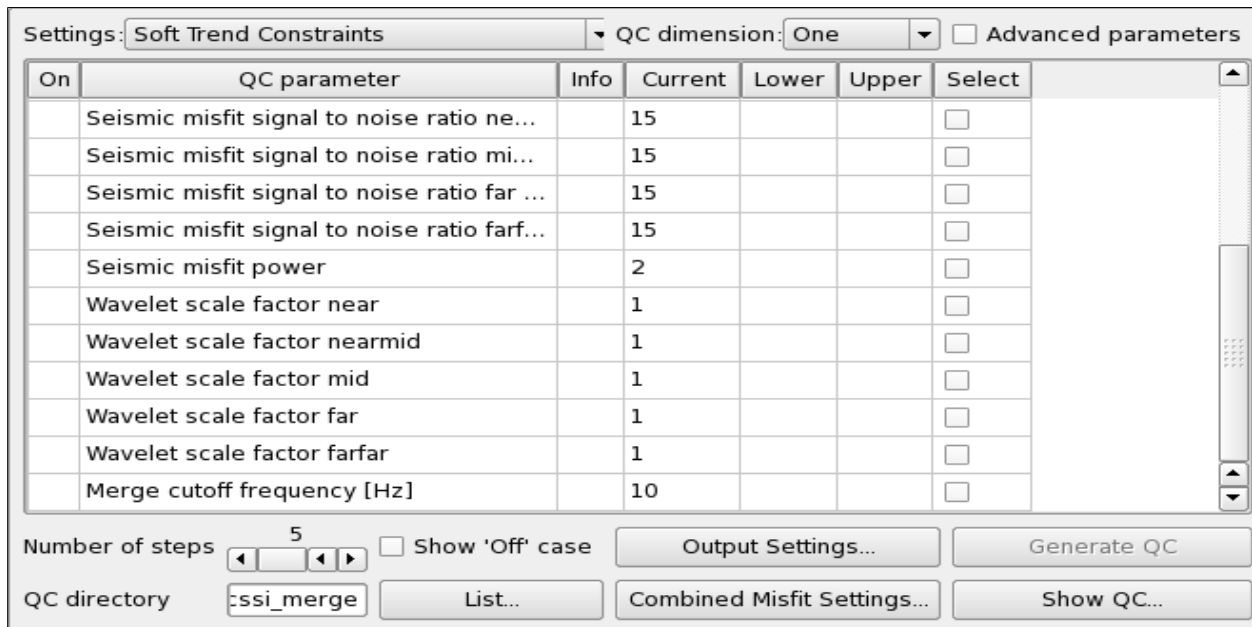
Figure 29: Optimum parameters used for the inversion.
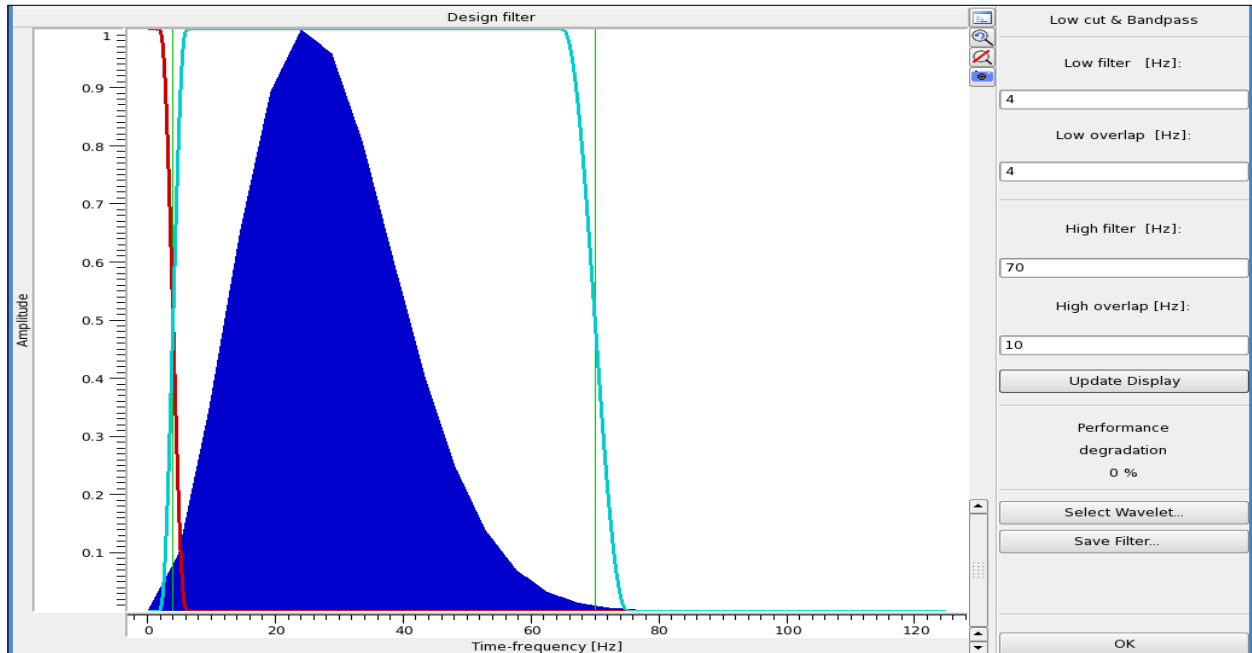
Figure 30: Merge filter with the required cut off filter frequency.

3.7 SIMULTANEOUS INVERSION

Simultaneous inversion is a sophisticated process of inverting the seismic data into elastic properties descriptive of target reservoirs (Berge, 2002 and Jason, 2013). This was carried out to simultaneously invert five angle stacks to generate elastic volumes for quantitative interpretation that will enhance hydrocarbon discovery in 'Sandfish' Field. The key inputs to the inversion are the low frequency models generated from high cut filtered interpolated P-sonic, S-sonic and density logs with seismic data (6°- 12°, 12°- 18°, 18°- 26°, 26°- 32° and 32°- 42°), seismic horizons and extracted wavelets. Jason's sparse spike inversion software was used to iterate trial inversions until the model sufficiently matched the seismic data. Figure 31 is the work flow for simultaneous inversion.
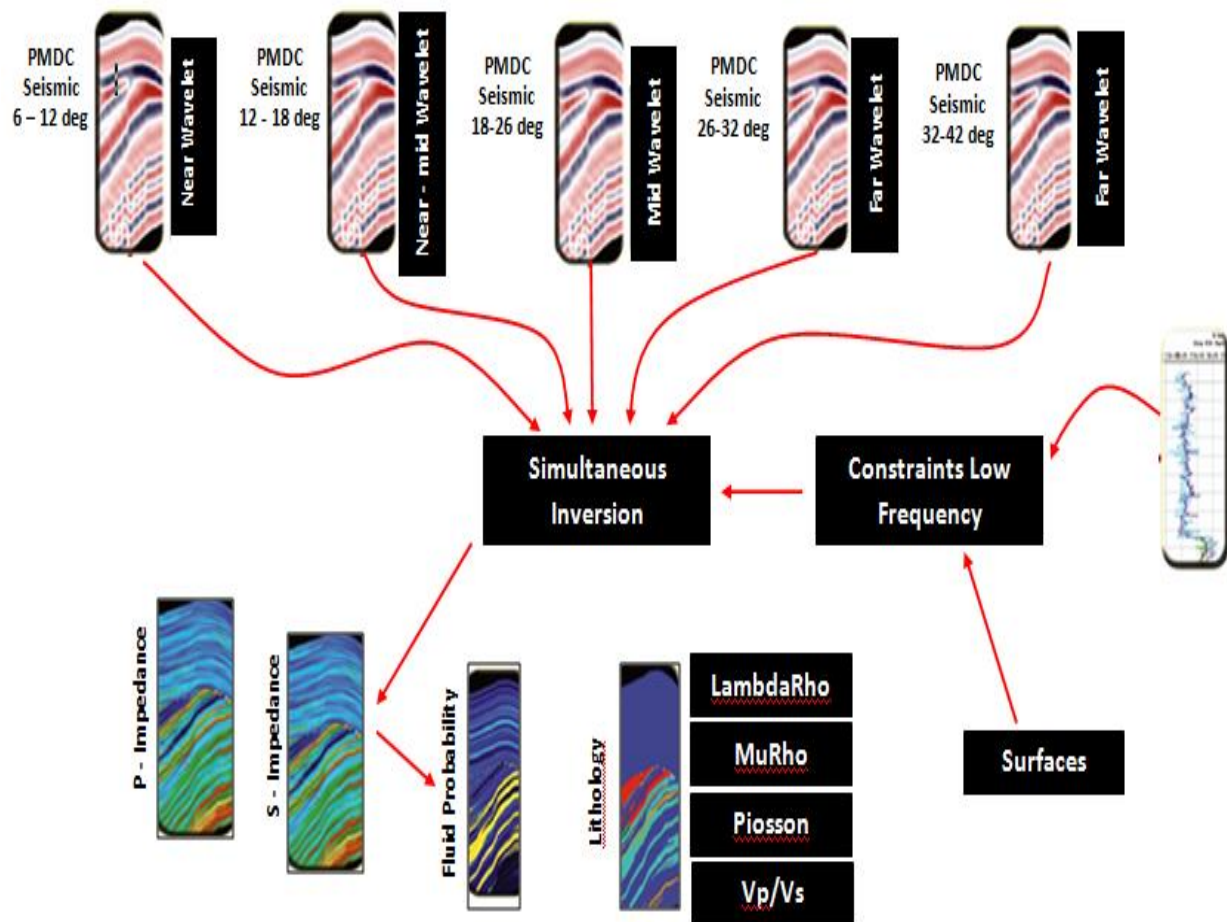
Figure 31: The Workflow for Simultaneous Inversion (Modified from Jason, 2013).

3.8 ELASTIC INVERSION

Elastic inversion is the variation of impedance with angle of incidence (Veeken and Da Silva, 2004). Near and far-far angle stacks were inverted to compliment the simultaneous inversion products. The key inputs are low frequency model, near stack (6°- 12°) and far-far Stack (32°- 42), seismic horizons and extracted wavelet. Jason's sparse spike inversion software was also used to iterate trial inversions until the model sufficiently matched the seismic data Figure 32 is the work flow for elastic impedance inversion.
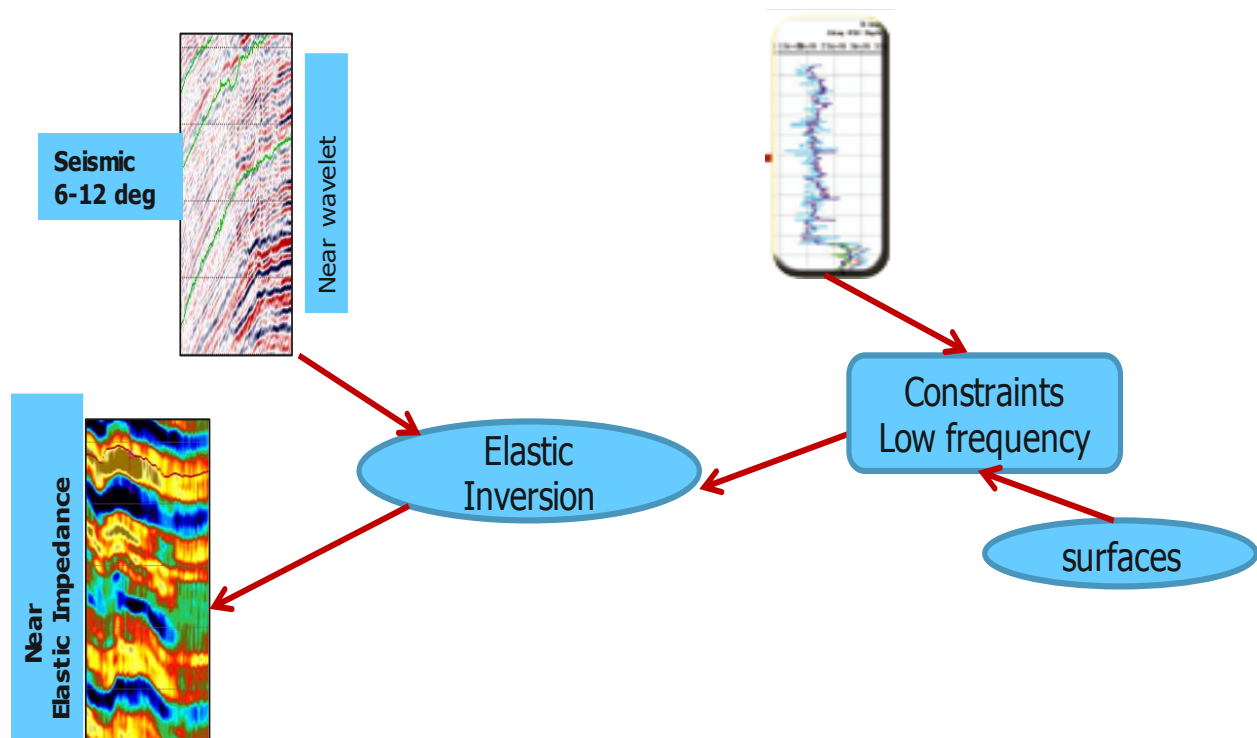
Figure 32: The Workflow for Elastic Impedance Inversion (Modified from Jason, 2013)

3.9 CORRELATION OF INVERTED VOLUMES

The elastic impedance for near and far-far angle stacks were inverted and correlated with the simultaneous inversion volumes to observe the trend of events so as to enhance quantitative interpretation and reduce uncertainty of the subsurface reservoirs in 'Sandfish' Field located in the Niger Delta.

3.10   COMPARISON OF SEISMIC DATA WITH INVERTED VOLUMES

Initial Seismic data was compared with inverted volume (Lambda-rho). This was carried out to assess the nature of AVA effects in 'Sandfish' Field. The subtle features identified on seismic data were converted to elastic layer property characterized by clastic Class III AVA sands (low

impedance sands). The fluid type was easily identified when compared with rock properties at the interval of interest. The knowledge of the fluid and lithology types could reduce exploration risk (mis-interpretation) in 'Sandfish' Field.

3.11 GENERATION OF LITHOLOGY AND FLUID PREDICTION MAPS

The outputs from simultaneous inversion are the full-bandwidth and band-limited P-impedance, S-impedance and density volumes, which were used to derive Poisson's ratio, lambda-rho, Vsand and mu-rho volumes. These seismic attributes are determined using formulae from Bacon *et al.* (2003) and Contreras *et al.* (2006) as in equations (21-27). Quantitative predictions of reservoir properties are made from extracted inversion product derivatives at the N-01 reservoir.

Compressional wave velocity, $V_P = \sqrt{\dfrac{K + {}^{4\mu}/_3}{\rho}}$ $\hspace{3cm}$ 21

Where, K = Bulk modulus, μ = Shear modulus, ρ = Density, ⋋ = Lambda

Shear wave velocity, $V_S = \sqrt{{}^{\mu}/_{\rho}}$ $\hspace{3cm}$ 22

P-impedance, $Z_P = \rho V_P$ $\hspace{3cm}$ 23

S-impedance, $Z_S = \rho V_S$ $\hspace{3cm}$ 24

Poisson's ratio, $\sigma = \dfrac{(\frac{V_P}{V_S})^2 - 2}{2(\frac{V_P}{V_S})^2 - 2}$ $\hspace{3cm}$ 25

Mu-rho, $Z_P^2 = (\rho V_P)^2 = \mu \rho$ $\hspace{3cm}$ 26

Lambda-rho, $Z_P^2 - 2Z_S^2 = \lambda \rho$ $\hspace{3cm}$ 27

CHAPER FOUR

4.0   RESULTS AND DISCUSSION

4.1 AVA SENSITIVITY ANALYSIS

4.1.1 Cross plots

The results of AVA sensitivity analysis are displayed in Figures (33 – 39). The plot of P-impedance (Z_P) against S-impedance (Z_S) colored by Vshale is displayed in Figure 33. The Figure reveals the litho-types in reservoirs of interest. The polygon captures the points with low shale volume (yellow) separated from the background trend that is highlighted in the well logs. The separation of the sands from the background shale is obvious but the difference is not large.
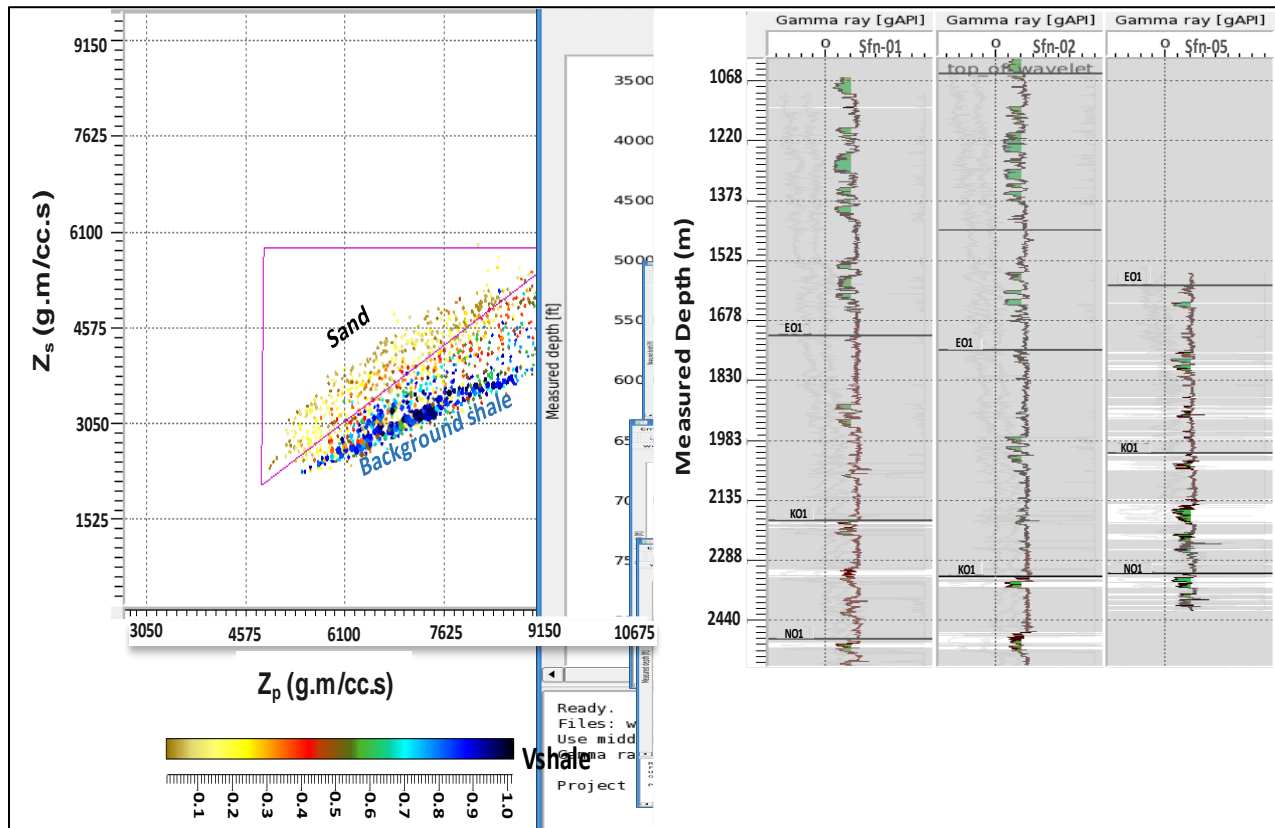
Figure 33: Cross-plot of Z_p and Z_s from well logs colored by Vshale.

The plot of P-impedance (Z_P) against S-impedance (Z_S) colored by water saturation in Figure 34 indicates fluid types at the reservoirs of interest. The polygon captures the points with low water saturation (yellow), separated from the background trend with high water saturation (blue) these are highlighted in the well logs.
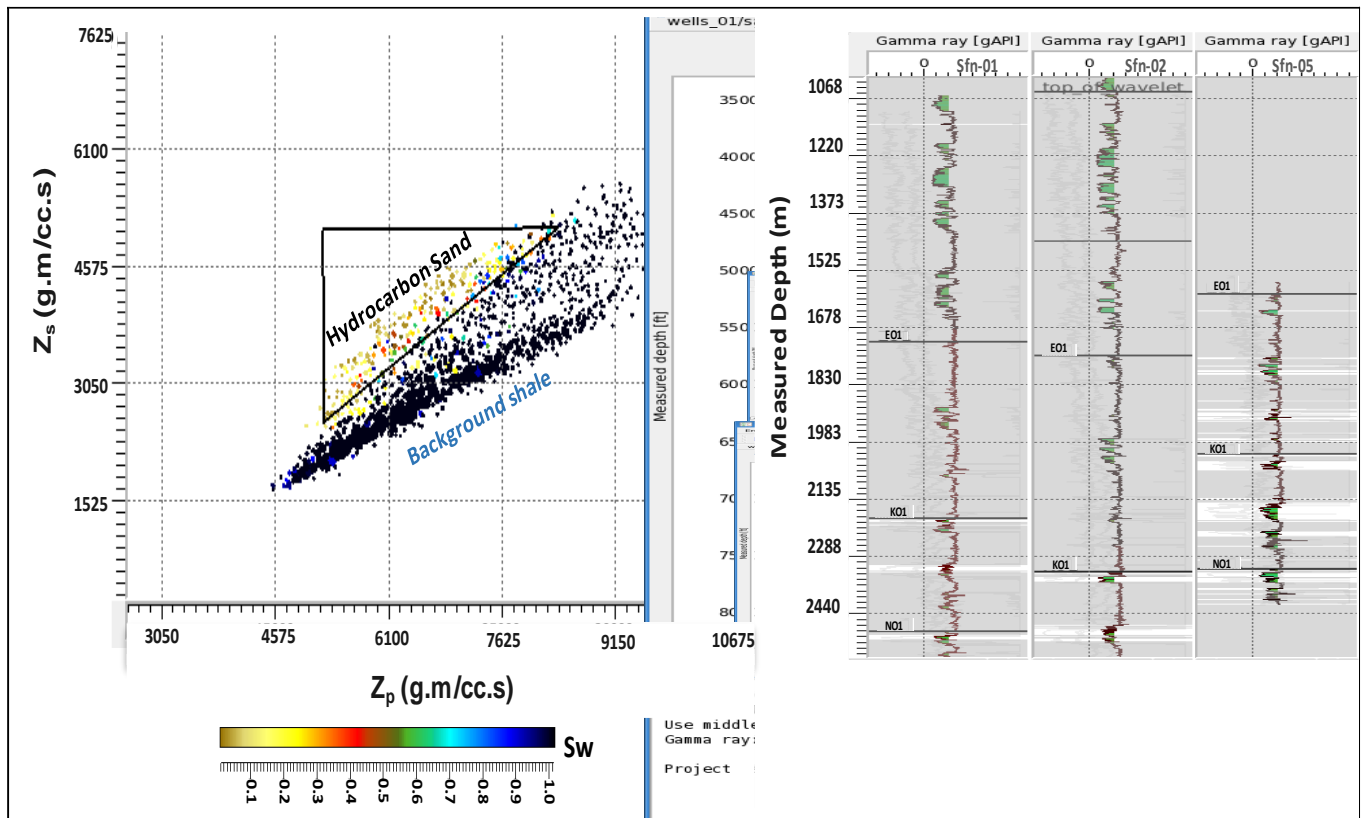
Figure 34: Cross plot of Z_p and Z_s from well logs colored by Sw.

The cross plot of mu-rho and lambda-rho is displayed in Figure 35. This is an important cross plot that differentiated low shale volume from background shale. It shows the separation of hydrocarbon sands (yellow) with low lambda-rho from shales (blue) with high lambda rho. This shows that lambda-rho versus mu-rho is a good litho-fluid discriminator in this field. This reveals that simultaneous inversion technique is an appropriate tool for the study investigation.

71
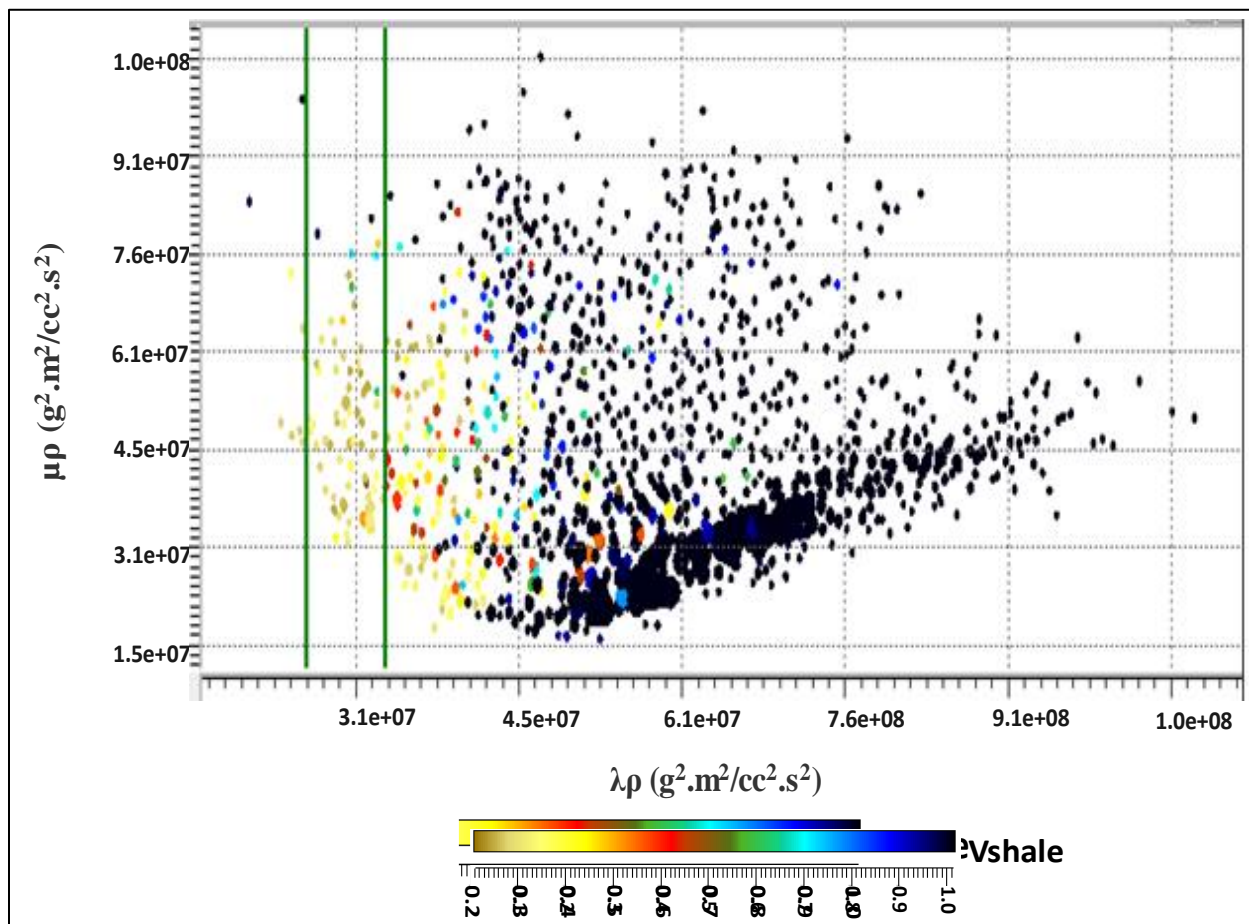
Figure 35: Cross plot of μρ and λρ from well logs colored by Vshale.

The cross plot of porosity with density colored by Vshale is displayed in Figure 36, It shows the separation of sands (yellow) with low density and porosity away from background shale (blue) with high density and porosity. This indicates that sands are more porous and less compacted compared to background shale. The plot of porosity with density colored by water saturation is displayed in Figure 37, the plot revealed the separation of hydrocarbon sands (yellow) away from water saturated shale (blue). The plot of Poisson's ratio and P-impedance colored by Vshale is shown in Figure 38. It shows the separation of sands (yellow) with low Poisson's ratio and P-

impedance from shale with high Poisson's ratio and P-impedance while the plot of lambda-rho and P-impedance colored by water saturation is displayed in Figure 39. The plot revealed the separation of hydrocarbon sands (yellow) from water saturated shale (blue).
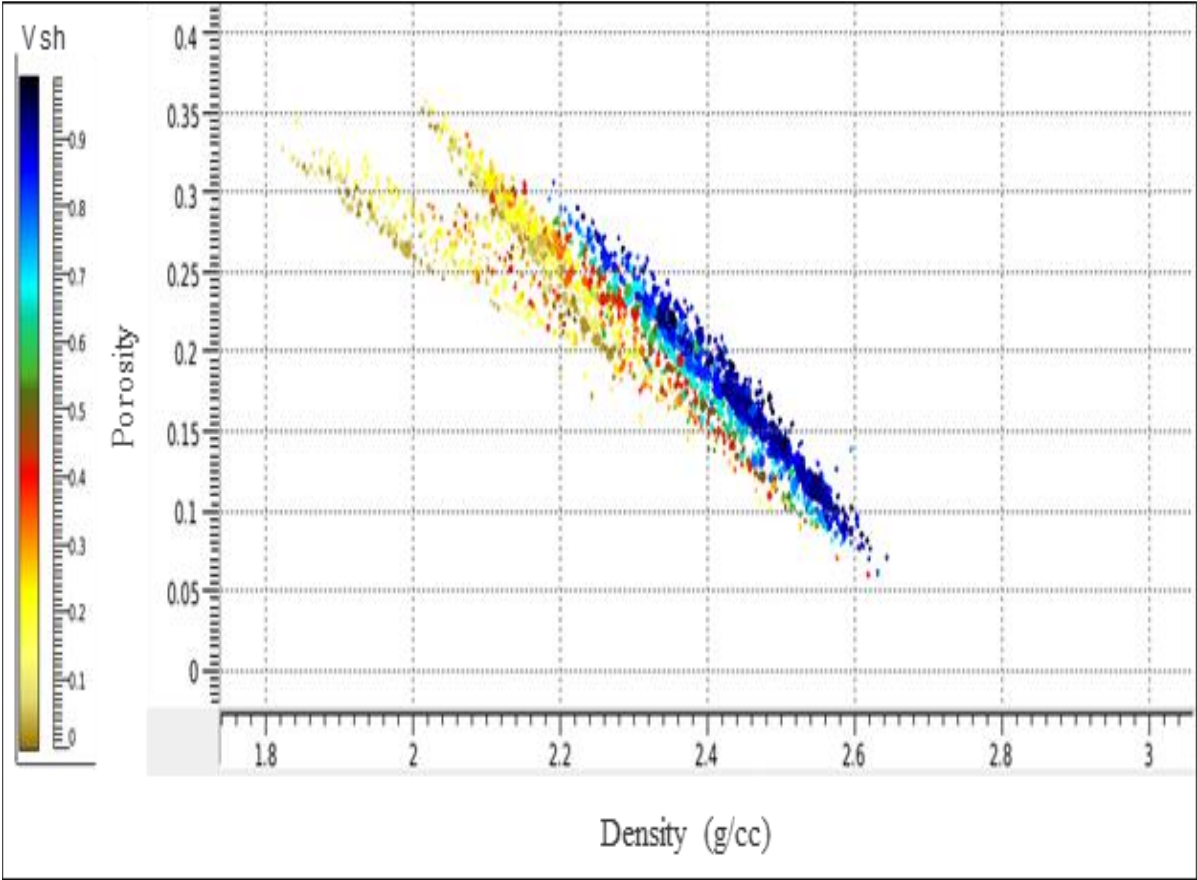
Figure 36: The cross plot of ϕ with ρ colored by Vshale.
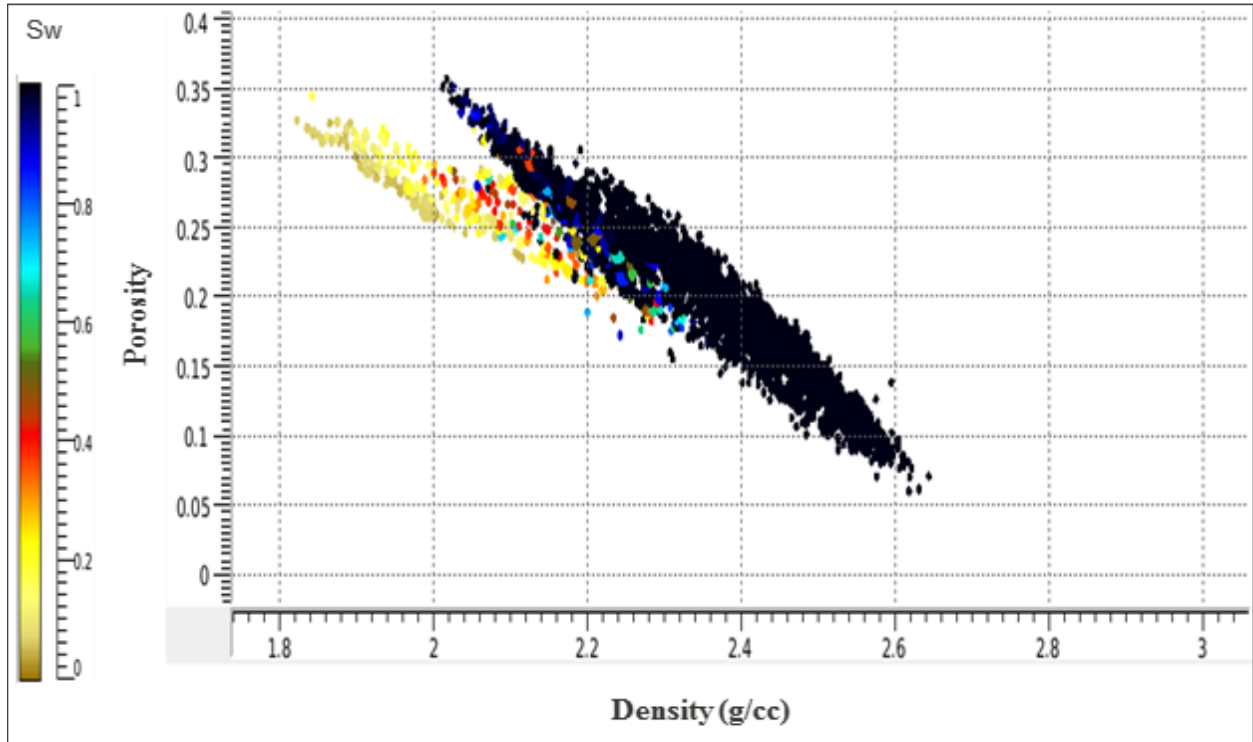
Figure 37: The cross plot of φ with ρ colored by Sw.
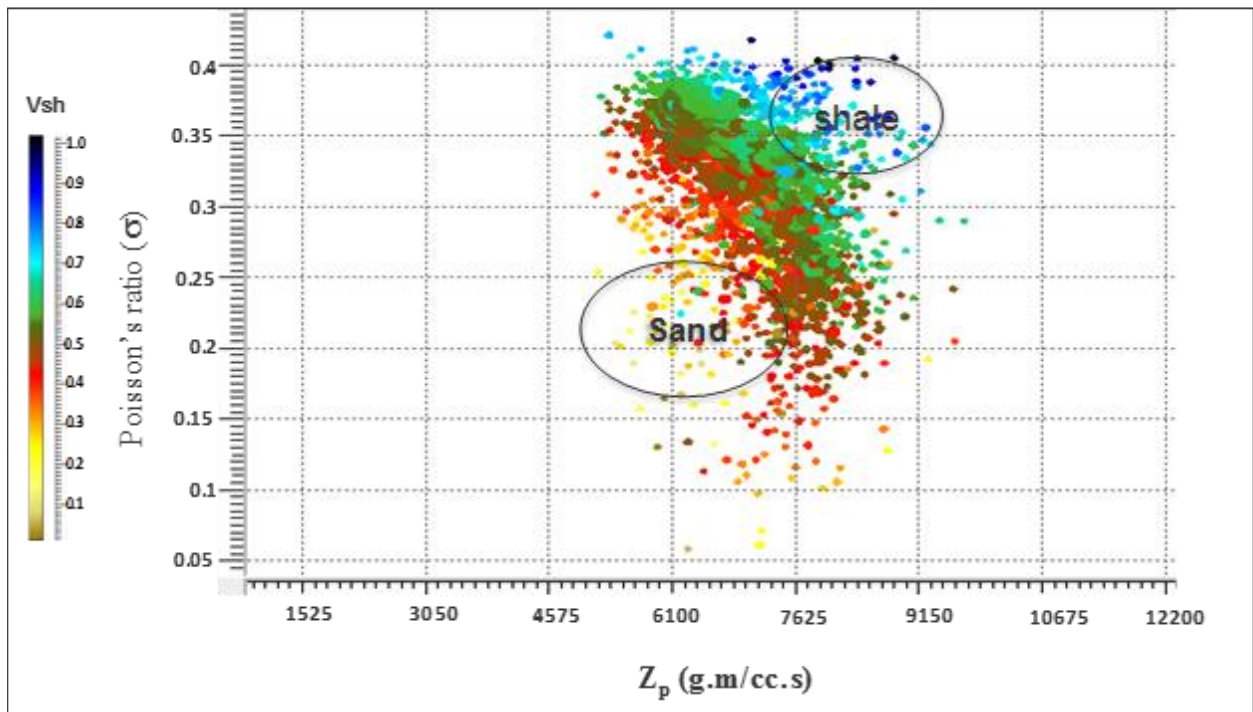
Figure 38: The plot of σ and Z_P colored by Vshale.
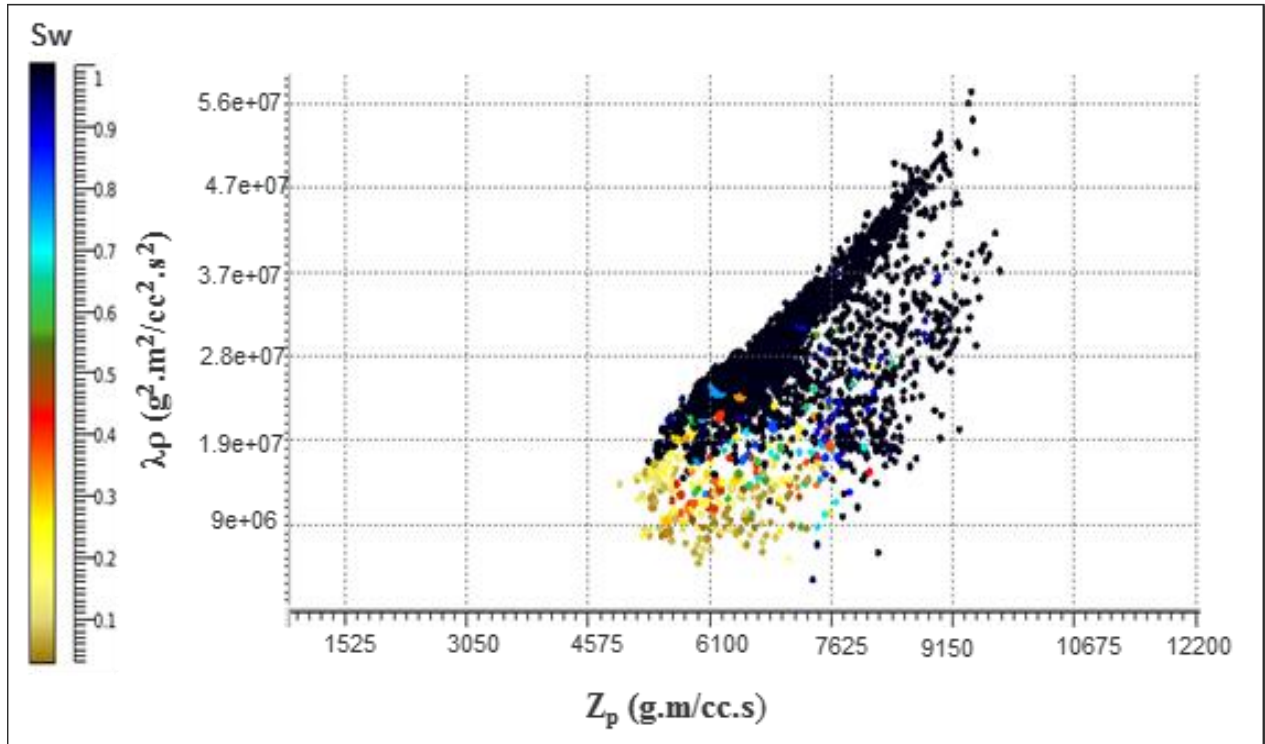
Figure 39: The plot of λρ and Z$_P$ colored by Sw.

4.1.2 Fluid Substitution

The results of the Biot - Gassmann fluid substitution analysis are displayed in Figures (40 – 43) using well Sfn-05. The values of V_P, V_S and ρ used to derive elastic properties of rock with different levels of fluids substituted in the rocks than in the in-situ conditions are shown in Figure 40 for V_P brine $> V_p$ oil $> V_p$ gas, V_S brine $< V_S$ oil $< V_S$ gas while $\rho_{brine} > \rho_{oil} > \rho_{gas}$. Comparison of N-01 and P-01 reservoirs from Sfn-05 with seismic amplitudes variation at the intervals of interest is displayed in Figure 41 while the cross plot of reflection coefficient versus angle of incidence for N-01 reservoir is shown in Figure 42. The latter shows that the hydrocarbon sand reflection coefficient becomes more negative with increasing angle of incidence in agreement with Rutherford and Williams (1989). Furthermore, the gradient versus intercept cross plot for the

shale/sand interface of the top of the reservoir N-01 in Figure 43 agreed to Castagna and Swan (1997).
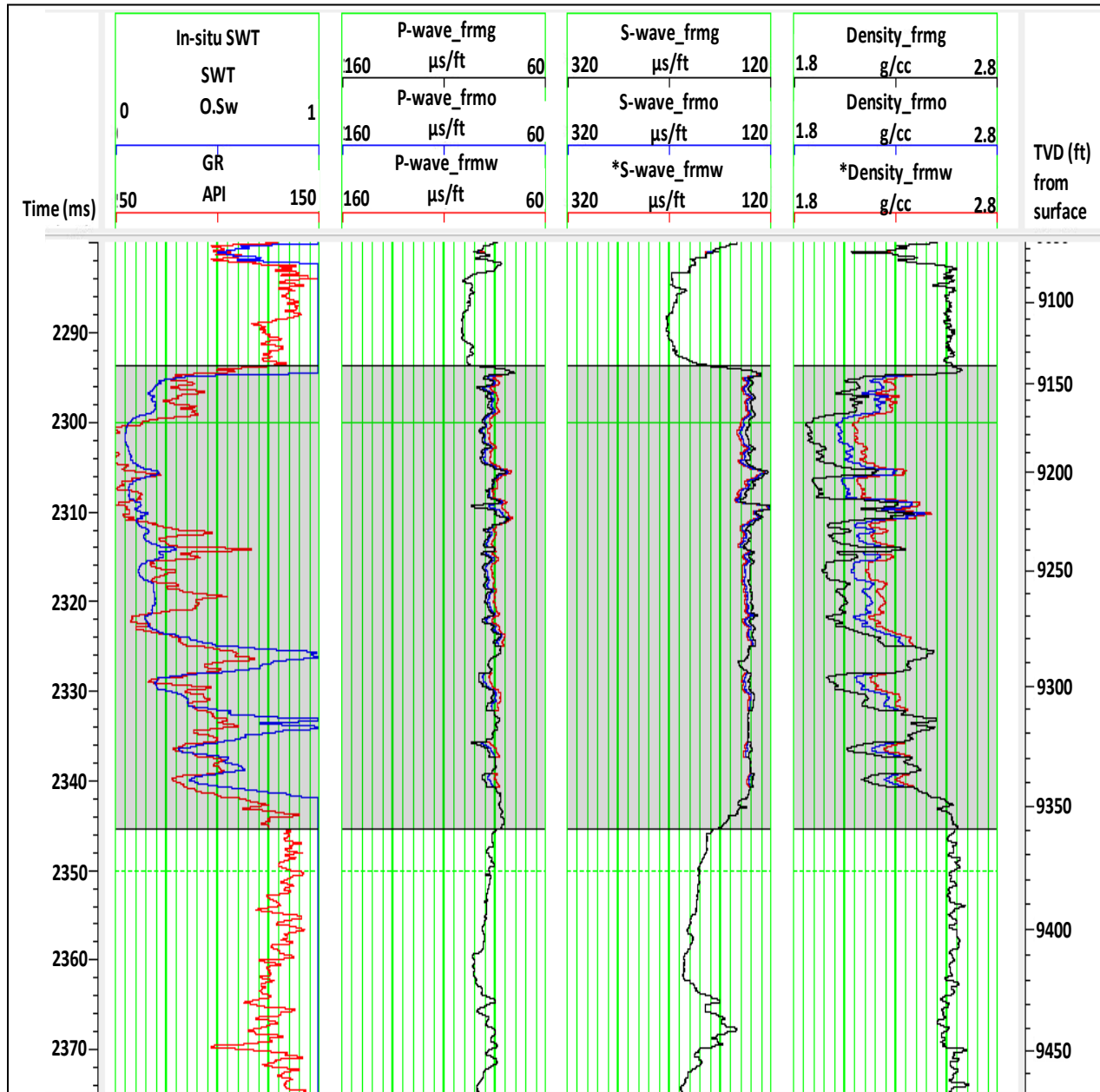
Figure 40: AVO responses when N-01 reservoir is saturated with these fluids; black (gas), Oil (blue) and brine (red).
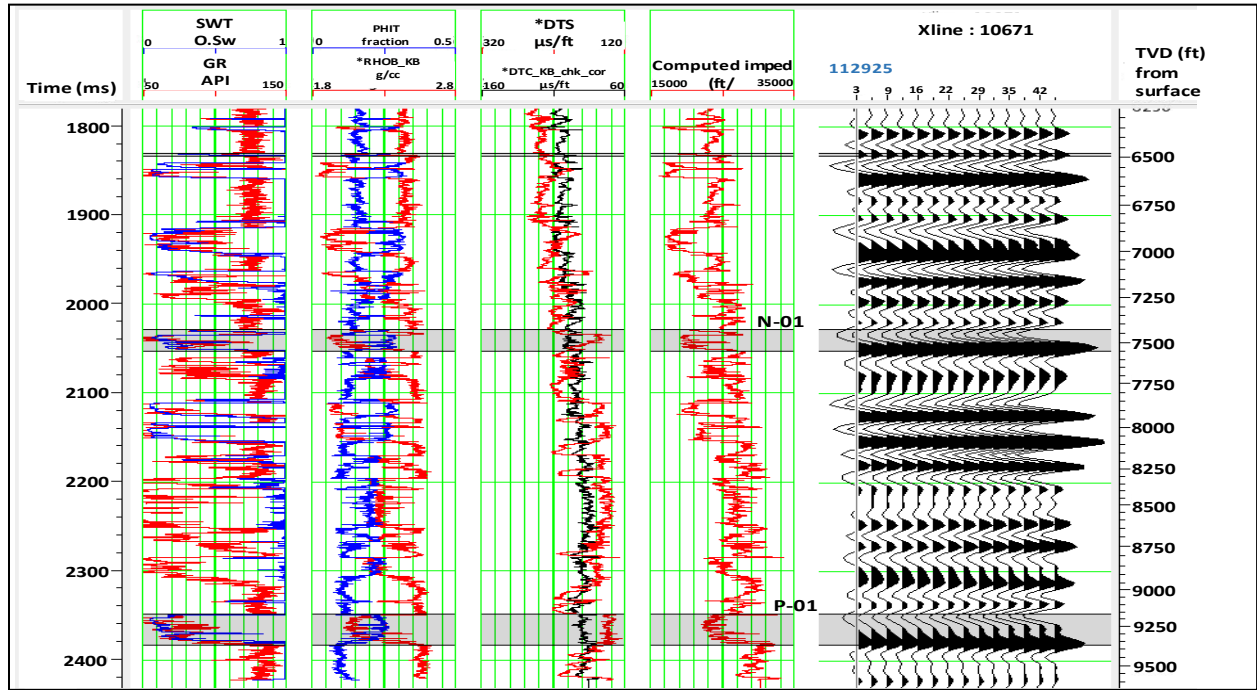
Figure 41: Comparison of N-01 and P-01 reservoirs from Sfn-05 with seismic amplitudes variation at the intervals of interest.
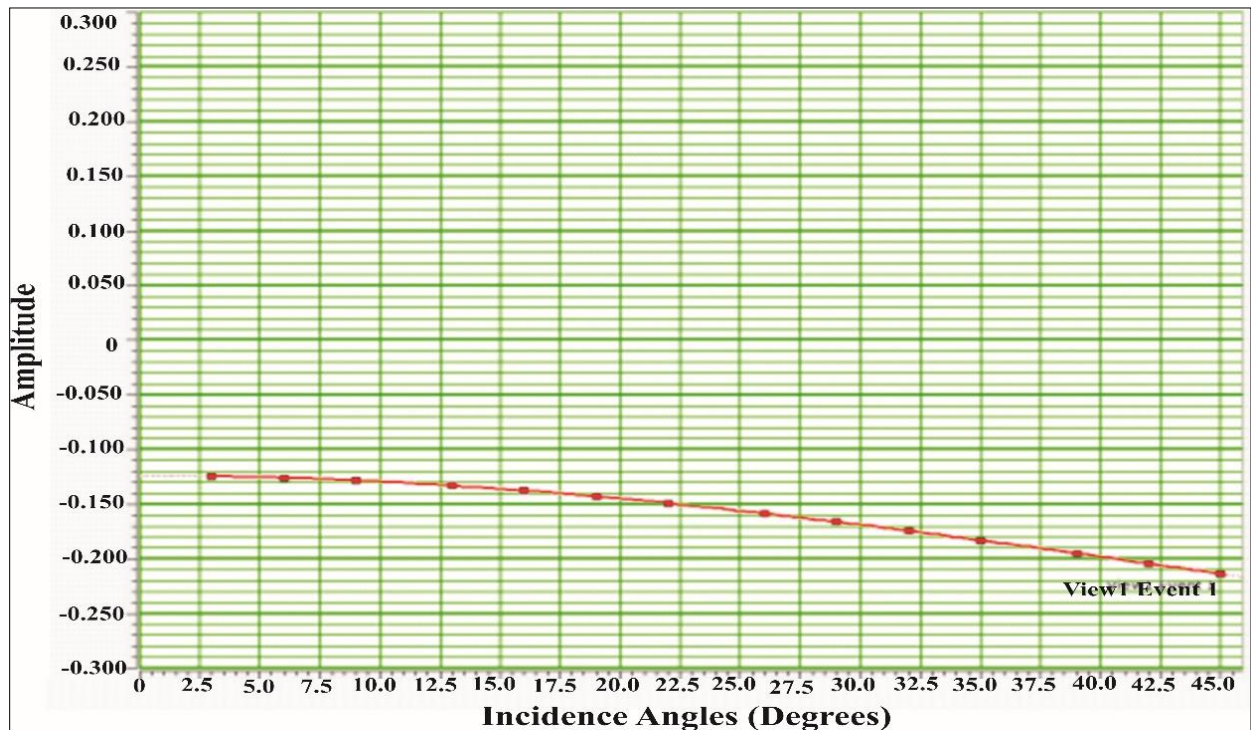
Figure 42: Plot of amplitude reflection coefficient at N-01 reservoir versus angle of incidence (Rutherford and Williams, 1989).
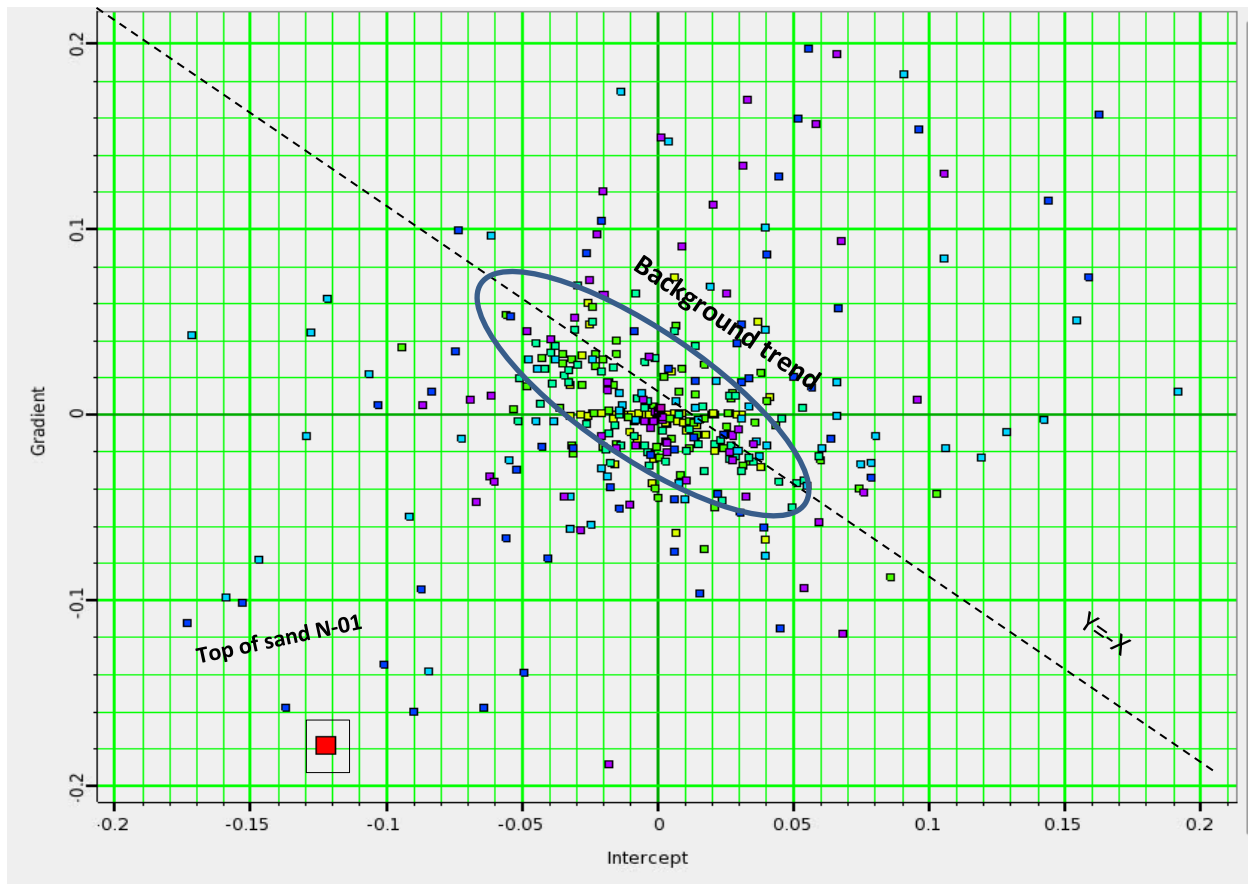
Figure 43: AVA Intercept (A) and Gradient (B) cross plot according to Castagna and Swan (1997) for N-01 reservoir.

4.2 SIMULTANEOUS INVERSION RESULTS

The inversion results are displayed in Figures (44 – 49). The P-impedance (full-bandwidth) in Figure 44 gradually increases with depth, low impedance (red) sands K01, N01and P01 match the overlain low gamma-ray log. The P-impedance (band-limited) displayed in Figure 45 shows high-impedance (blue) background shale while the low impedance (yellow) sands match the sands from the gamma-ray log. The S-impedance (full-bandwidth) in Figure 46 gradually increases with depth, low impedance (red) sands K01, N01and P01 match the overlain low gamma-ray log. The S-

78

impedance (band-limited) displayed in Figure 47 shows high-impedance (blue) background shale while the low impedance (yellow) sands match the sands from the gamma-ray log though not well differentiated from shale as compared to P-impedance volume. The Density (full-bandwidth) displayed in Figure 48 gradually increases with depth but the reservoir sands are difficult to separate from background shale. Density (band-limited) displayed in Figure 49 though noisy but still shows low density (yellow) sands N01 and P01 and high density (blue) background shale. The sands are difficult to separate from the surrounding shale, therefore P-impedance is a good lithology discriminator in the field of study. The results are in agreement with Alfaro *et al*., (2007) and Kong *et al*. (2013).
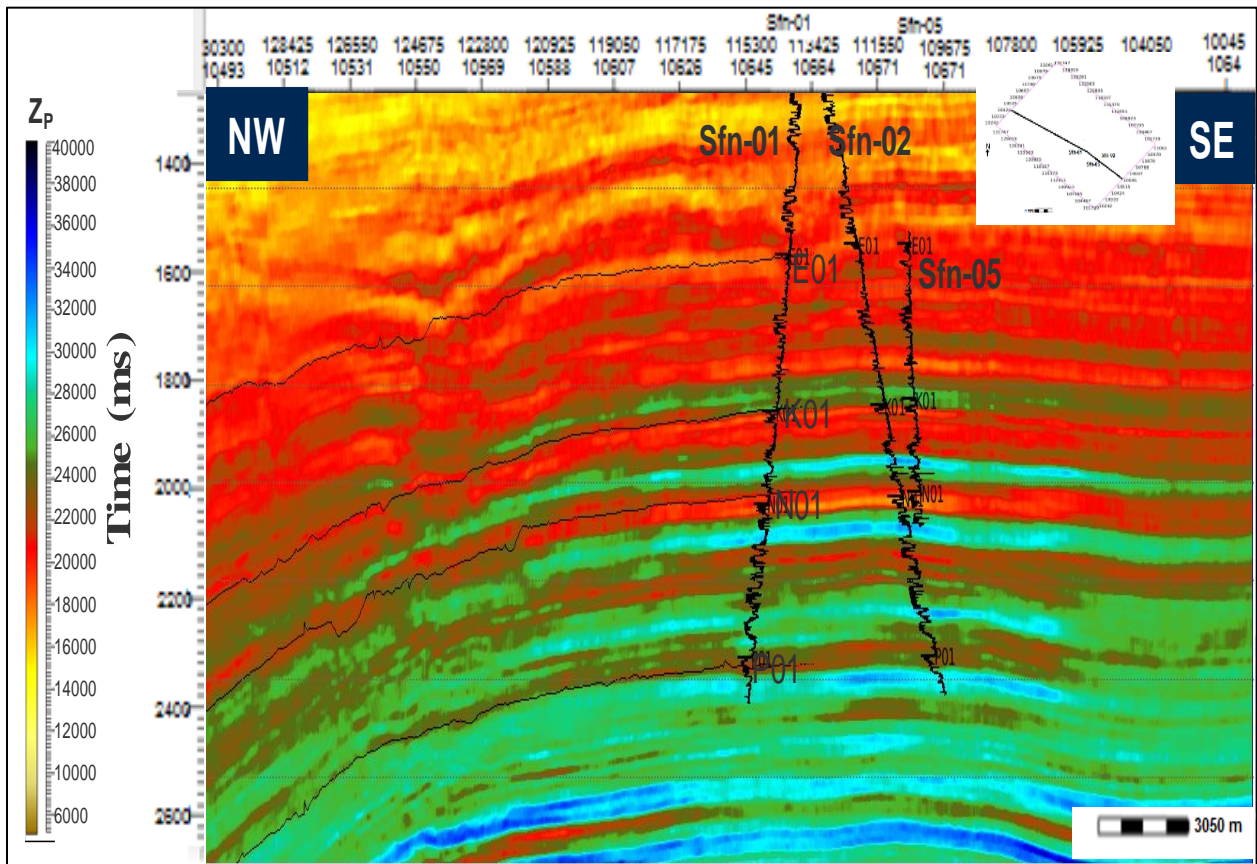
Figure 44: P-impedance (full-bandwidth) overlain with gamma ray log
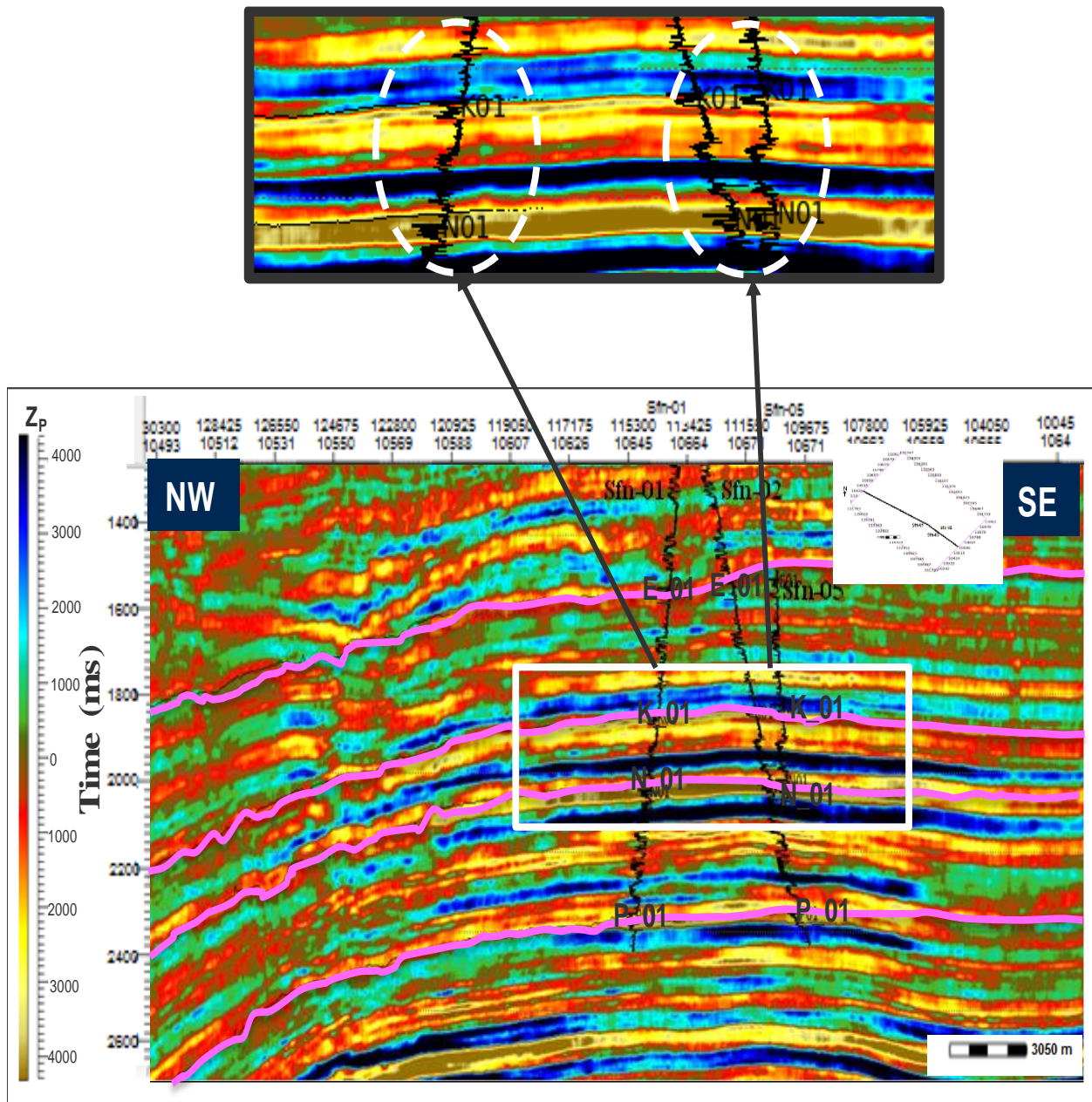
Figure 45: P-impedance (band-limited) overlain with gamma ray log
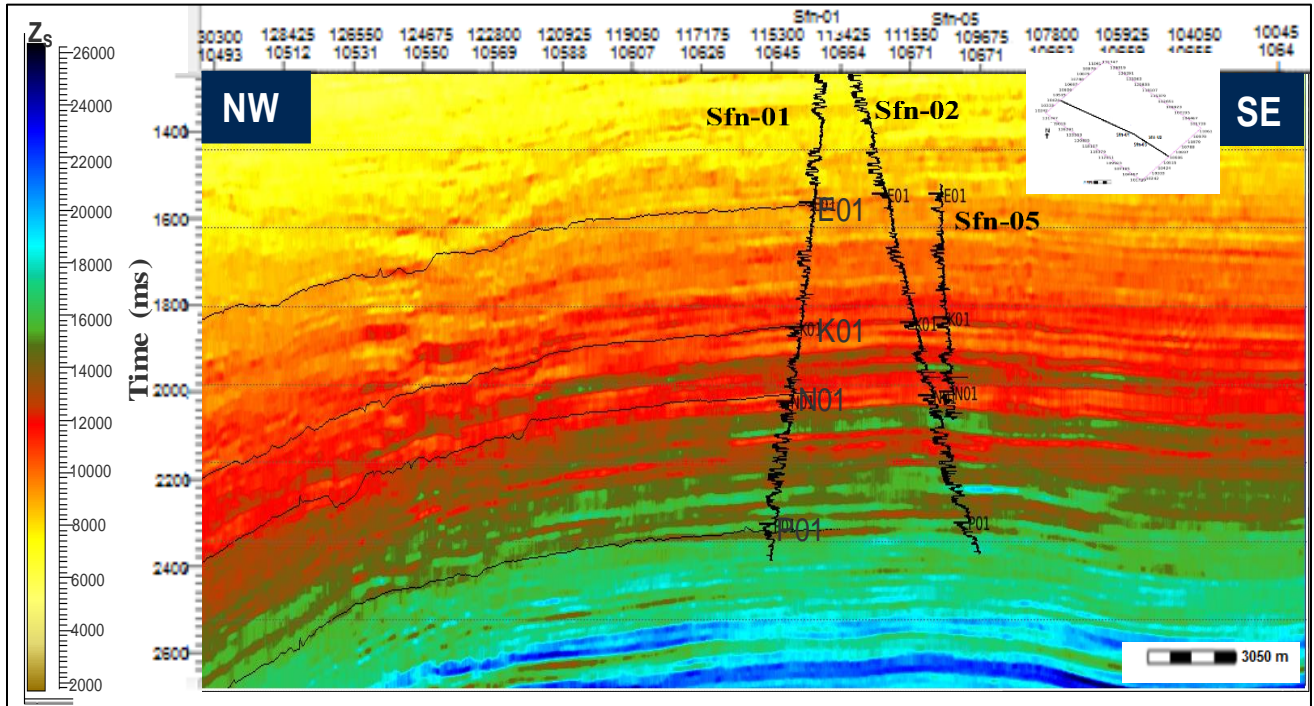
Figure 46: S-impedance (full-bandwidth) overlain with gamma ray log
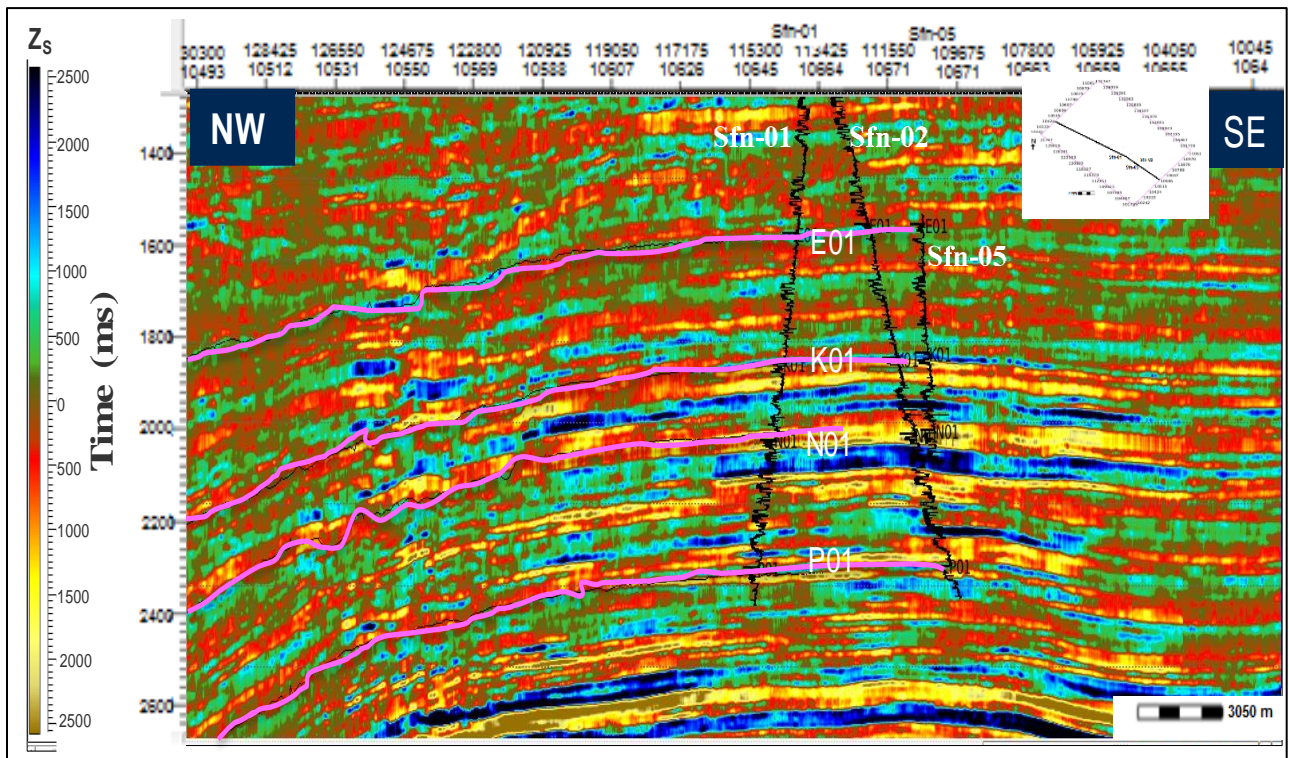
Figure 47: S-impedance (band-limited) overlain with gamma ray log
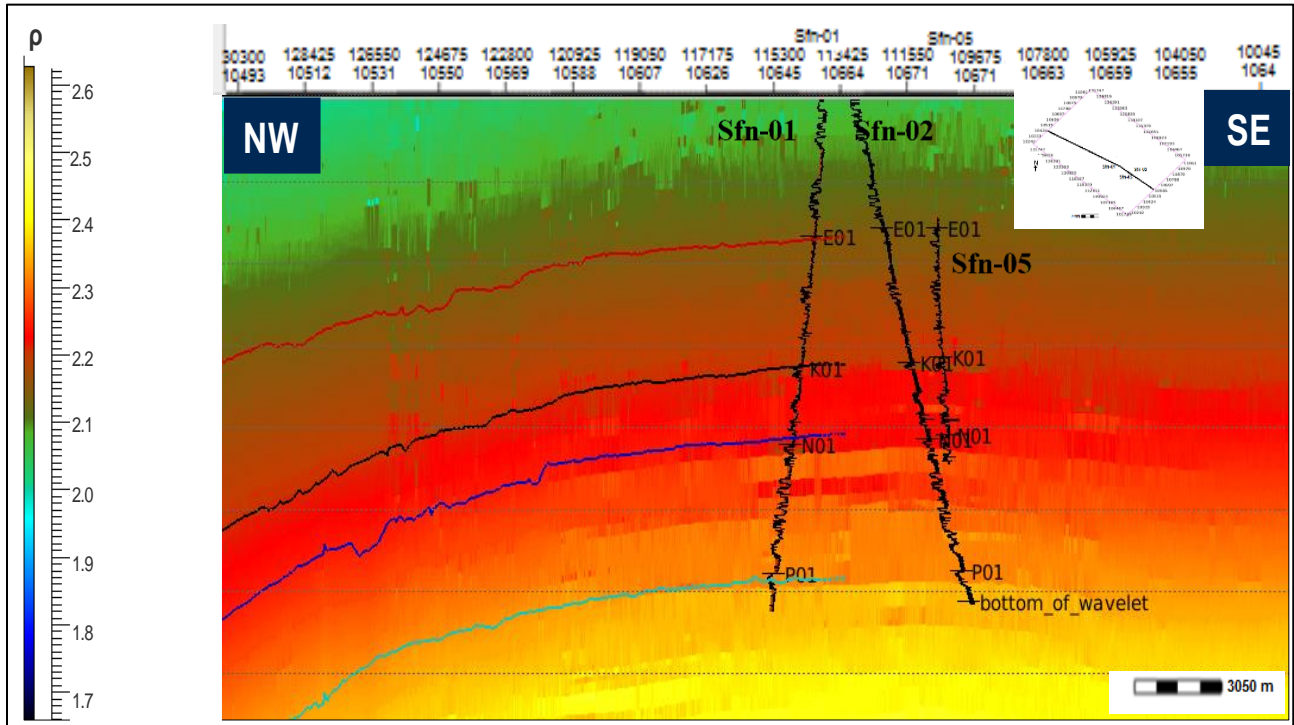
Figure 48: Density (full-bandwidth) overlain with gamma ray log
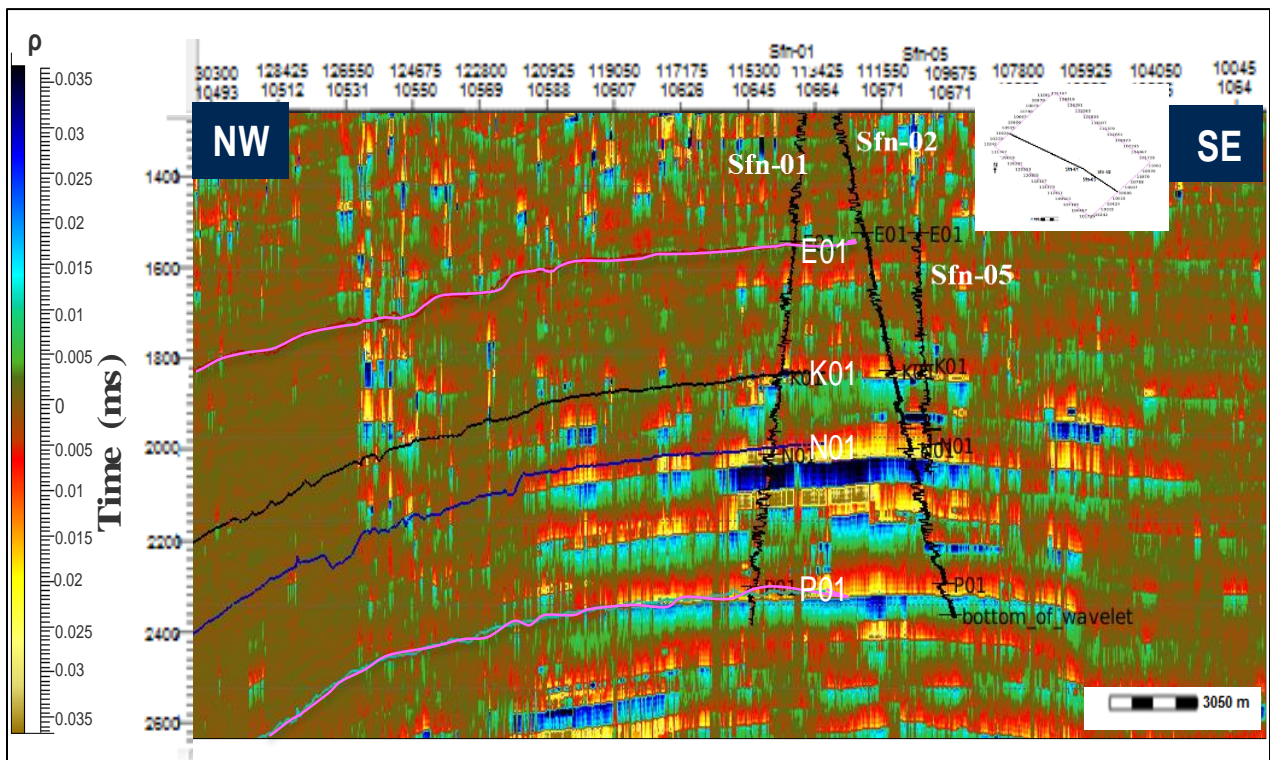
Figure 49: Density (band-limited) overlain with gamma ray log.

4.3 ELASTIC IMPEDANCE INVERSION RESULTS

The Elastic inversion volumes are displayed in Figures (50 – 53). The EI 9.2 (full-bandwidth) in Figure 50 shows the gradual increase in impedance with depth, low impedance (yellow to red) sands K01, N01and P01 match the overlain low gamma-ray log. The EI 9.2 (band-limited) displayed in Figure 51 shows high-impedance (blue) background shale while the low impedance (yellow to red) sands match the sands from the gamma-ray log. The EI 37.2 (full-bandwidth) in Figure 52 gradually increases with depth, low impedance (yellow to red) sands K01, N01and P01 match the overlain low gamma-ray log. The EI 37.2 (band-limited) displayed in Figure 53 shows high-impedance (blue) background shale while the low impedance (yellow to red) sands match the sands from the gamma-ray log. The reservoirs are more evident on the EI 37.2 inverted volumes than it is on EI 9.2 inverted volume. This agreed with the work of Veeken and Da Silva (2004) and Kong *et al*. (2013).
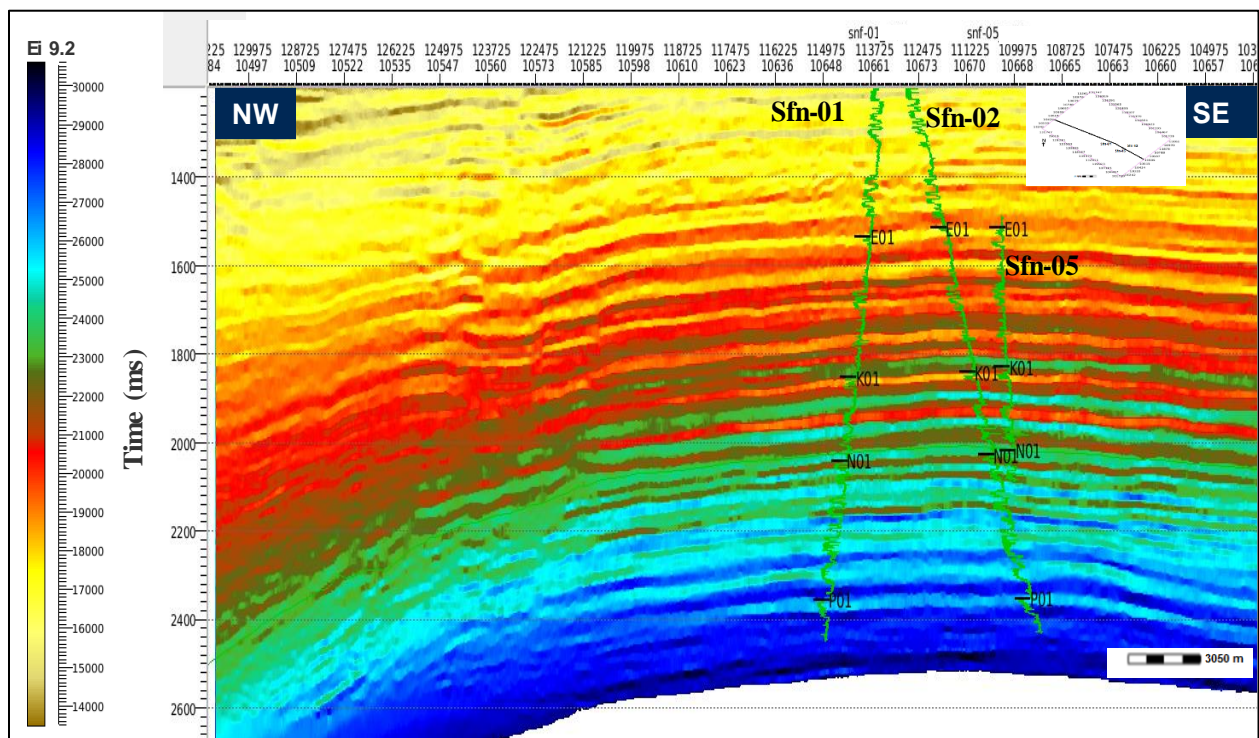
Figure 50: EI 9.2 (full-bandwidth) with overlain gamma ray log
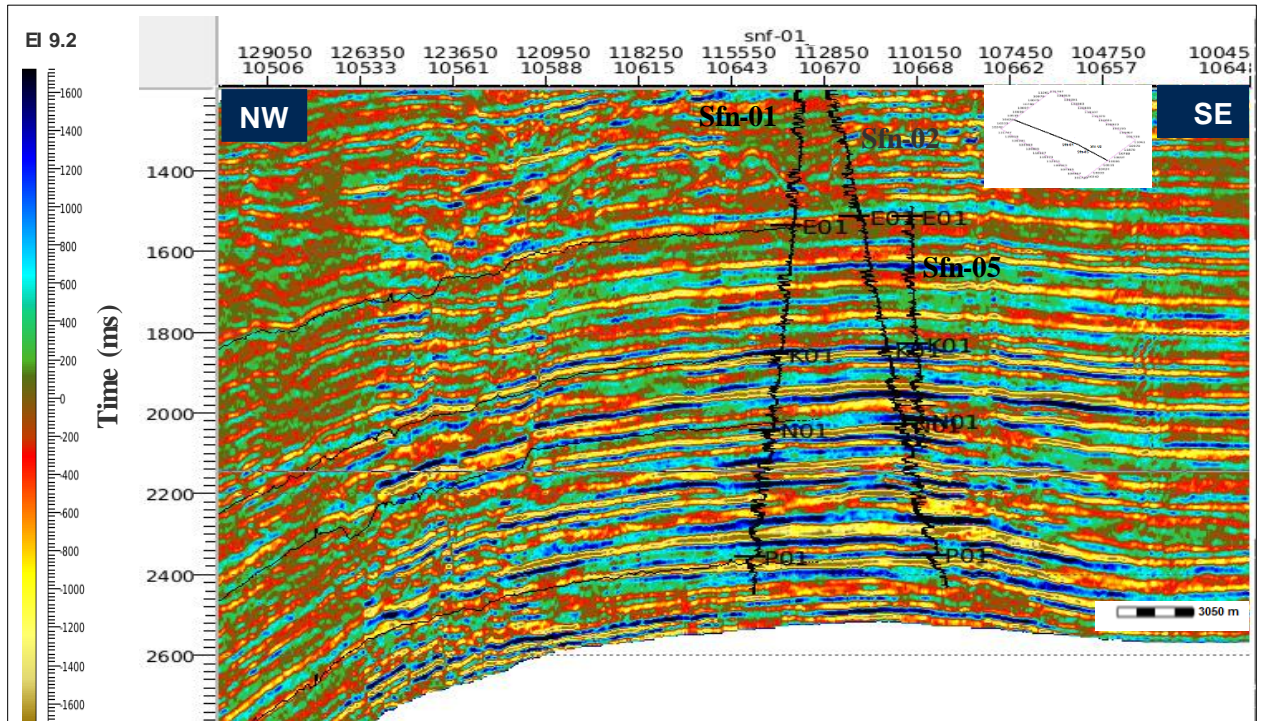
Figure 51: EI 9.2 (band-limited) with overlain gamma ray log
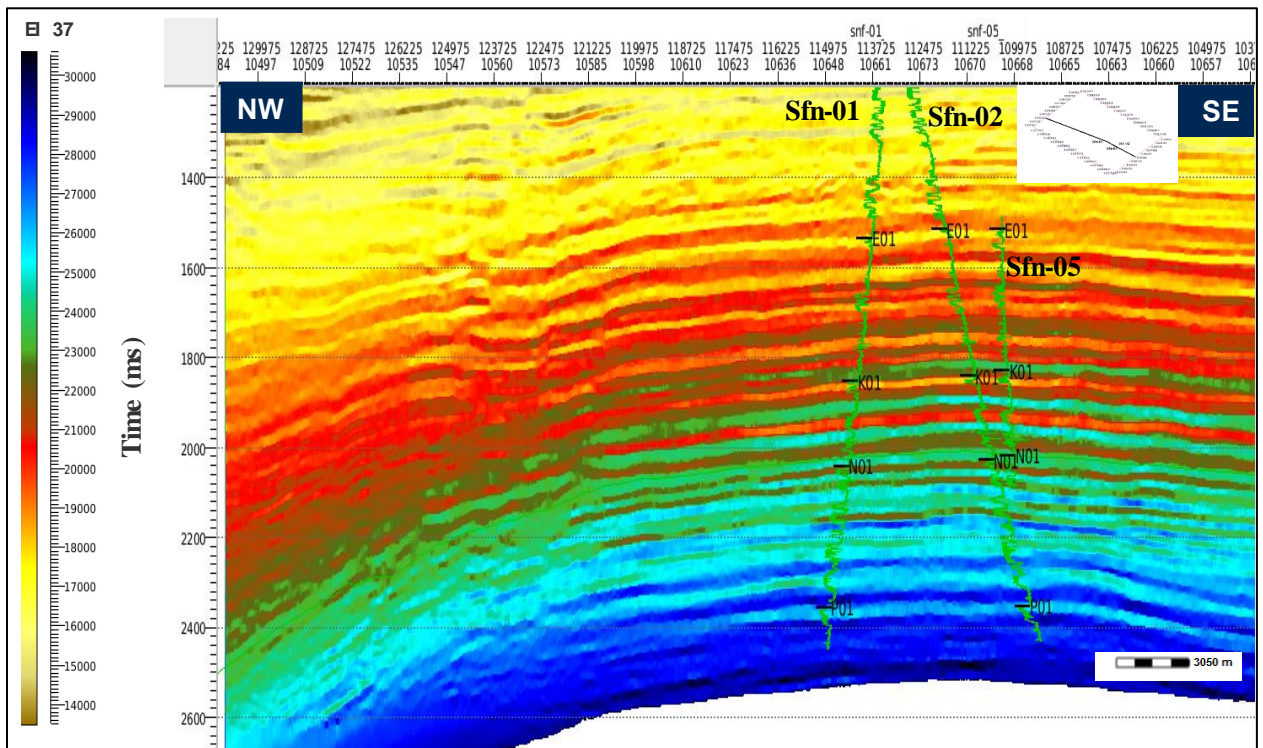
Figure 52: EI 37 (full-bandwidth) with overlain gamma ray log
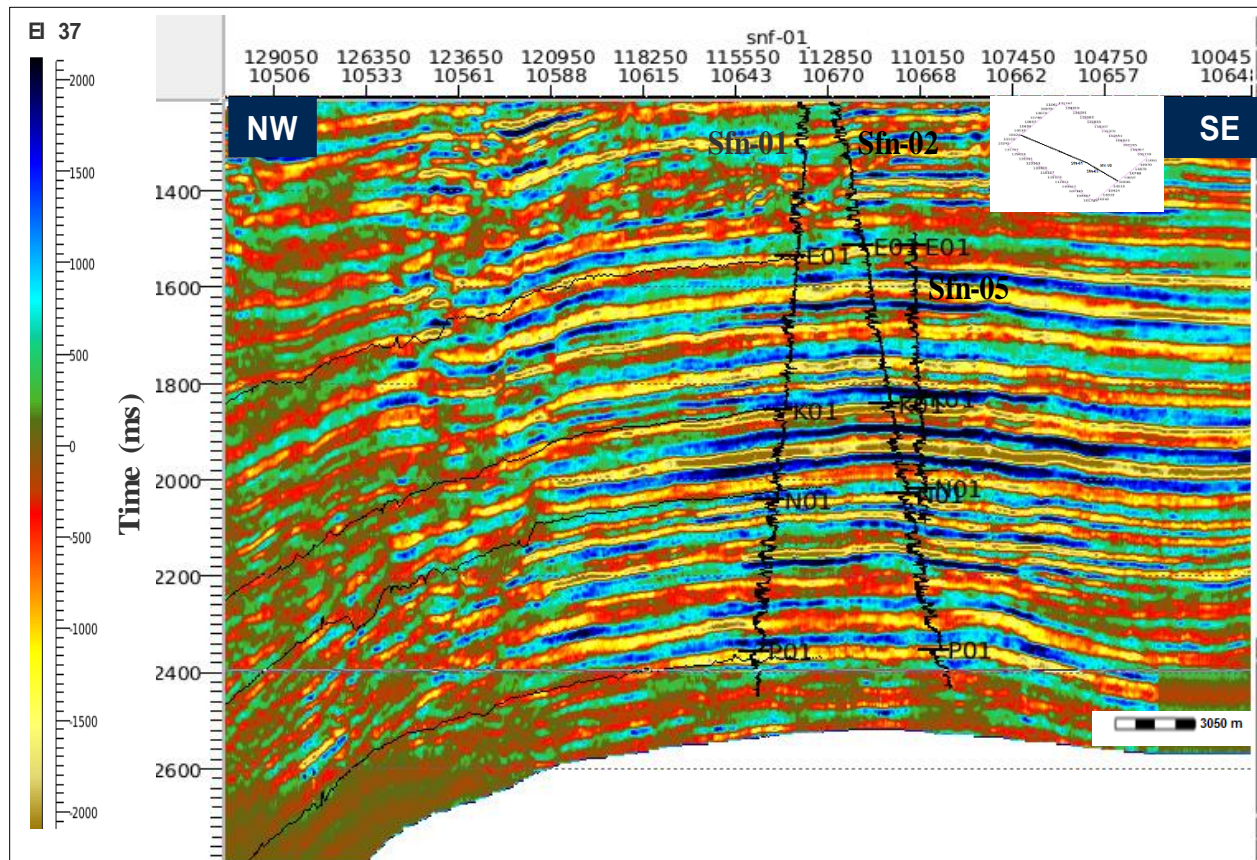
Figure 53: EI 37 (band-limited) with overlain gamma ray log

4.4 DERIVED VOLUMES

Figure 54 shows high resistivity response from the overlain resistivity log coinciding with low lambda-rho (yellow to red). Low lambda-rho indicates hydrocarbon sand therefore lambda-rho is a good litho-fluid discriminator in area of investigation similar to observation of Flippova (2011). Figure 55 is the mu-rho volume which reflects density variation with depth though the delineation of the lithologic units is not so good. Figure 56 shows high resistivity response from the overlain resistivity log having a good match with low Poisson's ratio (yellow to red) which indicates presence of hydrocarbon. Therefore, Poisson's ratio is a good fluid discriminator in this field which agreed with Smith and Gildlow (1987). The Poisson's ratio volume also reflects lateral continuity of reservoirs and good connectivity between the wells which suggests continuous sand.
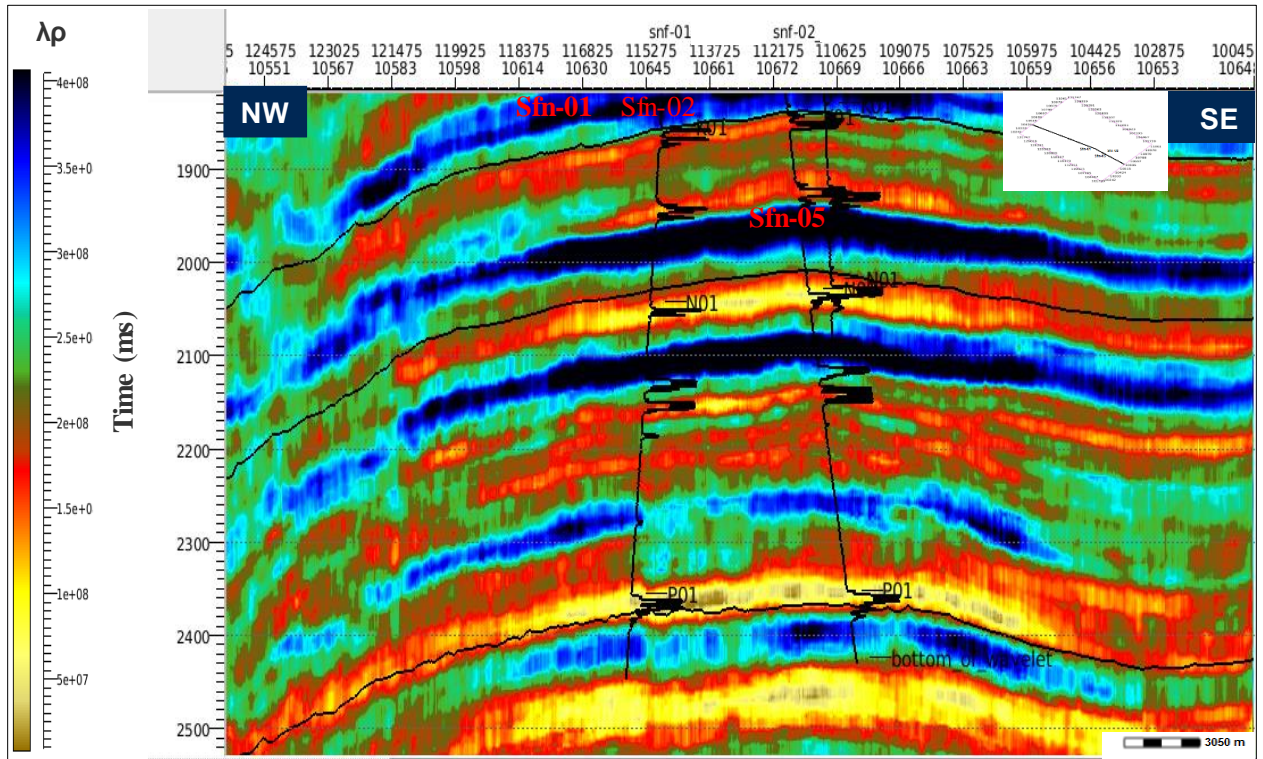
Figure 54: Lambda-rho with overlain resistivity log
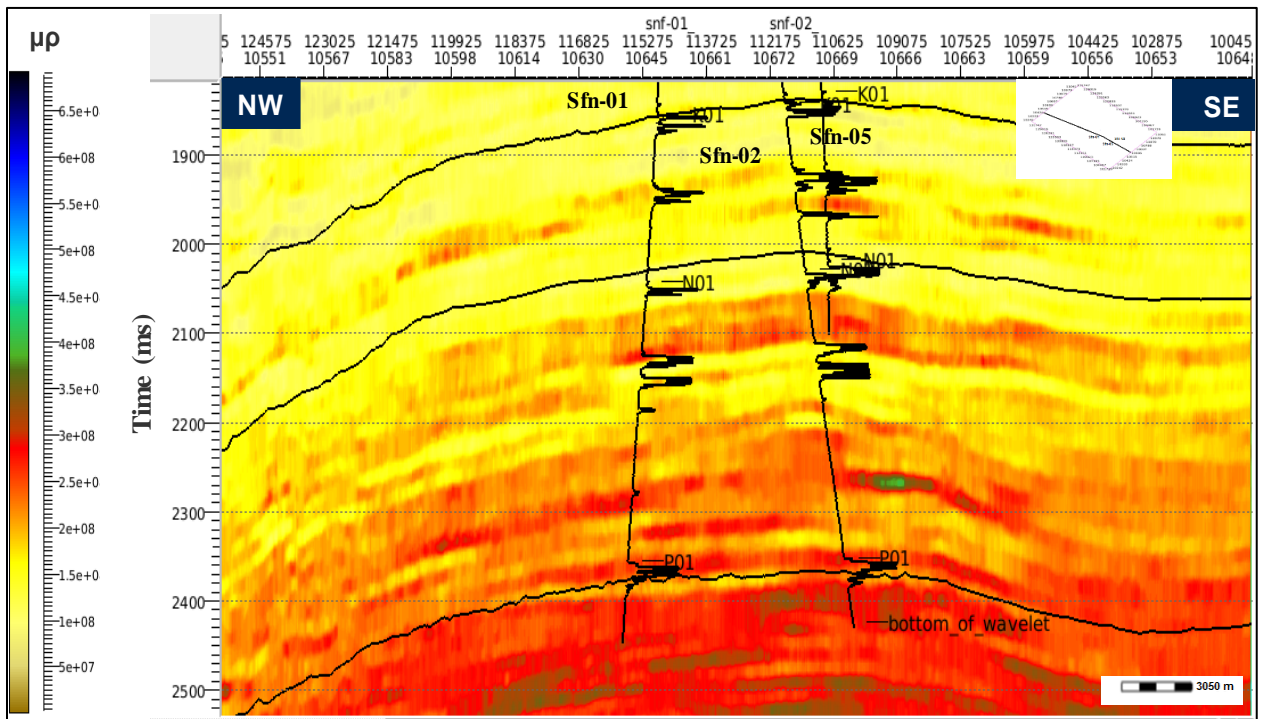
Figure 55: Mu-rho with overlain resistivity log
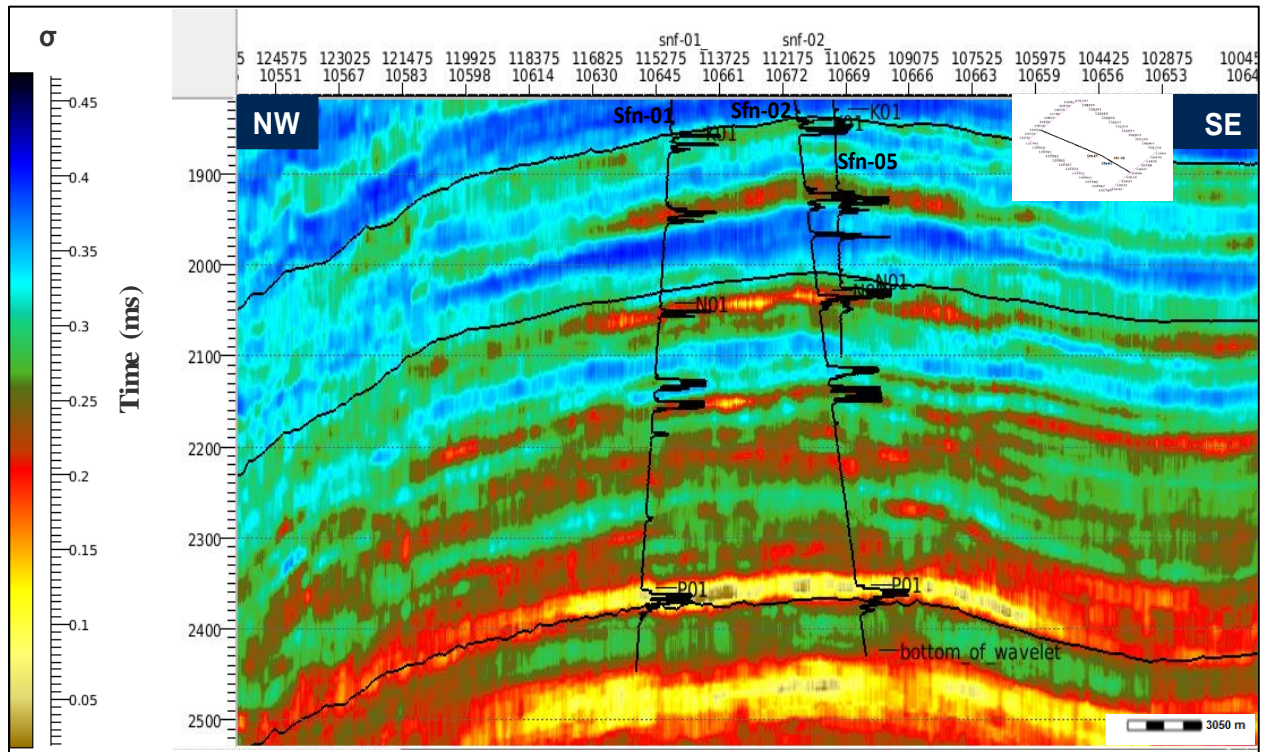
Figure 56: Poisson's ratio overlain resistivity log

4.5 THE RELATIONSHIP BETWEEN INVERTED VOLUMES AND PETROPHYSICAL LOGS

4.5.1 Cross plot of Inverted P-Impedance and Well P-Impedance

Figure 57 is the display of the cross-plot of the inverted P-impedance and well P-impedance from which a linear regression equation $Y = 0.688729X + 1839.15$ (g.m/cc.s) was derived. The regression equation could be rewritten as Inverted $Z_p = 0.688729$ Well $Z_p + 1839.15$ (g.m/cc.s). The comparison of the inverted P-impedance and well P-impedance gave correlation coefficient of 86% which indicates high quality inverted volume. The inverted volume predicted well P-impedance away from well control this will help reduce exploration risk in 'Sandfish Field'. The derived linear regression equation could be adopted in other fields with limited well data but with similar geological setting.

87
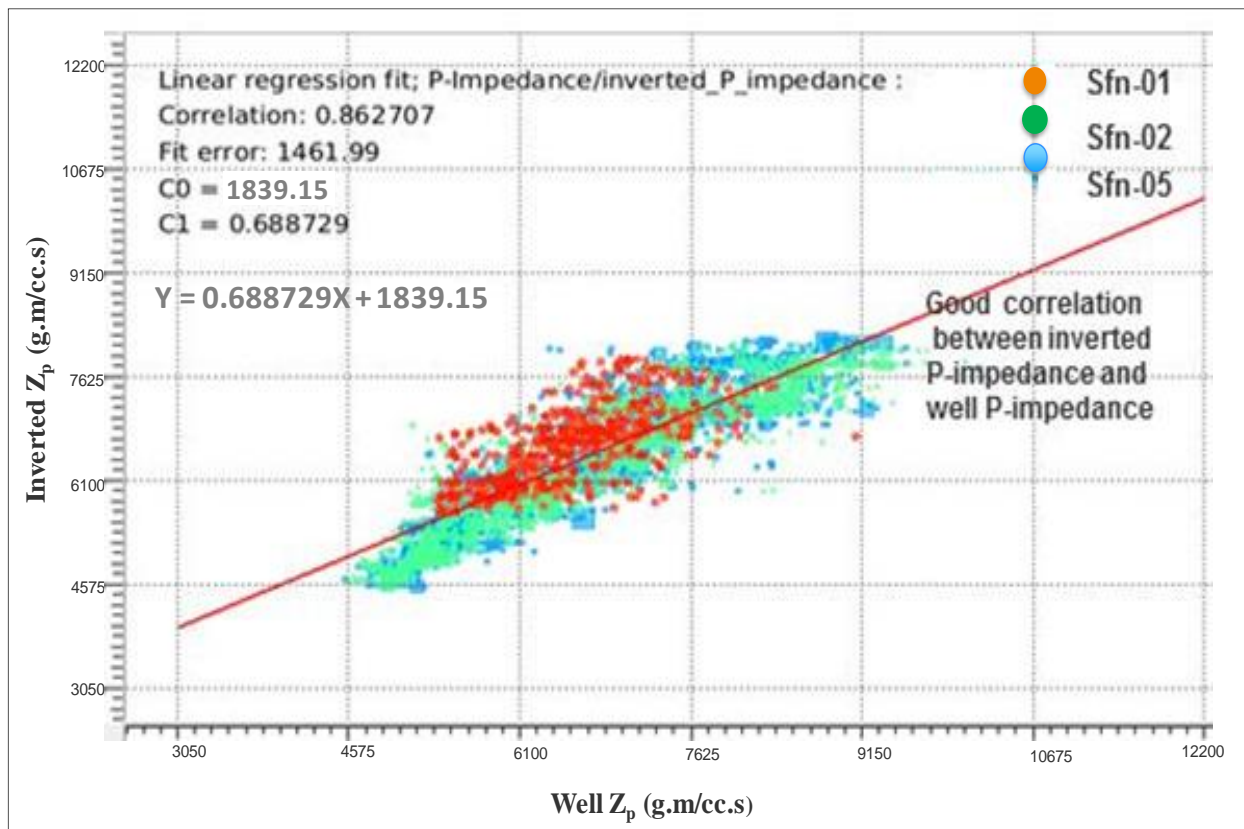
Figure 57: Cross plot of the Inverted Z_p and well Z_p

4.5.2 Comparison between Inverted P-impedance (band pass) and Well impedance (filtered)

Figure 58 shows the extracted P-impedance band limited (orange) at the three well locations (Sfn-01, Sfn-02, and Sfn-05) overlain by the filtered well P-impedance (blue). The well log P-impedance was first filtered to seismic frequency range to establish the validity of this relationship. A very good match is observed between the band pass Pseudo P- impedance extracted at the well locations and the filtered P-impedance from the well logs. This reflects high quality of the modeled seismic and well data.
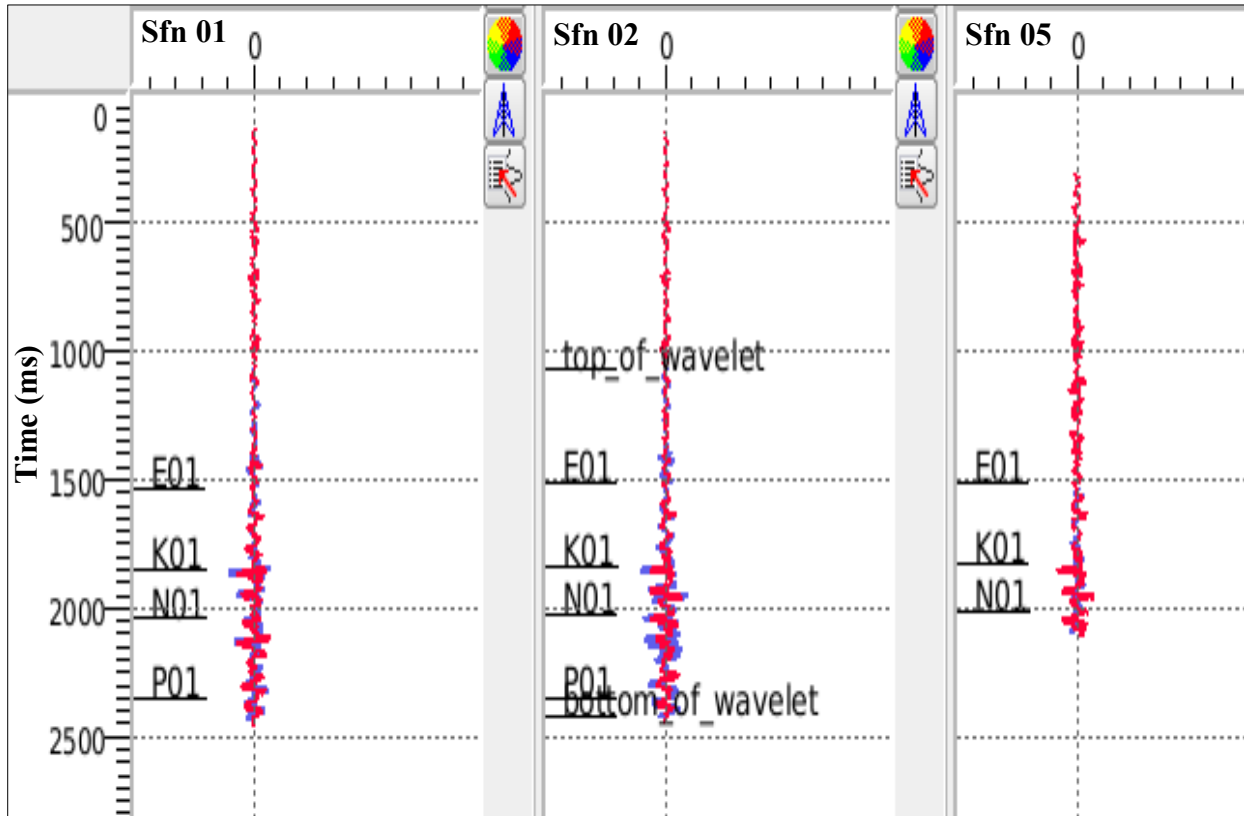
Figure 58: Inverted P-impedance band pass (orange) and well P-impedance filtered (blue)

4.5.3 Blind Test

This is a QC carried out to validate inversion results away from the well control. The blind test reveals heterogeneities in reservoir properties away from the wells. Inverted P-impedance was overlain with gamma ray log from Sfn-04 and Sfn-05 displayed in Figure 59. Sfn-04 was not used in the inversion but the gamma ray log shows a good match with the N01 sand top away from well control.
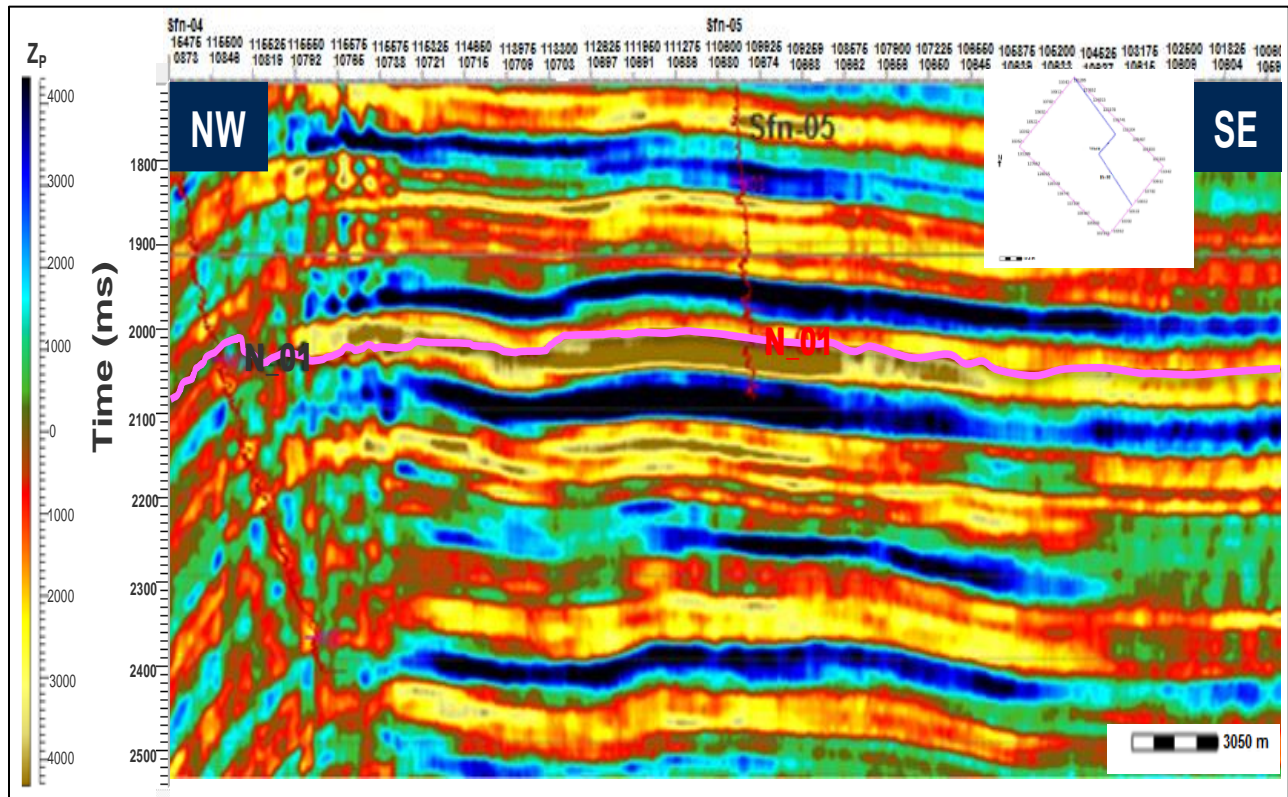
Figure 59: Sfn-04 shows good match with N01 sand top away from well control.

4.6 CORRELATION OF INVERTED VOLUMES

4.6.1 Comparison of Elastic impedance (near and far-far) with P-impedance from Simultaneous inversion (full bandwidth)

The elastic impedance inversion for near and far-far angle stacks were carried out to compliment the simultaneous inversion results. The elastic volumes show good correlation at 1850 ms and 2050 ms which represent sands K01 and N01. The reservoirs are of low P-impedance (4880 to 6710) g.m/cc.s, the sands matched the low gamma response at the wells displayed in Figure 60. Although the prospects are more visible at the far-far elastic volume compared to P-impedance from simultaneous inversion and near elastic volume.

4.6.2 Comparison of Elastic impedance (near and far-far) with P-impedance from Simultaneous inversion (band limited)

The comparative results of elastic impedance for near and far-far angle stacks with the inverted P-impedance from simultaneous inversion displayed in Figure 61 shows quality sand of low P-impedance at 1850 ms and 20430 ms which are within sands K01 and N01. The sands matched with the gamma response at the wells indicative of quality inverted volumes. Although more prospect zones are revealed in the Elastic impedance volumes.

4.6.3 Comparison of Inverted Volumes

Figure 62 is the display of the cross plot of the inverted P-impedance and EI 37.2 (Far-far elastic impedance) from which a linear regression equation $Y = 0.420135X + 3.67E6$ (Kg/m^{2}s) was derived. The regression equation could be rewritten as Inverted Z_p = 0.420135 EI 37.2 + 3.67E6 (Kg/m^{2}s). The comparison of the inverted P-impedance and EI 37.2 gave correlation coefficient of 82% which shows good qualitative agreement between the inversion products. The derived linear regression equation could be used to predict Far-far elastic impedance in other fields with similar geological setting.

4.6.4 Comparison of seismic amplitude data with inverted volume

The Figure 63a is the initial seismic section before inversion while Figure 63b is the inverted lambda-rho volume. The inversion was carried out due to the inability of the seismic data to define some subsurface structures properly. The subtle features identified on the seismic data (Fig. 63a) shows what looks like a fault and bright spots. The Figure 63b revealed discontinuity that confirmed the presence of Fault, identified the continous sand and better discriminate the lithology

and fluid types in the prospect zones. The result shows that inverted product (Fig. 63b) easily connect reservoir properties to fundamental rock properties e.g. compressibility (λ) and rigidity (ρ) than to traditional seismic attribute (amplitude). By converting boundary interface property to layer property of higher precision. Thus, quantitative information of reservoir properties are obtained.
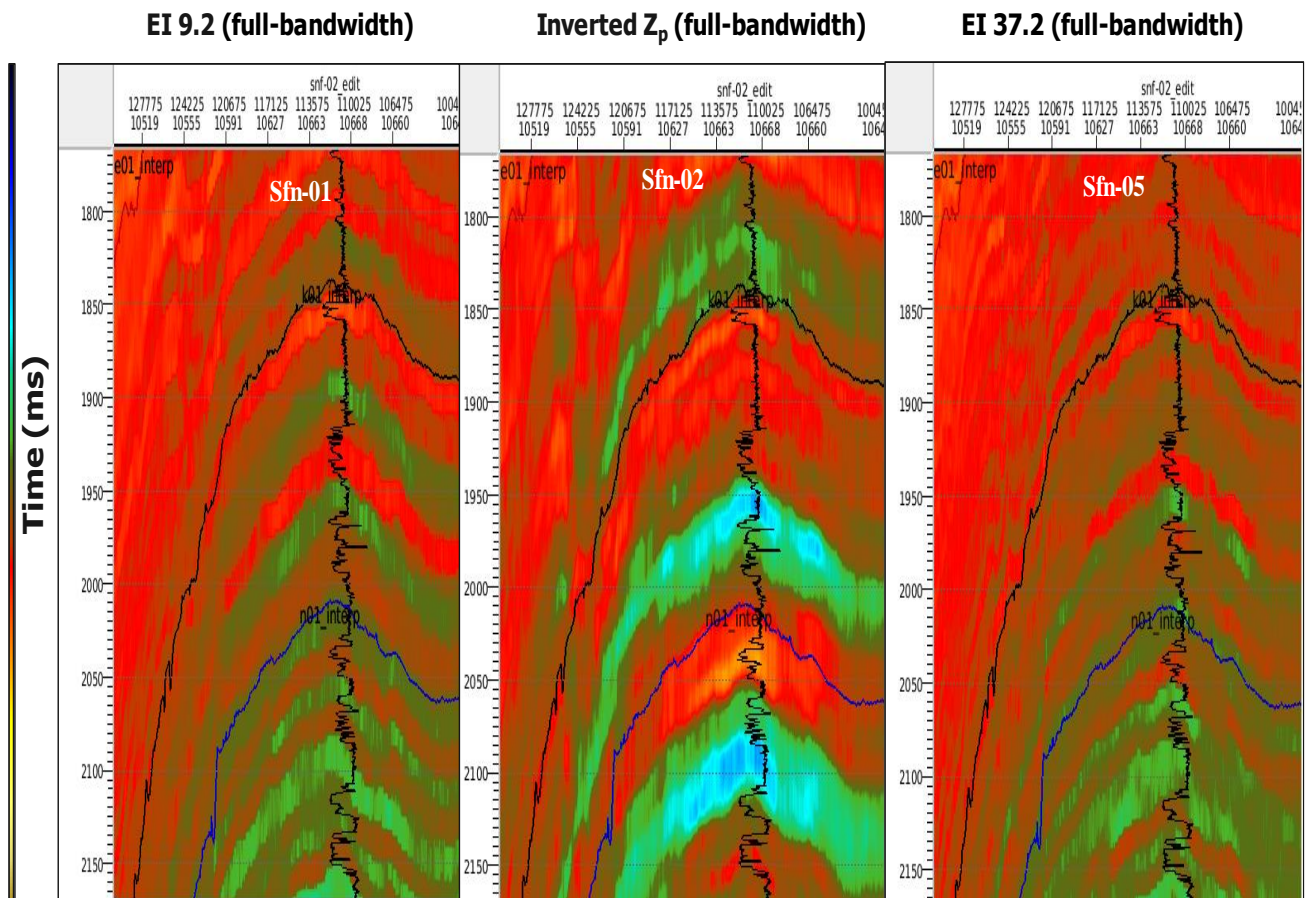
Figure 60: Comparison of Elastic impedance (near and far-far) with P-impedance.
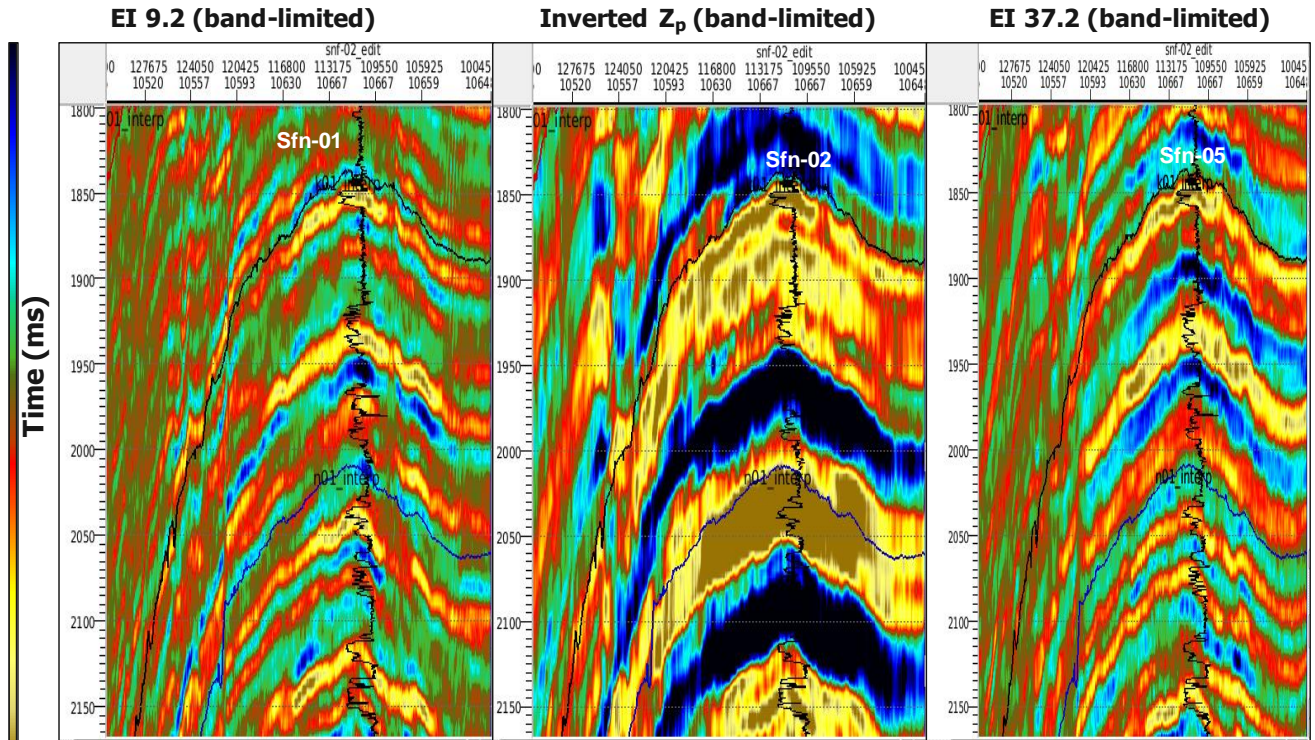
Figure 61: Comparison of Elastic impedance (near and far-far) with P-impedance
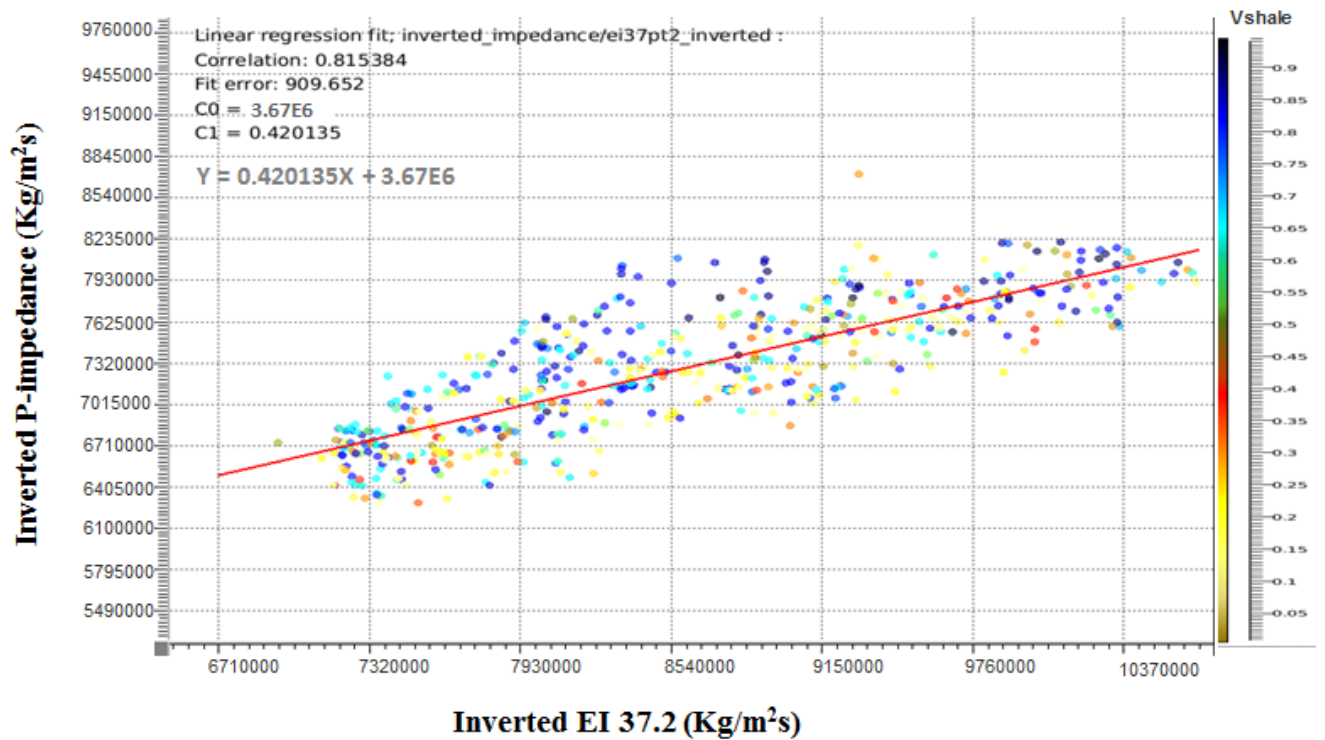
Figure 62: Cross plot of Inverted P-impedance and EI 37.2 (Far-far elastic impedance).

93
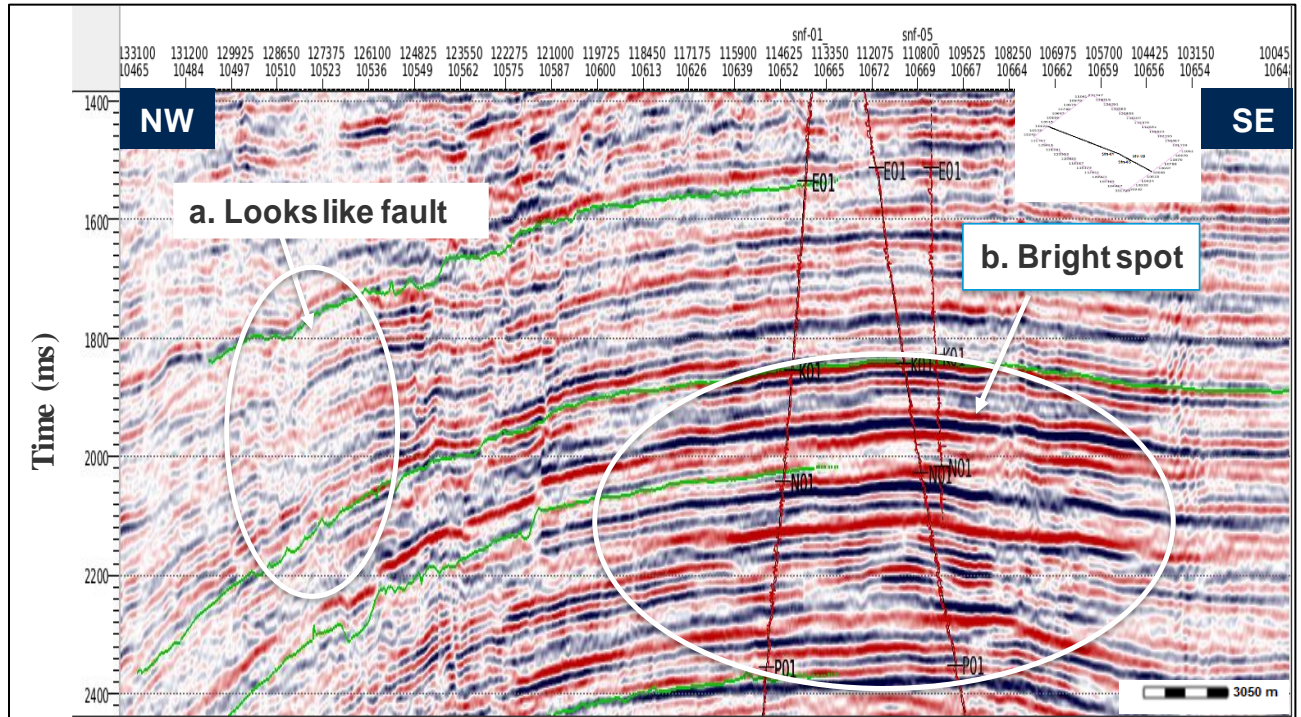
Figure 63a: Initial seismic section with subtle features
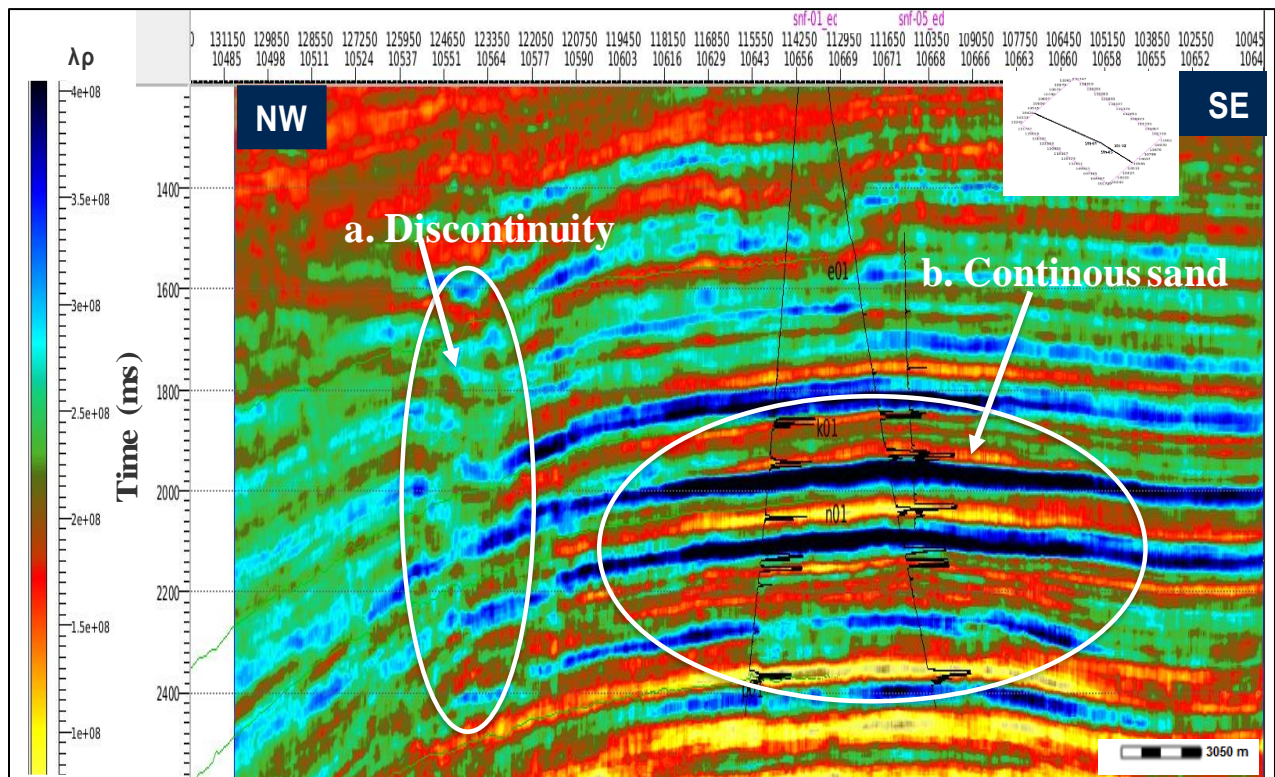
Figure 63b: Lambda-rho better discriminate the lithology and fluid types at prospect zones.

4.7 SEISMIC ATTRIBUTE EXTRACTION

4.7.1 Lithology and Fluid Prediction Map

Figure 64 is the map view which shows the lateral distribution of Vsand extracted at top of N-01 reservoir. The red to yellow represents high volume of sand while blue indicates low Vsand. The map shows good lateral continuity of reservoir at the south-center similar to shore-face depositional environment. Figure 65 is the display of the gamma-ray log and the extracted derived inverted volumes at the N-01 reservoir in well logs; inverted Vsand (blue), gamma-ray log (green), inverted Poisson's ratio (red). Hence, Figures 64 and 65 show the lateral and vertical variation of reservoir properties at N-01 reservoir. Figure 66 is the Fluid prediction map which shows the lateral variation of Poisson's ratio extracted at top of N-01 reservoir. This reflects the hydrocarbon saturation in the sand. The high Poisson's ratio (yellow) indicates low hydrocarbon saturation while low Poison's ratio (green to blue) indicates high hydrocarbon saturation.
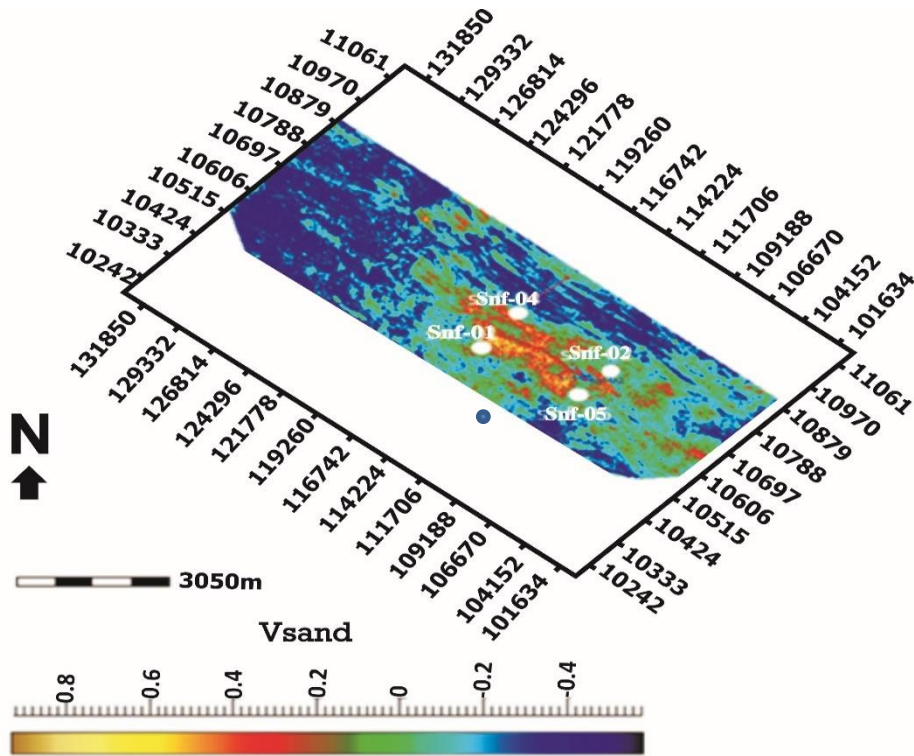
Figure 64: Lithology Map
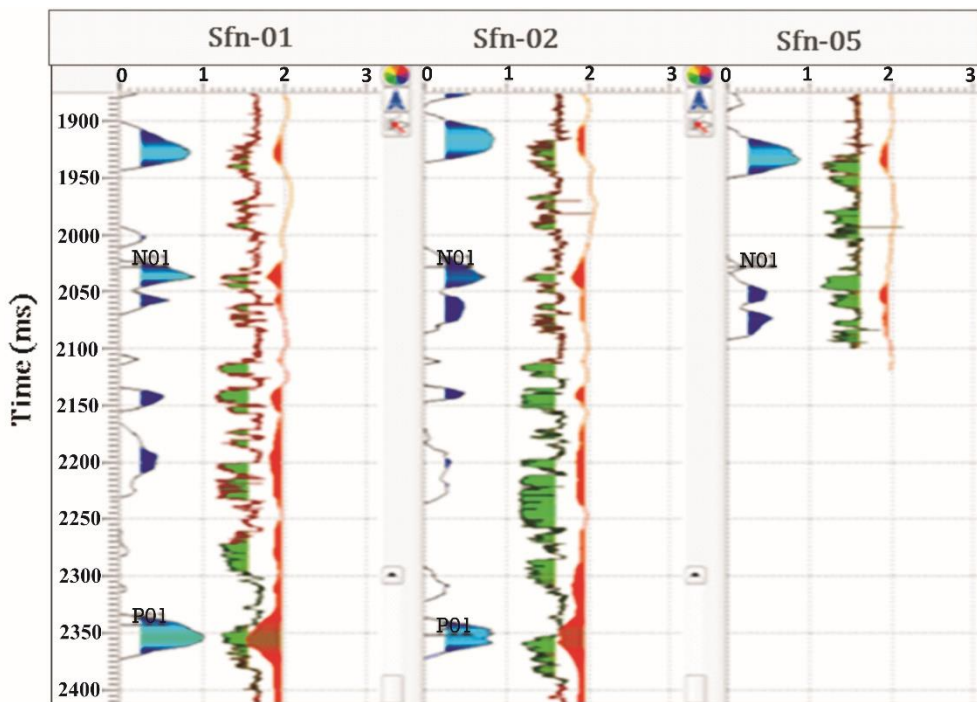
Figure 65: Vsand (blue), gamma ray (green), Poisson's Ratio (red)
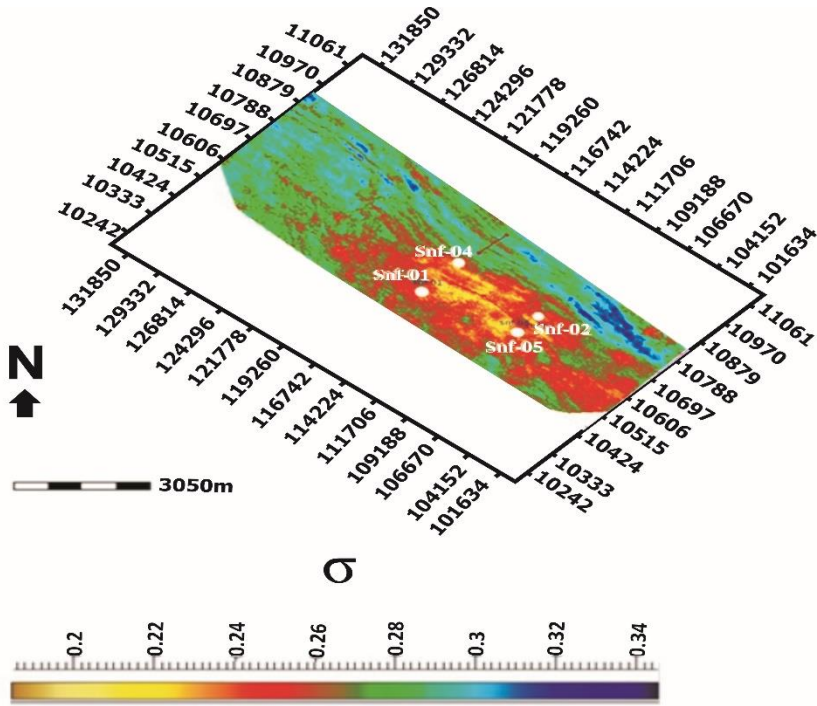
Figure 66: Fluid Prediction Map

5.0 SUMMARY AND CONCLUSIONS

5.1   SUMMARY OF FINDINGS

OBJECTIVES OF STUDY	SUMMARY OF FINDINGS
1. Carry out AVA sensitivity analysis in area of investigation;	i. The cross plots revealed that P-impedance and S-impedance are good lithology and fluid discriminators in the field of study and described the N-01 reservoir as low impedance sand. ii. The Fluid substitution analysis show different AVO responses for different fluids; gas (grey), oil (blue) and brine (red) which further established the presence of hydrocarbon.
2. Generate elastic volumes from Simultaneous and Elastic impedance inversions;	The inverted volumes (P-impedance, S-impedance, density, mu-rho, lambda-rho, Poisson's ratio, near and far-far impedance volumes) showed good match with the petrophysical variables.
3. Establish relationships between inverted volumes and petrophysical logs in area of study;	The cross plot of inverted P-impedance and well P-impedance gave a correlation co-efficient of 86% indicative of high quality inverted volume. The regression equation generated predicted well P-impedance away from well control. This will reduce exploration risk in 'Sandfish' Field and other fields with similar geological setting.
4. carry out blind well test to validate inversion products away from well control;	The inversion products showed good match with well logs from Sfn-04 away from the well control. This technique could be adopted in other fields with limited well data but with similar geological setting.
5. Compare inverted volumes from Simultaneous and Elastic impedance inversion techniques;	The elastic volumes revealed good qualitative agreement at 1850 ms and 2050 ms which represent sands K-01 and N-01, though the prospects are more visible at the far-far elastic impedance volume.
6. Generate fluid probability and lithology maps along horizon of interest in the area of study.	The low Poisson's ratio from the fluid prediction map indicated presence of hydrocarbon while lithology map reflected high Vsand of good quality

5.2 CONCLUSIONS

i. The Sensitivity analysis carried out established that P-impedance and S-impedance could be used as a lithology and fluid discriminator in the field of study. It further established the presence of hydrocarbon and described the N-01 reservoir as low impedance sand.

ii. The inverted volumes showed good match with the petrophysical variables; arising from the good match of overlain well logs on inverted volumes e.g. low gamma response having good match with low P-impedance and high resistivity response having great match with low Poisson's ratio.

iii. The cross plot of Inverted P-impedance and well P-impedance gave correlation coefficient of 86% indicative of high quality inverted volume. The regression equation generated predicted well P-impedance away from well control. This will reduce exploration risk in 'Sandfish' Field and other fields with similar geological setting.

iv. The inverted S-impedance and P-impedance described the reservoirs (K01, N01, P01) at depth 2179 m, 2484 m, and 3048 m as low impedance sands with net-gross thickness of about 30.5 m from well data.

v. The study revealed that lambda-rho is a better lithology and fluid discriminator when compared with other derived elastic volumes used in the study.

vi. A good match was established between the pseudo logs extracted from inverted volumes and the original logs at the well locations. The inversion results further showed good match with well logs from Sfn -04 away from the well control. Hence, the technique could be adopted in other fields with limited well data with similar geological setting.

vii. The comparison of inverted volumes from simultaneous and elastic impedance inversion techniques revealed good correlation at 1850 ms and 2050 ms which represent sands K01 and

N01,though the prospects are more visible at the Far-far elastic impedance volume beacause the far-angles are more sensitive to changing saturations than near-angles.

viii. The low Poisson's ratio from the fluid prediction map indicated presence of hydrocarbon while lithology map reflected high Vsand of good quality.

ix. The study showed that rock-property models from simultaneous and elastic impedance inversions are effective predictive tools for lithology and fluid types which in turn can guide well placement and reservoir development in the field of study.

5.3 CONTRIBUTIONS TO KNOWLEDGE

i. The study has generated elastic volumes and regression equations useful for the prediction of reservoir properties away from the well control. Also, this could be adopted in other fields with limited well data with similar geological setting.

ii. $\lambda\rho$ has been identified in this study to be a better lithology and fluid discriminator when compared with other seismic attributes because it contains bulk density which has assisted in defining the lithology and fluid types properly.

iii. By converting boundary interface information to layer property, this study obtained high precision reservoir properties to enhance viable hydrocarbon exploration in the study area.

5.4 RECOMMENDATIONS

1. The techniques applied in this study have been able to determine the lithology and fluid types in the identified prospect zones but for additional detail to build geological and hydrodynamic model, geostatistical inversion technique is required for better planning of production well.

2.   Further study should be carried out to cover larger seismic data so as to provide robust information for higher degree of certainty and to evaluate new potential areas identified.

REFERENCES

Adekanle, A. and Enikanselu, P. A. (2013). Porosity Prediction from Seismic Inversion Properties over 'XLD' Field, Niger Delta, *America Journal of Science and Industrial Research,* **4**(1), 31-35.

Adeoti, L., Adeleye, K. O., Afinotan, I. and Bello, M. A. (2014). Fluid prediction using AVO analysis and forward modelling of deep reservoirs in Faith Field, Niger Delta, Nigeria, *Arabian Journal of Geosciences*, **8**(6), 4057-4074.

Aki, K. and Richards, P. G. (1980). *Quantitative Seismology*, Freeman, W. H. and Co San Francisco.557.

Aki, K., and Richards, P.G. (2002). *Quantitative Seismology*, Theory and methods, Second ed. University science Books, Sausalito, California.700.

Alfaro, J. C., Corcoran, C., Davies, K, Pinda, F. G., Hampson, G., Hill, D., Howard, M., Kapoor, J. and Kragh, E., (2007). Reducing Exploration Risk, *Spring*, 26-47.

Allen, J.L. and Peddy, C.P. (1993). *Amplitude variation with offset Gulf Coast Case studies*. Society of exploration Geophysicists, Tulsa, 120.

Avseth, P., Murkerji, T. and Mavko, G. (2005). *Quantitative Seismic Interpretation*. Cambridge University press, Cambridge. UK.

Avbovbo, A. A. (1978). Tertiary lithostratigraphy of Niger Delta, *American Association of Petroleum Geologists Bulletin*, 62, 295-300.

Backus, M. M. (1987). Amplitude versus offset, Proceedings of the *57th SEG Annual International Meeting* held in New Orleans, Louisiana, United states, October 11-15, 617-620.

Bacon, M., Simm, R. and Redshaw, T. (2003). 3-D Seismic Interpretation, Cambridge University Press, Cambridge, UK.

Beka, F. T. and Oti, M. N. (1995). The distal offshore Niger Delta. In: *Frontier prospects of a mature petroleum province* (Eds. Oti, M.N. and Postma, G.). 237-241.

Berge, T. B., Aminzadeh, F., de Groot, P. and Oldenziel, T. (2002). Seismic inversion successfully predicts reservoir, porosity, and gas content in Ibhubesi field, Orange Basin, South Africa, *The Leading Edge*, 21, 338–348.

Biot, M.A., (1956). Theory of propagation of elastic waves in a fluid saturated porous solid; Low frequency range*, Journal of Acoustic Society of America*, 28, 168-178.

Burke, K. (1972). Longshore drift, submarine canyons, and submarine fans in development of Niger Delta, *American Association of Petroleum Geologists*, 56, 1975-1983.

Bustin, R. M. (1988). Sedimentology and characteristics of dispersed organic matter in Tertiary Niger Delta, origin of source rocks in a deltaic environment, *American Association of Petroleum Geologists Bulletin*, 72, 277-298.

Castagna, J. P.and Swan, H.W. (1997). Principles of AVO cross plotting, *The Leading Edge*, **16**(4), 337-342.

Chen, T., Goodway, W. N., Zhang, W., Potocki, D., Uswak, G., Calow, B. and Gray, F. D. (1998). Integrating Geophysics, Geology and Petrophysics: A 3D Seismic AVO and borehole

/logging case study, Proceedings of the 68th *Annual International Meeting of Society of Exploration Geophysicists* held in Washington, March 14-18. 615-618.

Chen, T., Al-Rashed, T., Husain, R.,Singh, P. and Evdokimova, M. (2014). 3D Seismic Prestack Inversion for Predicting Fracability Attributes - A Case Study in North Kuwait, Proceedings of the 76th *International Conference and Exhibition of European Association of Geoscientists and Engineers* held in Amsterdam, Netherlands, June 16-19.

Chopra, S. and Kuhn, O. (2001). Seismic inversion, Canadian Society of Exploration Geophysicists, 26 (1), 10-14.

Chopra, S. and Marfurt, K. J. (2005). Seismic Attributes – A Historical Perspective, *Geophysics,* **70** (5), 3 - 28.

Connolly, A. P. and Hughes, M. J. (2014). The Application of very large number of pseudo-wells for reservoir characterization, Proceedings of the *30th International Conference and Exhibition of European Association of Geoscientists and Engineers* held in Abu Dhabi, United Arab Emirates, November 10-13. 1200-1230.

Connolly, P. (1999). Elastic Impedance, *The Leading Edge*, 18, 438 - 452.

Contreras, A., Torres-Verdin, C. and Fasnacht, T. (2006). AVA simultaneous inversion of partially-stacked seismic amplitude data for spatial delineation of lithology and fluid units deep water hydrocarbon reservoirs in the central Gulf of Mexico. *Geophysics,* **71**(4), 41-48.

Dolberg, D. M., Helgesen, J., Hanssen, T. H., Magnus, I., Saigal, G., and Pedersen, B. K. (2000). Porosity prediction from seismic inversion, Lavrans Field, Halten Terrace, Norway, *The Leading Edge*, **19**(4), 392-399.

Doust, H. and Omatsola, E. (1990). Niger Delta. In: *Divergent and Passive Margin Basins* (Eds. Edwards, P.A. and Santogrossi, P.A.). *American Association of Petroleum Geologists*, Tulsa, USA, 45, 239-248.

Dufour, J., Squires, J., Goodway, W.N., Edmunds, A. and Shook, I. (2002). Integrated geological and geophysical interpretation case study, and Lame rock parameter extractions using AVO analysis on the Blackfoot 3C-3D seismic data, southern Alberta, Canada, *Geophysics,* 67, 27-37.

Ehsan, I. M., Ahmed, N., Khalid, P., Wei, X. L. and Naeem, M. (2016). Application of rock physics modeling to quantify the seismic response of gas hydrate-bearing sediments in Makan accretionary prism, offshore Pakistan, *Geosciences Journal*, **20**(3), 321-330.

Edwards, J.D. and Santogrossi, P.A. (1990). Summary and conclusions, in, Edwards, J.D., and Santogrossi, P.A., eds., Divergent/passive Margin Basins, *American Association of Petroleum Geologists Memoir*, Tulsa, 48, 239-248.

Ejedawe, J.E., Coker, S.J.L., Lambert-Aikhionbare, D.O., Alofe, K.B. and Adoh, F.O. (1984). Evolution of oil-generative window and oil and gas occurrence in Tertiary Niger Delta Basin, *American Association of Petroleum Geologists*, 68, 1744-1751.

Ekweozor, C. M. and Daukoru, E.M. (1984). Petroleum source bed evaluation of Tertiary Niger Delta—reply, *American Association of Petroleum Geologists Bulletin*, 68, 390-394.

Ekweozor, C. M., Okogun, J.I., Ekong, D.E.U. and Maxwell J.R. (1979). Preliminary organic geochemical studies of samples from the Niger Delta, Nigeria: Part 1, analysis of crude oils for triterpanes, Chemical Geology, 27, 11-28.

Ekweozor, C.M. and Okoye, N.V. (1980). Petroleum source-bed evaluation of Tertiary Niger Delta, *American Association of Petroleum Geologists Bulletin*, 64, 1251-1259.

Etu-Efeotor, J.O. (1997). *Fundamentals of Petroleum Geology*, Paragraphics Publisher, Port Harcourt, Nigeria. 146.

Evamy, B.D., Haremboure, J., Kamerling, P., Knaap, W.A., Molloy, F.A. and Rowlands, P.H., (1978). Hydrocarbon habitat of Tertiary Niger Delta, *American Association of Petroleum Geologists Bulletin*, 62, 277- 298.

Feng, H. and Bancroft, J. C. (2006). AVO Principles, processing and inversion *Crewes Research Report*, 18, 1-19.

Filippova, K., Kozhenkov, A. and Alabushin, A. (2011). Seismic inversion techniques: choice and benefits, *First break,* 29, 103-114.

Frost, B., R. (1997). A Cretaceous Niger Delta Petroleum System, In: Extended Abstracts, AAPG/ABGP Hedberg Research Symposium, *Petroleum Systems of the South Atlantic Margin,* Rio de Janeiro, Brazil. 1 - 8.

Gassman, F. (1951). Elastic waves through a packing of spheres, *Geophysics*, 16, 85-673.

Goodway, B., Chen, T., and Downton, J. (1997). Improved AVO Fluid detection and lithology discrimination using Lame's Petrophysical parameters; "$\lambda\rho$, $\mu\rho$, $\lambda\mu$ Fluid stack" from

P and S inversions, Proceedings of the *67th Annual International Meeting of Society of Exploration Geophysicists* held in Dallas, Texas, November 2-7. 4.

Gray, F. D. and Andersen, E. A. (2000). The application of AVO and Inversion to Formation Properties, *World oil*, 221(7), 9-11.

Gregory, A.R. (1977). Aspects of rock physics from laboratory and log data that are important to seismic interpretation, *AAPG memoir,* 26, 15-46.

Haack, R.C., Sundararaman, P. and Dahl, J. (1997), Niger Delta petroleum System, Presented at *AAPG/ABGP Hedberg Research Symposium, Petroleum Systems of the South Atlantic Margin* held at Rio de Janeiro, Brazil, November 16-19.

Hampson, D. P., Russell, B. H and Bankhead, B. (2006). Simultaneous inversion of pre-stack seismic data, *Geohorizons*, 13-17.

Hospers, J. (1965). Gravity field and structures of the Niger delta, Nigeria, West Africa, *Geolological Society of America Bulletin*, 76, 407-422.

Hunt, J. M. (1990). Generation and Migration of Petroleum from Abnormally Pressured Fluid Compartments, *American Association of Petroleum Geologists Bulletin*, **7**(4), 1-12.

Jason Geoscience Workbench (2013). Simultaneous AVA/AVO Inversion. Fugro-Jason, Netherlands.

Kaplan, A., Lusser, C.V. and Norton, I.O. (1994). Tectonic Map of the World. Panel 10 Tulsa, *AAPG Bulletin,* 74, 1-12.

Khalid, P., Ahmed, N., Mahmood, A. and Saleem M. A. (2015). An Integrated Seismic Interpretation and Rock physics attribute analysis for pore fluid discrimination in Rotana area of Northern Potwar in Pakistan, *Arabian Journal for Science and Engineering*, **4**(1), 191-200.

Kong, V. W., Kyaw, M. U., Koko, U., Paxton, A. and Hobbs, C. M. (2013). Differentiating between potential reservoirs and hard rock with a holistic quantitative seismic interpretation method, Proceedings of the *23rd International Conference and Exhibition of Geophysical* held in Melbourne, Australia, August 11-14. 7.

Kulke, H. (1995). Nigeria. In: *Regional Petroleum Geology of the World Part II.* (Eds. Kulke, H.). Africa, America, Australia and Antarctica Berlin, Gebrüder Borntraeger, 143-172.

Lambert-Aikhionbare, D. O. and Ibe, A.C. (1984). Petroleum source-bed evaluation of the Tertiary Niger Delta, *American Association of Petroleum Geologists Bulletin*, 68, 387-394.

Lavergne, M., Willm, C. (1977). Inversion of seismograms and pseudo-velocity logs, Geophysical Prospecting, 25, 232-250.

Lefeuvre, F.E., Wrolstad, K.H., Zou, K.S., Smith, L.J., Maret, J.P., Nyein, U.K. (1995). Sand-shale ratio and sandy reservoir properties estimation from seismic attributes: an integrated study, *Society of Exploration Geophysicists,* 95, 108-110.

Lehner, P. and De Ruiter, P.A.C. (1977). Structural history of Atlantic Margin of Africa. *American Association of Petroleum Geologists Bulletin*, 61, 961-981.

Lindseth, R.O. (1979). Synthetic sonic logs: a process for stratigraphic interpretation, Geophysics, 44, 3-26.

Lortzer, G.J. and Berkhout, A.J. (1992). An integrated approach to lithologic inversion, *Geophysics*, 57, 233-244.

Michel, K. (2010). Rock physics driven inversion; the importance of work flow, *First break,* 28, 69-8.

Miguel, B., Gabriel, A., Diego, M., Vicmar, A., Yohaney, G. and Thais, D. (2012). Seismic inversion and statistical classification of lithology and fluids at Rubiales field, Colombia, Proceedings of the 82nd SEG Annual International Conference held in Las Vegas, Nevada, USA, November 4-9, 8.

Montazeri, M. (2013**).** Reprocessing of 2D Reflection Seismic Marine Data and Investigation into the AVO behaviour of Cambrian Sandstones, Southern Baltic Sea, Sweden. *Geofysik*, 45, 31-42.

Neves, F.A., Mustafa, H.M. and Rutty, P.M. (2004). Pseudo-gamma ray volume from extended elastic impedance inversion for gas exploration, *The Leading Edge,* 23, 536-540.

Nguyen, N. and Larry, F. (2008). From Angle Stacks to Fluid and Lithology Enhanced stacks, *Hyderabad*, 41, 1-5.

Nwachukwu, S.O. (1972). The tectonic evolution of the southern portion of the Benue Trough, Nigeria, *Geology Magazine*, 109, 411-419.

Nwachukwu, J. I. and Chukwurah, P. I. (1986). Organic matter of Agbada Formation, Niger Delta, Nigeria, *American Association of Petroleum Geologists Bulletin*, 70, 48-55.

Omar, V. J., Torres-Verdin, C. and Lake, L. (2006). On the value of 3D amplitude data to reduce uncertainty in the forecast of reservoir production, *Journal of Petroleum Science and Engineering*, 20, 269-284.

Omudu, L. M., Ebeniro, J. O., Xynogalas, M., Adesanya, O. and Osanyande, N. (2007). Beyond Acoustic Impedance, An onshore Niger Delta Experience, Proceedings of the *Annual International Meeting of the Society of Exploration Geophysicists* held in San Antonio, Texas, September 23-26. 4.

Pendrel, J., Debeye, H., Pedersen-Tatalovic, R., Goodway, B., Dafour, J., Bogaards, M., and Stewart, R. (2000). Estimation and Interpretation of P and S Impedance Volumes from Simultaneous Inversion of P-wave Offset Seismic Data, Proceedings of the *70th Annual International Meeting of Society of Exploration Geophysicists* held in Calgary, Alberta, August 8-11, 146-149.

Phillips, D. (2008, May 10). Cost of Offshore Drilling Rising as Fast as oil Prices, Columbia Broadcasting System News (CBSN), Los Angeles.

Rajagopal, R., Khaled, O., Zuabi, Y. and Chen, T. (2015). Prediction of shear velocity using Rock Physics Modelling for Seismic Reservoir Characterization, presented at the 3rd *European Association of Geoscientists and Engineers Workshop* held in Istanbul, Turkey, November 15-18.

Rasmussen, K. B., Bruun, A. and Pedersen, J.M. (2004). Simultaneous seismic inversion, Proceedings of the 66th *International Conference and Exhibition of European Association of Geoscientists and Engineers* held in Paris, June 7-20.

Reijers, T.J.A., Petters, S.W. and Nwajide, C.S. (1997). The Niger Delta Basin. In: *African Basins-*
-Sedimentary Basin of the World III (Eds. Selley, R.C.). Elsevier Science,
Amsterdam, 151-172.

Rijks, E.J. and Jauffred, J.C. (1991). Attribute extraction: An important application in any detailed
3-D interpretation study, The Leading Edge, 10, 11-19.

Rutherford, S. R. and Williams, R. H. (1989). Amplitude versus offset variation in gas sands,
Geophysics, 54, 680-688.

Sancevero, S.S., Remacre, A.Z., Portugal, R.S., Mundim, E.C. (2005). Comparing deterministic
and tochastic seismic inversion for thin-bed reservoir characterization in a turbidite
synthetic reference model of Campos Basin, Brazil, Leading Edge, **24**(11), 1094-
1179.

Shannon, P. M. and Naylor, N. (1989). *Petroleum Basin Studies*. Graham and Trotman Limited,
London, 153-169.

Shaoming, L. and George, A. M. (2004). Elastic impedance inversion of multichannel seismic data
from unconsolidated sediments containing gas hydrate and free gas, *Geophysics,*
69(1), 164-179.

Sheriff, R. (1992**).** Limitation on resolution of seismic reflections and geologic detail derivable
from them. In*: Seismic stratigraphy – applications to hydrocarbon exploration*
(Eds. Payton, C.E). America Association of Petroleum Geologists, Tulsa, USA, 26,
3-14.

Short, K. C. and Stauble, A. (1967). Outline Geology of Niger Delta, *America Association of Petroleum Geologists,* 51, 761-776.

Shuey, R.T. (1985). A simplification of the Zoeppritz equations, *Geophysics*, **50** (4), 609-614.

Singh, S., Gupta, D.K and Rajput, S. (2014). Pre-Stack Seismic Inversion and Amplitude Versus Angle Modeling Reduces the Risk in Hydrocarbon Prospect Evaluation, *Advances in Petroleum Exploration and Development*, **7**(2), 30-39.

Smith, G.C. and Gidlow, P.M. (1987). Weighted stacking for rock property estimation and detection of gas, *Geophysical Prospecting*, **35**(9), 993-1014.

Smith, T.M., Sondergeld, C. H. and Rai, C. S. (2003). Gassmann fluid substitutions, *Geophysics*, 68, 430-440.

Stacher, P. (1995). Present understanding of the Niger Delta hydrocarbon habitat. In: *Geology of Deltas* (Eds. Oti, M.N. and Postma, G.). Rotterdam, Balkema, 257-267.

Suslick, S. B, Schiozer, D. and Rodriguez, M. R. (2009). Uncertainty and Risk Analysis in Petroleum Exploration Production, *Terrae*, **6**(1), 30-41.

Tuttle, M. L.W., Charpentier R. R. and Brownfield, M. E. (1999). The Niger Delta Petroleum System: Niger Delta Province, Nigeria, Cameroon, and Equatorial Guinea, Africa, *United States Geological Survey*, Open-File Report 99-50-H.

Veeken, P.C. and Da Silva, M. (2004), Seismic Inversion and some of their constraints, *First Break,* **22**(6), 47-70.

Weber, K. J. and Daukoru, E.M. (1975). Petroleum geology of the Niger Delta, Proceedings of the *9th World Petroleum Congress Geology* held in London, 2, 210-221.

Whiteman, A. (1982). *Nigeria: Its Petroleum Geology, Resources and Potential*. Graham and Trotman Limited, London, 394.

Whitcombe, D. N., Connolly, P. A., Reagan, R. L. and Redshaw, T. C. (2002). Extended elastic impedance for fluid and lithology prediction, *Geophysics*, 67, 63-67.

Xiao, H. and Suppe, J. (1992). Origin of rollover, *American Association of Petroleum Geologists Bulletin,*76, 509-229.

Yilmaz, O. (2002). *Seismic Data Analysis: Processing, Inversion, And Interpretation of Seismic Data.* Society of Exploration Geophysicists, Tulsa, 2027.

Young, R.G., Mrinal, K. and Sen, M.K. (2007). A comparison of porosity estimates obtained using post, partial and prestack seismic inversion methods: 'Marco Polio' Field, Gulf of Mexico, Proceedings of the *77th Annual International Meeting of Society of Exploration Geophysicists held* in San Antonio, September 23-26,1790-1794.

APPENDIX A
SEISMIC TO WELL TIE
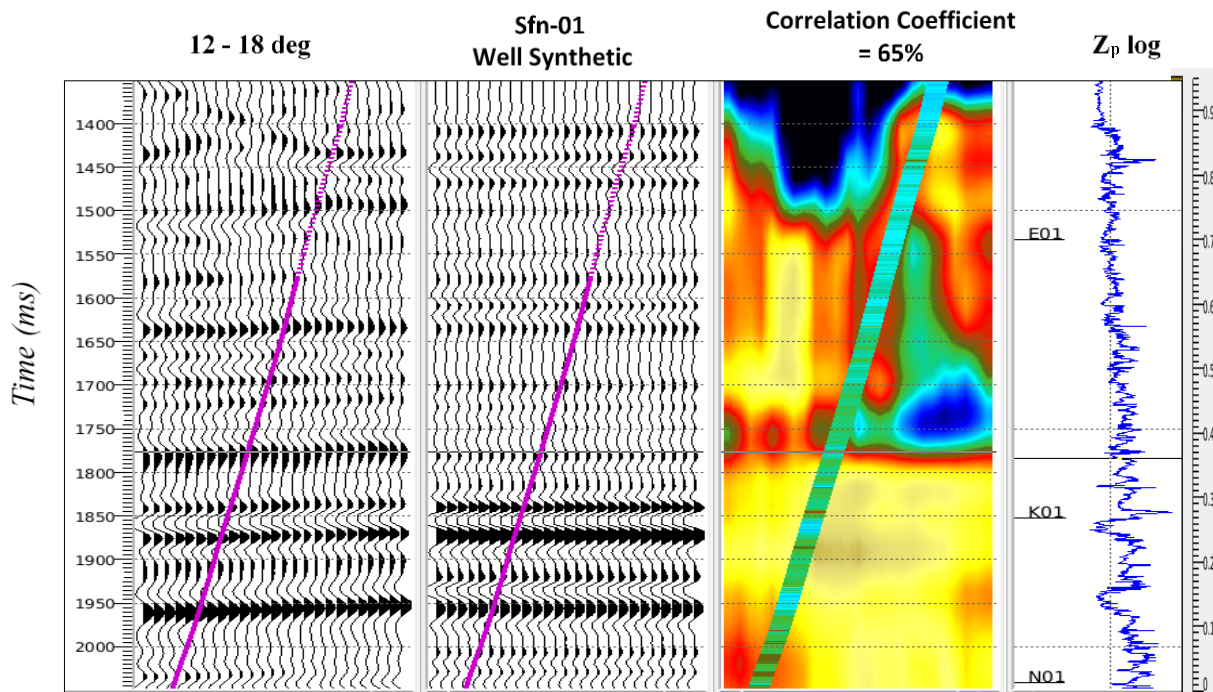
Figure 22d: Seismic to well tie using the near mid (12°-18°) stack and Sfn-01.
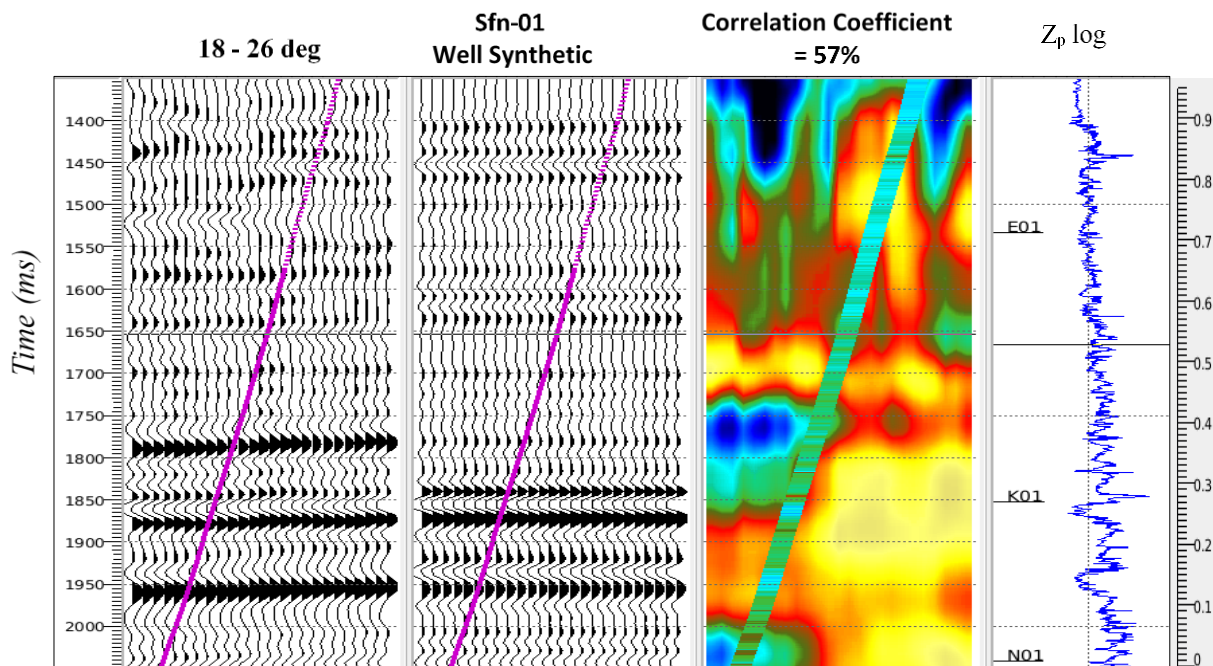
Figure 22e: Seismic to well tie using the mid (18°-26°) stack and Sfn-01.
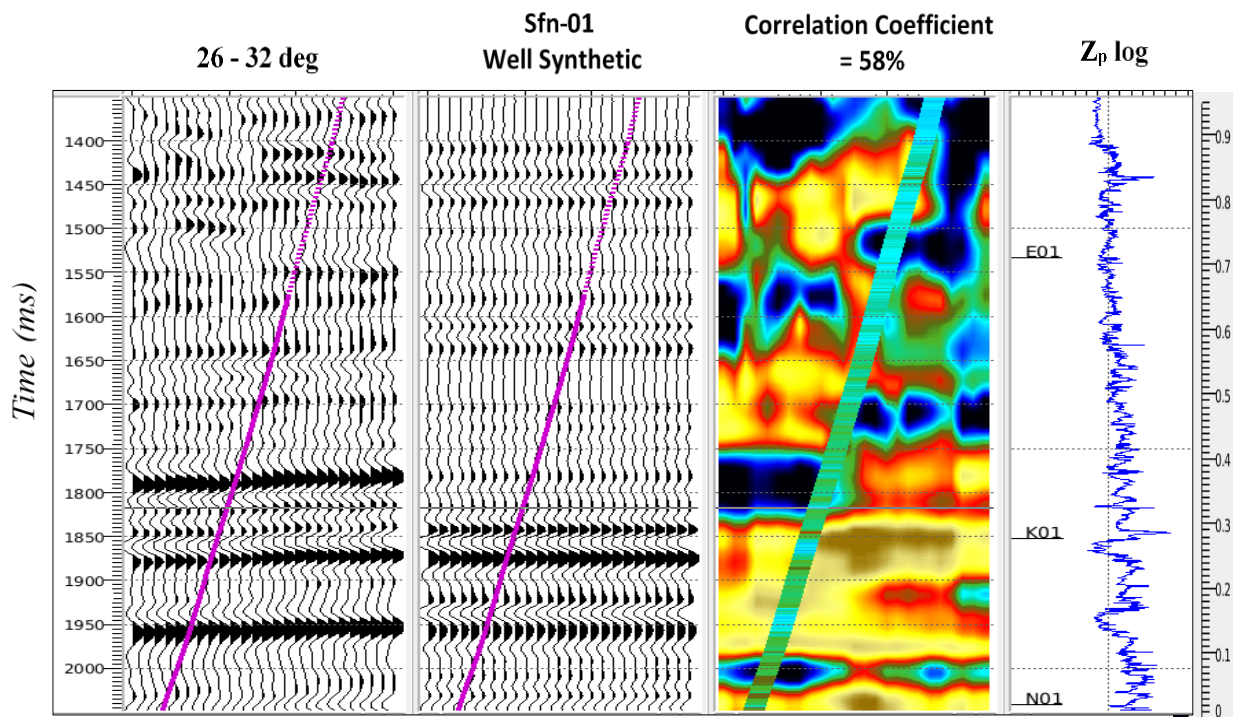
Figure 22f: Seismic to well tie using the far (26°-32°) stack and Sfn-01.
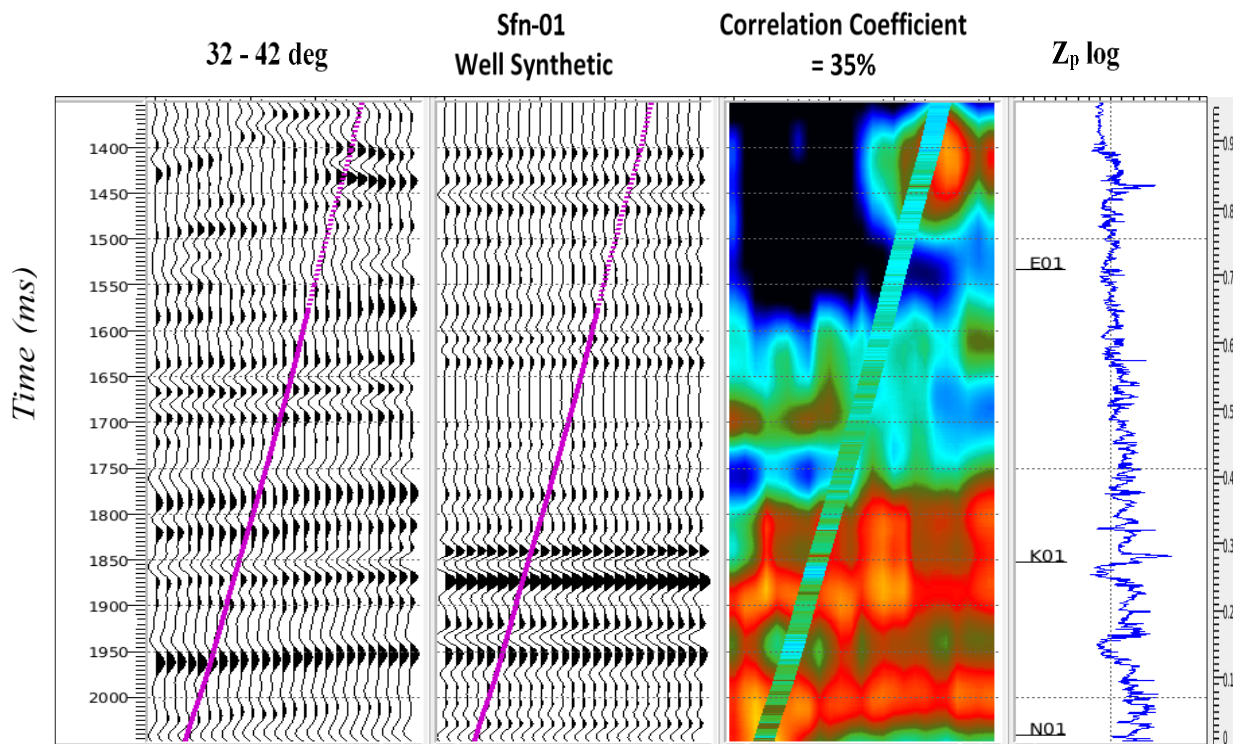
Figure 22g: Seismic to well tie using the far-far (32°-42°) stack and Sfn-01.
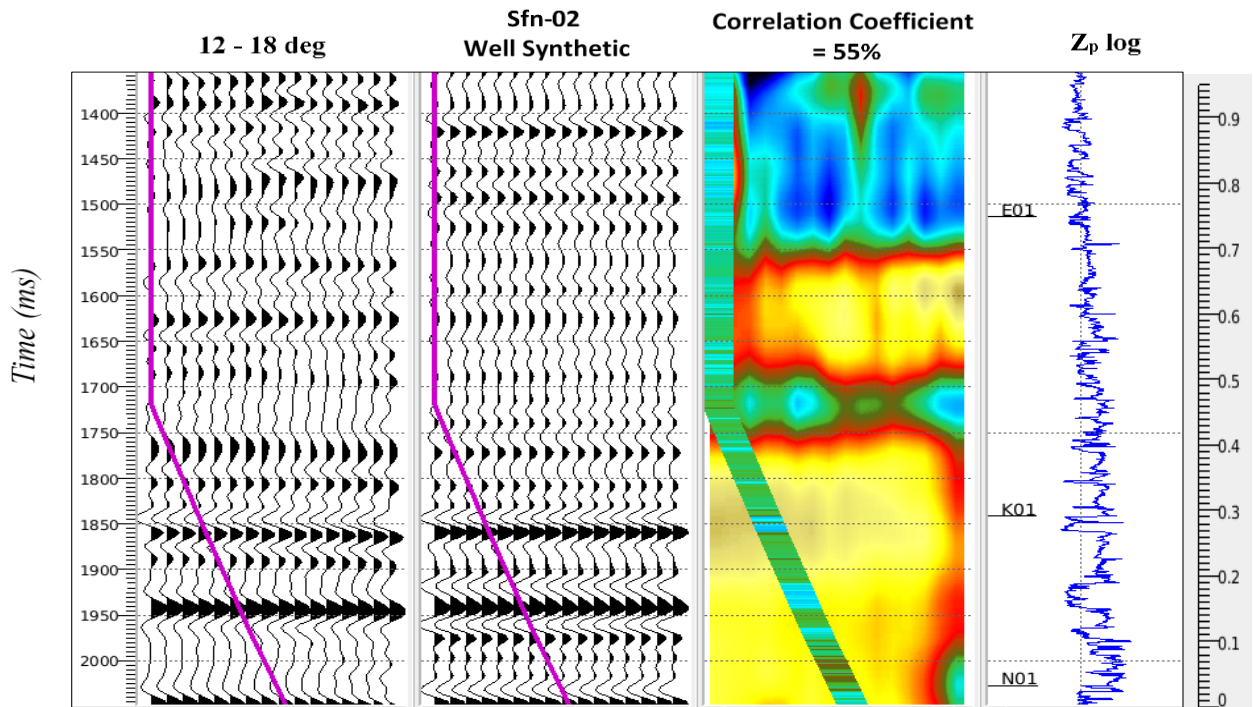
Figure 22h: Seismic to well tie using the near mid (12°-18°) stack and Sfn-02.
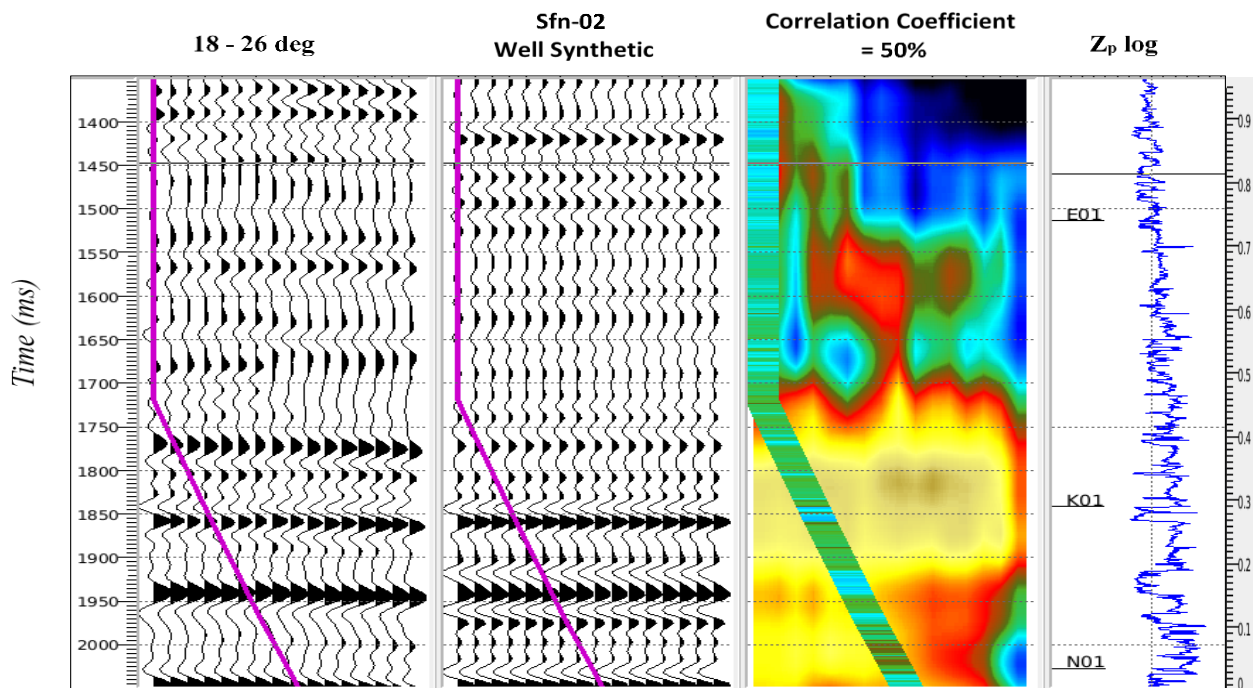
Figure 22i: Seismic to well tie using the mid (18°-26°) stack and Sfn-02.

117
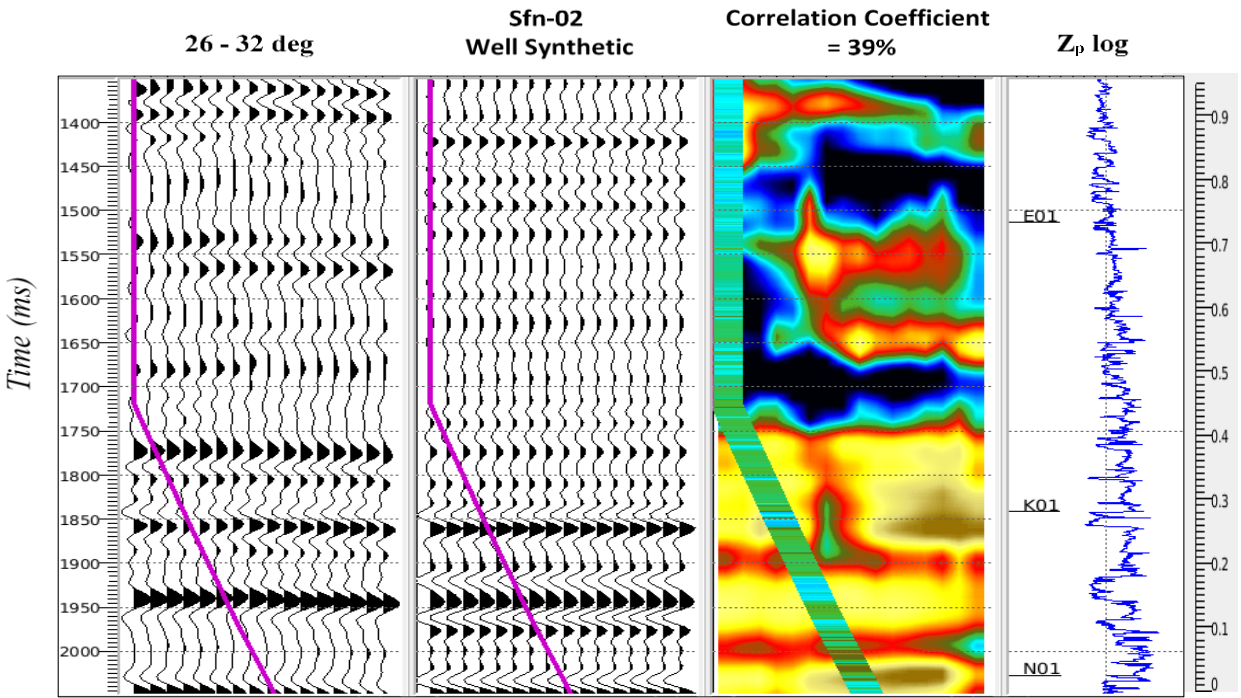
Figure 22j: Seismic to well tie using the far (26°-32°) stack and Sfn-02.
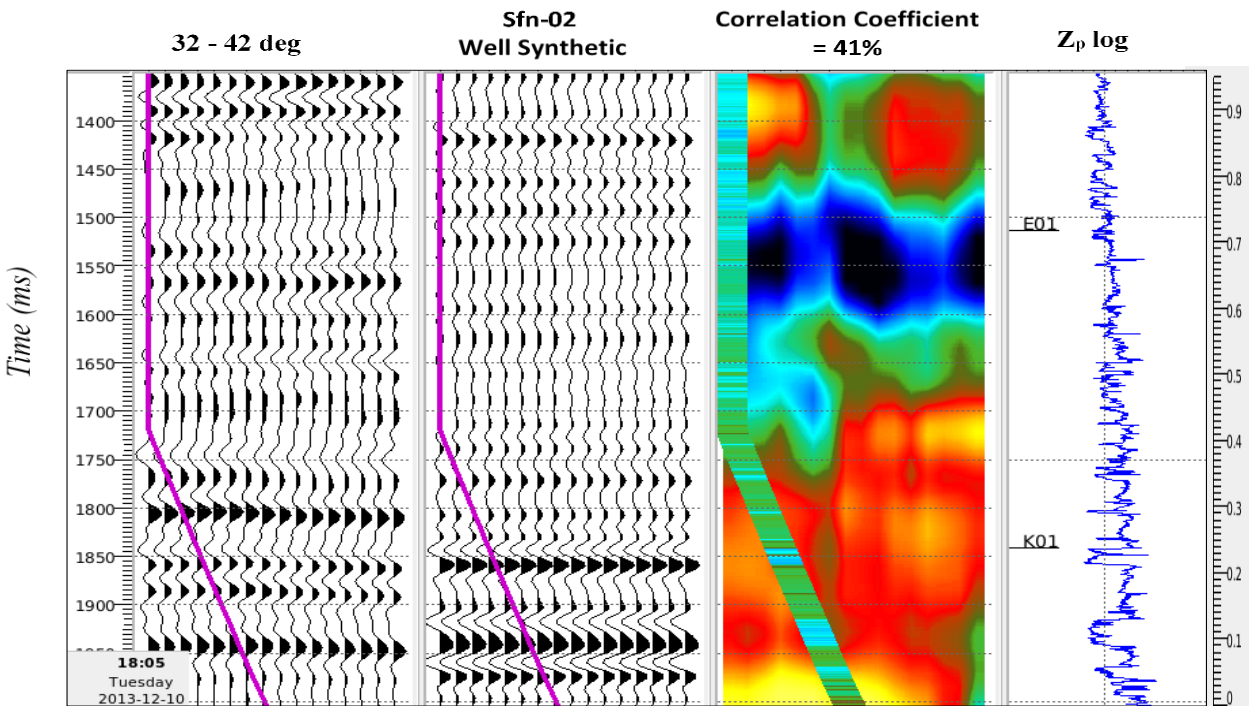
Figure 22k: Seismic to well tie using the far-far (32°-42°) stack and Sfn-02.
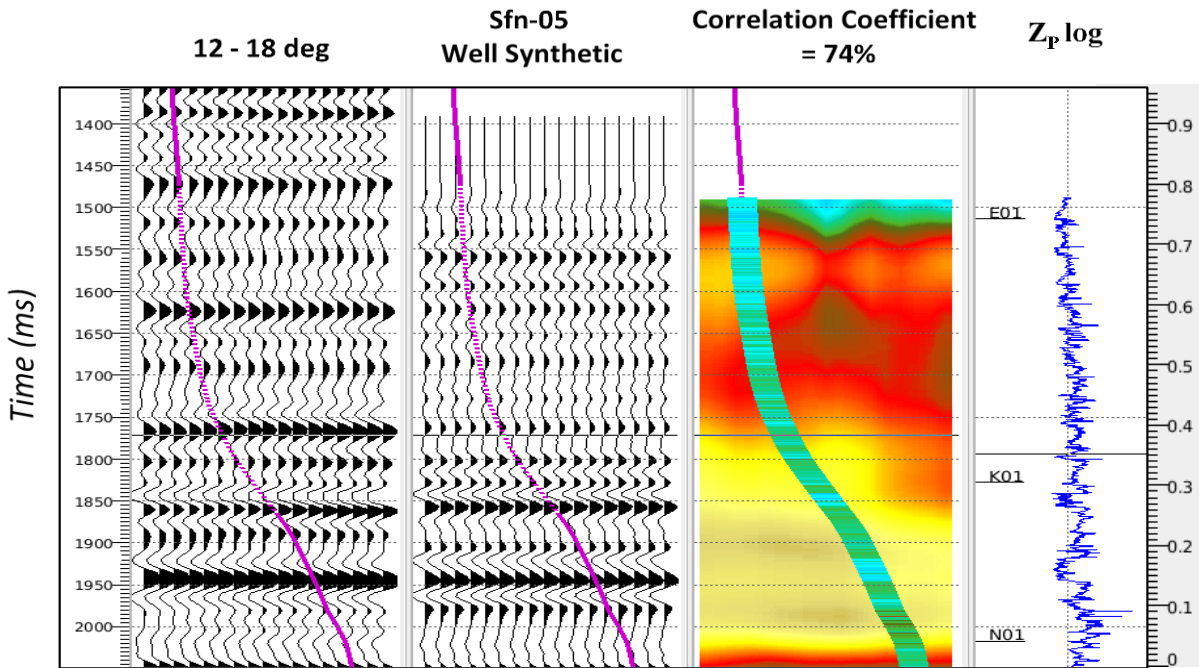
Figure 22l: Seismic to well tie using the near mid (12°-18°) stack and Sfn-05.
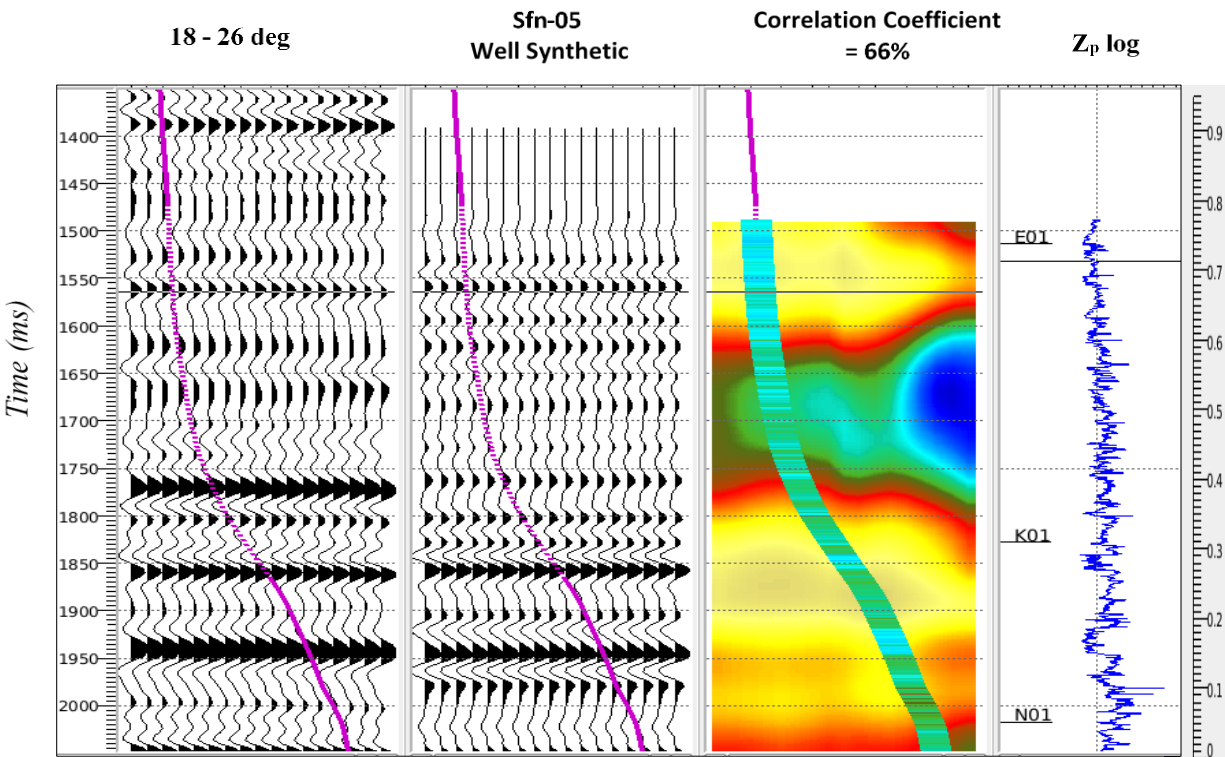
Figure 22m: Seismic to well tie using the mid (18°-26°) stack and Sfn-05.
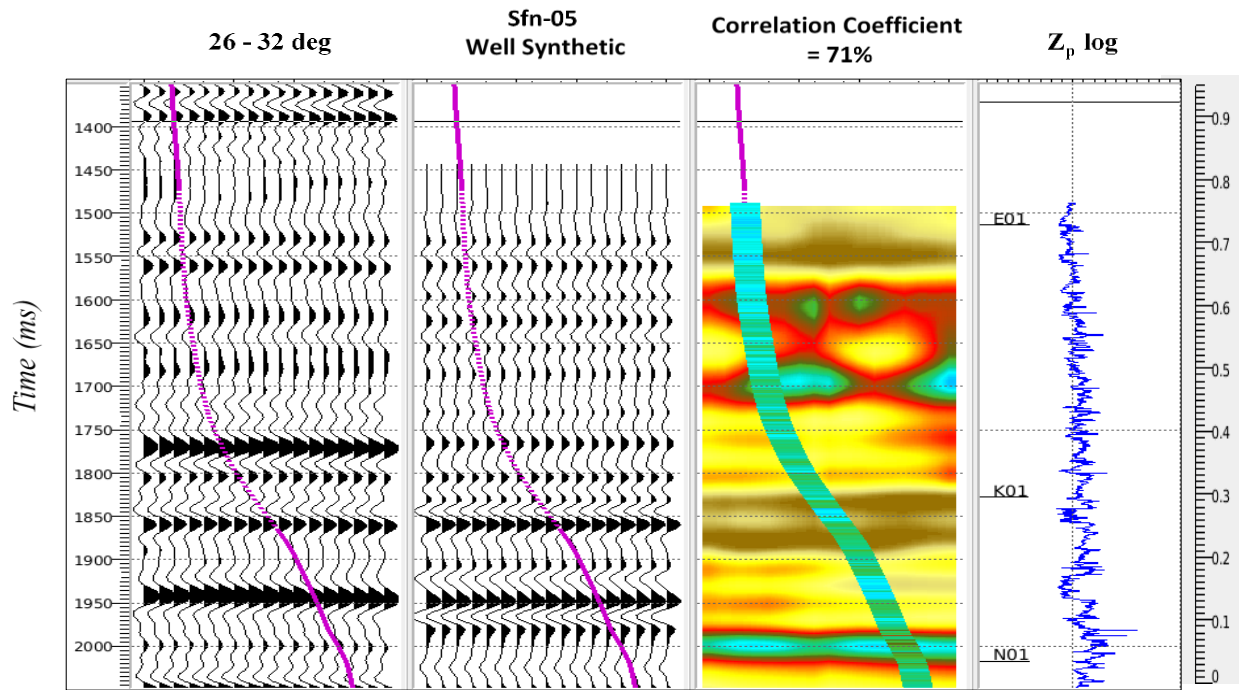
Figure 22n: Seismic to well tie using the far (26°-32°) stack and Sfn-05.
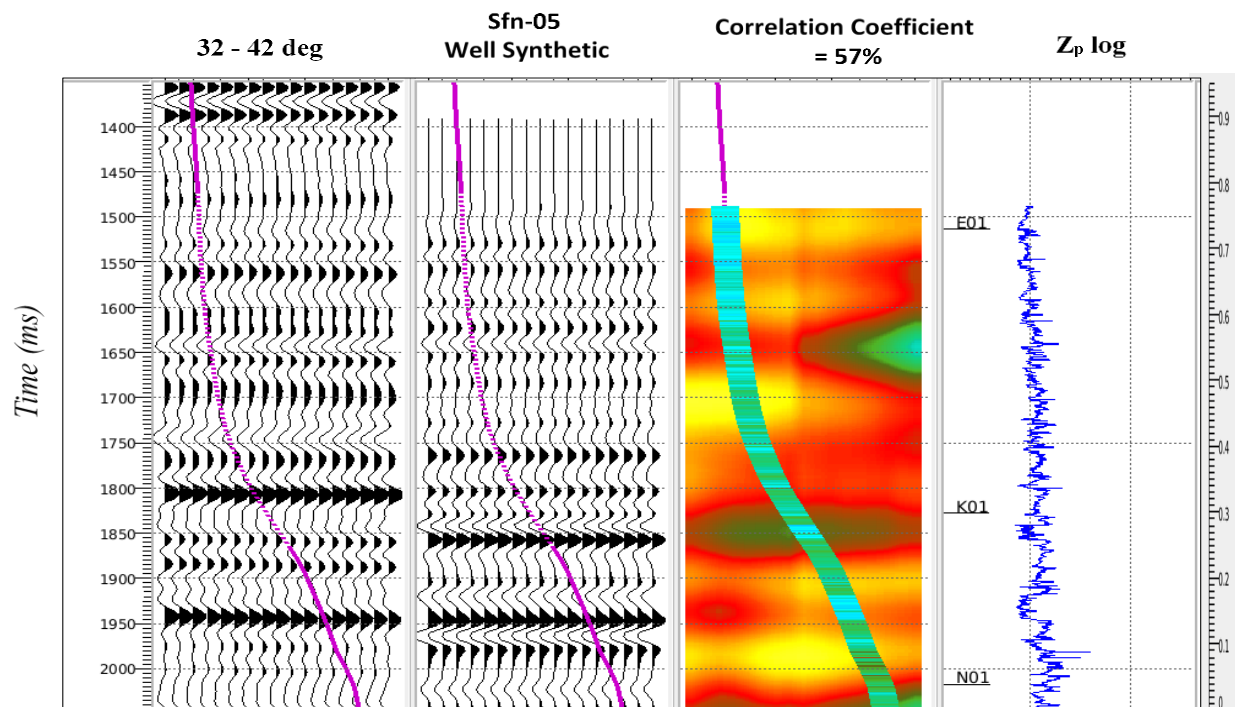
Figure 22o: Seismic to well tie using the far-far (32°-42°) stack and Sfn-05.